Photoionisation of ^{40}Ca with a frequency-doubled 422 nm laser and a 377 nm laser diode

A diploma thesis submitted to the

Faculty for Mathematics, Computer Science and Physics
University of Innsbruck

In partial fulfilment of the requirements for the degree of
Master of Natural Science
Magister Rerum Naturalium

by
Regina Lechner

Supervisor: Prof. Dr. Rainer Blatt
Department of Experimental Physics

May 2010

Mousa: And this, what is this one?
Rambo: It's a blue light.
Mousa: What does it do?
Rambo: It turns blue.

Rambo III

Abstract

This thesis reports on the setup of a photoionisation system for ^{40}Ca consisting of a frequency-doubled system to generate 422 nm light and a laser diode to provide 377 nm light. Of special interest is the frequency doubling system to generate the second - harmonic power at 422 nm wavelength, as the commercial shortage of diodes at this wavelength necessitated alternative solutions. The full functionality of the setup was tested by the measurement of atomic fluorescence and the trapping of ions in a surface-electrode ion trap at room temperature.
The description presented here summarises both the theoretical considerations and experimental work in order to build a setup to photoionise ^{40}Ca, consisting of a frequency-doubled light source generating a second-harmonic wave at 422 nm and a 377 nm laser diode.

Contents

1. Introduction and Motivation **1**

2. Photoionisation of Calcium **3**
2.1. Calcium . . . 3
2.1.1. Calcium I . . . 4
2.1.2. Calcium II . . . 4
2.2. Atom-light interaction . . . 5
2.2.1. Two-level system . . . 5
2.2.2. Rate equations and bound-free transition . . . 7

3. Frequency Doubling **11**
3.1. Nonlinear optics . . . 11
3.1.1. Nonlinear wave equation . . . 12
3.1.2. Birefringent phasematching and quasi-phasematching . . . 14
3.2. SHG using lasers as coherent light source . . . 18
3.2.1. Summary . . . 20

4. Output Enhancement with an Optical Cavity **21**
4.1. Creating a stable resonator - The ABCD matrices . . . 22
4.1.1. ABCD matrix and Gaussian beams . . . 22
4.1.2. ABCD matrices for a bow-tie cavity with a nonlinear crystal . . . 24
4.2. Enhancement of the SHG power using a bow-tie resonator . . . 25
4.2.1. Parameters for resonant frequency doubling using a bow-tie cavity . . . 26
4.2.2. Resonator enhancement of the second harmonic . . . 30

5. Photoionisation Setup **35**
5.1. Characterisation of the lasers . . . 35
5.1.1. 844 nm laser . . . 35
5.1.2. 422 nm laser . . . 38
5.1.3. 377 nm laser . . . 40
5.2. Cavity . . . 42
5.3. Hänsch - Couillaud stabilisation . . . 43
5.4. Temperature stabilisation of the crystal . . . 46
5.5. Fibre coupling and overlap with 377 nm laser . . . 50
5.6. Summary . . . 50

6. Experimental Implementation **53**
6.1. Surface-electrode trap . . . 53
6.2. Vacuum chamber . . . 56
6.3. Imaging . . . 56
6.4. Experimental results . . . 57
6.4.1. Atomic fluorescence . . . 57
6.4.2. Loading . . . 59

6.5. Summary 60

7. Conclusion and Outlook **63**

Appendices

A. A Survey of Frequency Doubling **65**
A.1. Deriving the nonlinear wave equation 65
A.2. The Boyd-Kleinman approach 66

B. Resonant SHG **69**
B.1. Finesse 69
B.2. SHG with a resonator 70

C. Laser Setup **73**
C.1. Calibration of TOPTICA's DTC 110 SVL 73
C.2. Using the 422 nm frequency doubler 73
C.3. Considerations for building a doubler 76

Bibliography **79**

List of Figures

2.1. Photoionisation transition in calcium 4
2.2. Energy level structure of $^{40}Ca^{+}$ used in experiments 5
2.3. Schematic of a two-level atom 6
2.4. Population probability as a function of Rabi frequency and time 7

3.1. Indicatrix for angle - and temperature tuning 15
3.2. Index ellipsoid to explain the walk-off 16
3.3. Intensity growth of the second-harmonic wave for different phasematching cases 17
3.4. Boyd - Kleinman factor for various conditions 20

4.1. Schematic of the bow-tie resonator geometry 21
4.2. Figure on the waist in the short arm of the bow-tie resonator 25
4.3. Bow-tie resonator schematic with fields denoted 26
4.4. Power ratio at resonance as a function of input mirror reflectivity, R_1 27
4.5. Circulating power excluding and including conversion losses 29
4.6. Airy function for the transmission at multiple beam interference 30
4.7. Second-harmonic power as a function of input coupling mirror reflectivity, R_1 . 31
4.8. Overall conversion efficiency as a function of incident fundamental power 32
4.9. Second-harmonic light power for single pass and with cavity enhancement . . . 33

5.1. Schematic showing the complete photoionisation laser setup 36
5.2. Optical power as a function of supply current for the 844 nm laser 37
5.3. Schematic showing the complete 844nm laser beam path 38
5.4. Optical power at 422 nm as a function of pump power at 844 nm 39
5.5. Schematic showing the complete 422 nm beam path 40
5.6. Optical power as a function of supply current for the 377 nm laser 41
5.7. Schematic on the complete 377 nm laser beam path 42
5.8. Schematic on the cavity setup including construction parameters 43
5.9. Basic setup for the Hänsch - Couillaud locking scheme 44
5.10. Calculated Hänsch - Couillaud error signal 45
5.11. Setup of the Hänsch - Couillaud lock 45
5.12. Oscilloscope frame showing the Hänsch Couillaud error signal 46
5.13. Drawing of the crystal mount 47
5.14. Temperature dependence of SHG 49
5.15. Schematic of the setup for overlapping the 422 nm and the 377 nm laser light . 51

6.1. Linear trap configuration 54
6.2. Surface-electrode trap geometry 55
6.3. Three dimensional schematic of the vacuum setup 57
6.4. Schematic of the setup before the trap 58
6.5. Atomic fluorescence measured 59
6.6. Decrease of fluorescence without heated oven 59
6.7. Schematic of the beam path through the chamber 60

6.8. First trapped ions in room-temperature setup 60

A.1. Propagation of a Gaussian beam 66

C.1. Calibration of the temperature measurement 74

List of Tables

2.1. Isotopes of calcium with natural abundance and isotope shifts 3

4.1. Summary of important ABCD matrices 23
4.2. ABCD matrices for a bow-tie resonator with crystal 24

5.1. Specifications of the 844 nm laser diode 36
5.2. Crystal properties for ppKTP 39
5.3. Specifications of the 377 nm laser diode 40
5.4. Mirrors contained in the cavity 42
5.5. Comparison of temperature setup components 47

1. Introduction and Motivation

"The power of quantum computing derives from its scaling properties: as the size of the problems grows the resources required to solve them grow in a manageable way."
Kielspinski 2002

Since the beginning of the 1980s, quantum computers have been discussed as offering an advancement compared to classical Turing machines [1]. The first to recognize and state the tremendous prospects originating from quantum mechanics were Feynman [1] and Deutsch [2]. However, it took until the mid 1990s until the presentation of algorithms [3–7] based on quantum mechanics caused the idea of a quantum computer to be anything more than a curiosity. The formulation of the DiVincenzo criteria [8] summarised five principal conditions to experimentally implement the hitherto theoretical considerations in a physical system. They also provide two principles to allow quantum communication between such devices. A proposal by Cirac and Zoller published in 1995 [5] presented a concrete example of a way in which a realistic system, using already developed physical methods, could be used to implement a quantum computer.

Quantum computing is based on registers consisting of so-called 'qubits'. A qubit is a two-level system analogous to a bit in a classical computational register. However instead of representing either 0 or 1, the states $|0\rangle$ and $|1\rangle$ of the qubit can also appear in superpositions $(\alpha\,|0\rangle + \beta\,|1\rangle)$. α and β are complex numbers that are normalised to $|\alpha|^2 + |\beta|^2 = 1$. Hence, unlike a classical bit, a qubit can represent an abundance of settings corresponding to certain information. A clear picture can be derived, by imagining the classical information as a switch, being either in position on (1) or off (0) whereas the qubit is represented by an arrow, pointing to a certain position on a sphere [9].
The implementation for qubits chosen in the Innsbruck group is based on internal electronic states of $^{40}Ca^{+}$ ions [10], where the qubit is encoded in the ground state $S_{1/2}$ and the metastable $D_{5/2}$ state ($\tau \approx 1.16\,s$ [11]). The element is chosen as it provides closed cycles for Doppler cooling in which any population in undesired long-lived levels can be repumped to the fast cooling transition. State detection is performed by measuring the fluorescence signal of the ion: in case the ground state $S_{1/2}$ is populated, the ion is transferred to the excited state $P_{1/2}$ due to an excitation with a laser. This transfer ($S_{1/2}$ to $P_{1/2}$) represents a strong dipole transition which produces a clearly detectable photon signal (in the range of 10^8 photons) within a timescale that is shorter than the lifetime of the metastable $D_{5/2}$ state. However, if the ion occupies the so-called shelf state, $D_{5/2}$, the fluorescence is suppressed. Hence, a signal arising from this measurement, which is called the electron shelving method [12–14], shows a clear pattern with a signal equal to zero if the ion is in the shelf state and a maximum signal value if the ion is in the ground state. Due to this, the convention is to denote the ground state of the ion state $|1\rangle$ while the excited state is denoted as $|0\rangle$.
All wavelengths necessary to implement the above-mentioned processes (Doppler cooling, repumping, state detection) can be generated using convenient laser sources, based on diodes. Furthermore, the production of $^{40}Ca^{+}$ ions from the neutral element can be carried out using a two step resonant photoionisation process which represents an advantageous loading method. To perform operations on the ions, trapping in a linear Paul trap is accomplished [15, 16] to

localise the ion position and store them for hours at a time. Interactions with a laser beam are used to imprint information on a single ionic qubit and to initialise a certain state. While the electronic qubits act as storage facility for quantum information, the shared collective motional mode of the whole ion string is used as a phonon quantum bus, to distribute the information in the register.
These considerations have been the working principle in a large number of quantum computation experiments during the last 15 years and have produced prominent results [17–33]. However, the number of qubits that can be efficiently manipulated within a linear ion trap is limited to at most a few tens of qubits [34]. This stands in contrast to the proposed implementation of large scale quantum computers which demand thousands or millions of qubits (e.g. [35]). One possibility to circumvent the restrictions created by linear RF ion traps is the use of 'segmented trap arrays' as suggested by Kielpinski [36].
An approach to simplify the fabrication of such segmented trap arrays is to bring all electrodes into a plane, as proposed by Chiaverini et al. [37]. The geometry introduced allows scalability and miniaturisation which is one step to implement a segmented trap array. Such planar trap geometries have been investigated in order to determine their properties and adaptability for large-scale quantum processors [38–40]. However, a common issue is the increased heating rate when scaling-down the trap size [38, 41] attributed predominantly to surface electrode patch potentials [42]. In the most extreme case, the increased heating rates lead to the issue, that the ion gets heated out of the trap within a time range that is too short to implement quantum logic gate operations [43]. Studies of this phenomenon led to the use of cryostats to cool the trap down to cryogenic temperatures [44, 45]. A reduction of the heating rate of seven orders of magnitude was reported by Labaziewicz et al. [45]. In addition to low heating rates, good position control of the ions is needed in order to address individual ions. This can be frustrated by atoms deposited on the electrodes from the oven, and by excess charges building up [46, 47]. To prevent these difficulties, a clean and efficient loading method is needed, reducing contamination of the electrodes and the generation of stray charges as much as possible. One method meeting these conditions which has already been tested in our group [48, 49] is photoionisation. It ionises only the desired element and pollution of the trap can be reduced as the atom flux from the oven can be decreased compared to electron bombardment [47, 48, 50]. Furthermore, stray charges disturbing the trapping potential diminish and the ionisation can be localised to the trapping region.
This thesis describes the photoionisation of calcium using a 422 nm frequency-doubled light source and a laser diode at 377 nm which is a suitable loading method for both room temperature and cryogenic surface-electrode traps. It has been tested by loading ions in a surface-electrode trap at room-temperature. One future application already in progress is trapping at cryostatic temperatures.

The goal of the experimental work carried out for this thesis was the implementation of a photoionisation system for ^{40}Ca using a frequency-doubled system to generate 422 nm laser light, and a laser diode to provide 377 nm light. The thesis structure consists of a predominantly theoretical introduction in chapters 2 to 4, followed by the experimental implementation and results in chapters 5 and 6.
Chapter 2 presents the electronic structure of ^{40}Ca and introduces the theory of atom-light interactions. In chapter 3, nonlinear optics is reviewed to describe the process of frequency doubling. The considerations for the assembly of a build-up cavity are summarised in chapter 4 with an emphasis on the case of interest - a bow-tie resonator to enhance second-harmonic generation. A description of the experimental setup and its major components can be found in chapter 5. The apparatus and experiments carried out to test the implemented laser system are given in chapter 6.

2. Photoionisation of Calcium

In order to enable trapping in radio-frequency electric fields a technique to create charged ions from neutral atoms is required. The method which represents the foundation for this thesis is photoionisation; it uses the interaction of atoms with a light field for ionisation. Compared to the conventional electron bombardment method used before by our group [48, 49] and in other experiments e.g. [47, 50], it offers a number of advantages. For calcium, the photoionisation process can take place in two steps: the first being a resonant transition from $^1S_0$ to $^1P_1$ at a vacuum wavelength of 422.67262 nm (with slight differences for the various isotopes of calcium, see Tab. 2.1) and a second step from $^1P_1$ to the continuum. Thus, photoionisation permits distinct loading of not only a certain element, but it also offers the possibility to load selected isotopes. A further advantage is that the abdication of the electron beam reduces the amount by which the apparatus charges up. Also, the pollution of the surroundings can be reduced as photoionisation requires a weaker atom beam [47, 48, 50].

Isotope	Natural abundance (%)	Isotope shifts Ca^+ S-P	
		709285682 MHz (MHz)	422.67262 nm (nm)
^{40}Ca	96.941	0	0.00000
^{42}Ca	0.647	394	0.00023
^{43}Ca	0.135	612	0.00036
^{44}Ca	2.086	774	0.00046
^{46}Ca	0.004	1160	0.00069
^{48}Ca	0.187	1513	0.00090

Table 2.1.: Important isotopes of calcium with their natural abundance and the isotope shift in MHz and in nm relative to ^{40}Ca [50, 51].

The generation of calcium ions using photoionisation is the goal of the experiment this thesis is based on. Furthermore this contributes to the assembly of a cryogenic trapping system which requires a clean and efficient loading method, especially with regard to decreasing the heat load introduced by the oven. In the following, energy levels of atomic calcium (CaI) and singly ionised calcium (CaII) will be reviewed in Sec. 2.1 while a brief theoretical treatment of the photoionisation process will be given in Sec. 2.2.

2.1. Calcium

According to the criteria given by DiVincenzo [8] the implementation of quantum information processing is, amongst other things based on the existence of a scalable physical system with well defined qubits and a process which can initialise certain states. For trapped ions, the encoding of the qubit occurs in terms of long-lived atomic levels. $^{40}Ca^+$ is an ion that meets these conditions excellently and exhibits transitions for cooling and repumping at favorable wavelengths [52] which will be presented in the following.

2.1.1. Calcium I

Calcium is a group II element, a so-called earth alkaline. It naturally occurs in bound form: a special thermal process is needed to generate pure calcium. 19 different isotopes have been detected, the most important of which are presented in Tab. 2.1. The ground state electron configuration of calcium is $1s^2 2s^2 2p^6 3s^2 3p^6 4s^2$ and the two electrons in the outermost shell lead to a helium-like electronic structure. Therefore the element has an energy level scheme that consists of singlet and triplet states [49, 53].
For the further discussion in this thesis, the 422 nm wavelength transition is considered as it facilitates photoionisation. The ionisation process takes place in two steps (see Fig. 2.1): a transition from $^1S_0$ to $^1P_1$ at 422 nm wavelength and a second transition from the $^1P_1$ level to the continuum at any wavelength shorter than 389 nm. For the setup investigated here, the wavelength is chosen to be 377 nm as a diode at this wavelength was in stock. The first transition is a dipole-allowed step at a vacuum wavelength of 422.67262 nm for ^{40}Ca. However, this value varies for the different isotopes over a range of a few hundred MHz (see Tab. 2.1) [48, 50] which allows isotope selective photoionisation.

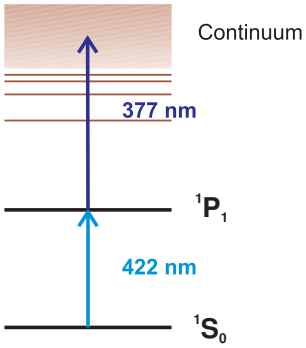

Figure 2.1.: Schematic of the levels used in calcium to obtain photoionisation with the laser wavelengths used in the experiment

2.1.2. Calcium II

The relevant electronic structure of the calcium ion enabling the encoding of a qubit is presented in Fig. 2.2 [10, 52, 54].

The qubit is implemented as a superposition of the $S_{1/2}$ ground state and the metastable $D_{5/2}$ state which represents a quadrupole transition at a wavelength of 729 nm with a lifetime of 1.16 s [11]. Hence, coherence times are long compared to experimental gate operation times that lie in the $\sim 100\,\mu$s range. A laser at 854 nm wavelength is used to depopulate the D state if necessary. Doppler cooling is accomplished using the transition at 397 nm while a laser at 866 nm wavelength serves as repumper [54]. A measurement is done using the so-called electron shelving method [12–14] which determines the internal state ($S_{1/2}$ or $D_{5/2}$) of the ion by selective excitation into a third short-lived state ($P_{1/2}$) [52]. Photons are scattered if and only if the coupled state was occupied. For calcium, the ion is excited at 397 nm wavelength, coupling the $S_{1/2}$ state to the short-lived $P_{1/2}$ state. If the $S_{1/2}$ state was occupied, photons are scattered and can be detected. As all transition wavelengths for manipulating and cooling can be obtained from diode based devices which are relatively inexpensive and easy to handle, calcium is a prominent candidate to implement ion-based quantum computation.

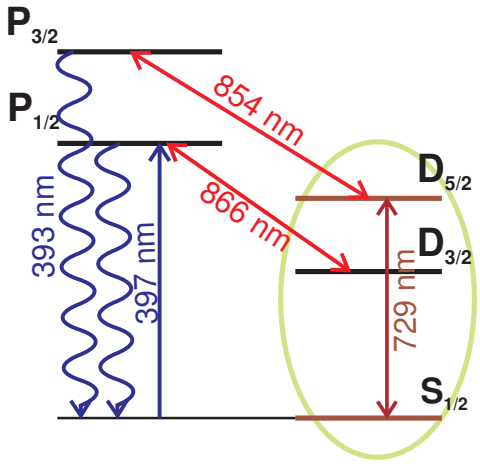

Figure 2.2.: Transitions and wavelengths relevant in Ca^+ to accomplish quantum logic processes. Qubits are implemented as superpositions of the states $S_{1/2}$ and $D_{5/2}$ [54] emphasised here with a green ellipse.

2.2. Atom-light interaction

The atomic response to radiation forms the basis of numerous experiments. It is also used in the process of photoionisation - the ionisation of atoms using light of certain wavelengths. Hence, a theoretical description should be at hand to quantitatively describe the effects occurring. In the following section, a brief introduction will be given to the topic. Further treatments can be found in [55–59]. For the purpose of this description the interaction will be treated semiclassically, referring to the atom as a quantum system and regarding the light as a non-quantised, electromagnetic field. This approach is appropriate, as the lasers used as light sources generate a large number of photons. Thus, back-action effects on the field are neglected if an atom absorbs or emits a photon - photonic losses and gains do not effect the field. Given these prerequisites the Schrödinger equation for atom-light interactions can be written as [55, 57]

$$\boxed{\left\{\frac{p^2}{2m} + V(r) - e\mathbf{r}\cdot\mathbf{E}(\mathbf{r_0},t)\right\}|\Psi(\mathbf{r},t)\rangle = i\hbar\frac{\partial}{\partial t}|\Psi(\mathbf{r},t)\rangle} \tag{2.1}$$

In this equation, $\frac{p^2}{2m}$ is the kinetic energy of an electron (mass m, momentum p) bound to a nucleus due to the potential energy $V(r)$. The term $e\mathbf{r}\cdot\mathbf{E}(\mathbf{r_0},t)$ denotes the energy introduced by the interaction of the atom with the external light field. By defining the unperturbed Hamiltonian of the atom $\mathcal{H}_0 = \frac{p^2}{2m} + V(r)$ and the Hamiltonian for the perturbation by the light field $\mathcal{H}_1 = -e\mathbf{r}\cdot\mathbf{E}(\mathbf{r_0},t)$ the overall Hamiltonian can be rewritten as

$$\mathcal{H} = \mathcal{H}_0 + \mathcal{H}_1. \tag{2.2}$$

2.2.1. Two-level system

An adequate description of phenomena such as photon absorption and emission can be derived using the two-level approximation. It represents a reduction of complicated atomic systems to two levels which are resonant or nearly resonant with the external driving field as depicted in Fig. 2.3. All other levels of the atom are neglected. This description is analogous to a spin 1/2 particle in an external magnetic field.

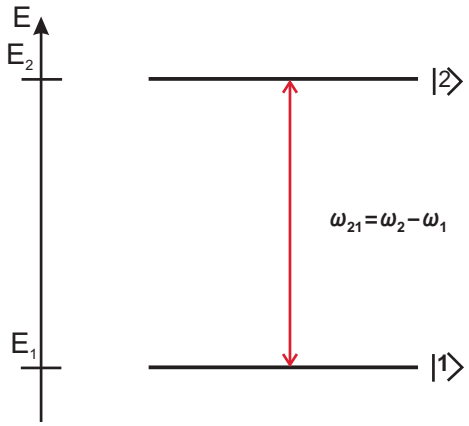

Figure 2.3.: The schematic illustrates a two-level atom interacting with light. The abbreviation $|1\rangle$ indicates the ground state and $|2\rangle$ denotes the excited state. ω_{21} is the resonance angular frequency of the transition.

The interaction of atoms with light is formally described by time dependent perturbation theory. The atomic Hamiltonian is the same as in Eq. 2.1, where the interaction Hamiltonian is modified according to the incident light field $\mathcal{H}_1 = e\mathbf{r} \cdot \mathbf{E_0} \cos(\omega t)$ with an amplitude vector $\mathbf{E_0}$ and angular frequency ω. A general solution to this can be formulated using an expansion series but is beyond the scope of this thesis. Hence, only the results of this method will be used in the following. Detailed treatments can be found in quantum mechanics textbooks such as [60].

A description of the atom-light interaction can be accomplished, following three steps:

1. Description of the initial state as a wave function,

2. Solution of the Schrödinger equation to calculate the time evolution of the system including the interaction,

3. Analysis of the population transfer probability to the excited state.

For a two-level atom, these steps can be carried out explicitly. The initial wave function for the two-level system results from a superposition of time dependent solutions for the unperturbed Hamiltonian $\mathcal{H}_0$

$$\Psi(\mathbf{r}, t) = c_1(t)\,|1\rangle\, e^{iE_1 t/\hbar} + c_2(t)\,|2\rangle\, e^{iE_2 t/\hbar}. \tag{2.3}$$

If this initial state is substituted into Eq. 2.1 a system of coupled differential equations for the constants c_1 and c_2 is obtained

$$\begin{aligned} \dot{c_1} &= -i\Omega_{\mathrm{R}} \cos(\omega t) e^{-i\omega_{21} t} c_2 \\ \dot{c_2} &= -i\Omega_{\mathrm{R}} \cos(\omega t) e^{i\omega_{21} t} c_1. \end{aligned} \tag{2.4}$$

For convenience, the resonance angular frequency $\omega_{21} = \omega_2 - \omega_1$ and the Rabi frequency $\Omega_{\mathrm{R}} = \frac{\langle 1|e\mathbf{r}\cdot\mathbf{E_0}|2\rangle}{\hbar} = \frac{\mathbf{d_{12}}\mathbf{E_0}}{\hbar}$ have been introduced. $\mathbf{d_{12}} = e\,\langle 1|\mathbf{r}|2\rangle$ denotes the dipole matrix element.
Rewriting the field oscillation in terms of exponential functions, the rapidly oscillating terms at frequency $(\omega_{21} + \omega)$ can be neglected by making the **Rotating Wave Approximation**. This is valid as there is almost no contribution of these terms to the time evolution of the

system (provided $\Omega_R << \omega_{21}$).

$$\dot{c_1} = -i\frac{\Omega_R}{2}e^{-i(\omega_{21}-\omega)t}c_2$$
$$\dot{c_2} = -i\frac{\Omega_R}{2}e^{i(\omega_{21}-\omega)t}c_1 \tag{2.5}$$

Solving Eq. 2.5 for a monochromatic light source leads to expressions for the coefficients $c_1(t)$ and $c_2(t)$ dependent on the initial condition of the quantum system

$$c_1(t) = \left[\left\{\cos\left(\frac{\Omega t}{2}\right) - \frac{i\Delta}{\Omega}\sin\left(\frac{\Omega t}{2}\right)\right\}c_1(0) + i\frac{\Omega_R}{\Omega}\sin\left(\frac{\Omega t}{2}\right)c_2(0)\right]e^{i\Delta t/2}$$
$$c_2(t) = \left[\left\{\cos\left(\frac{\Omega t}{2}\right) + \frac{i\Delta}{\Omega}\sin\left(\frac{\Omega t}{2}\right)\right\}c_2(0) + i\frac{\Omega_R}{\Omega}\sin\left(\frac{\Omega t}{2}\right)c_1(0)\right]e^{-i\Delta t/2}. \tag{2.6}$$

The new parameters in Eq. 2.6 are the detuning $\Delta = (\omega_{21} - \omega)$, and the flopping frequency $\Omega = \sqrt{\Omega_R^2 + \Delta^2}$ [59]. The transition probability is defined as $\mathsf{P}_{21}(t) = |\langle 2|\Psi(\mathbf{r},t)\rangle|^2$. For the case where the atom is initially in the ground state[1] the coefficients are $c_1(0) = 1$ and $c_2(0) = 0$. With these constraints the probability of finding the atom in the excited state after a certain time, t, is

$$\mathsf{P}_{21}(t) = |c_2(t)|^2 = \left(\frac{\Omega_R}{\Omega}\right)^2\sin^2\left(\frac{\Omega t}{2}\right) = \left(\frac{\Omega_R}{2}\right)^2\mathrm{sinc}^2\left(\frac{\Omega t}{2}\right). \tag{2.7}$$

If the incident monochromatic light is exactly resonant ($\omega = \omega_{21}$), the detuning is zero, $\Omega = \Omega_R$ and the probability to find the atom in the excited state simplifies to $\mathsf{P}_{21} = \sin^2(\Omega_R t/2)$.

The excitation probability, P_{21}, for a resonantly driven transition is plotted in Fig. 2.4. Corresponding to the choice of the initial conditions, it starts with zero probability of finding the population in the excited state. With time evolving the probability cycles between zero and one, denoting a periodic transition of the atom from ground state to excited state.

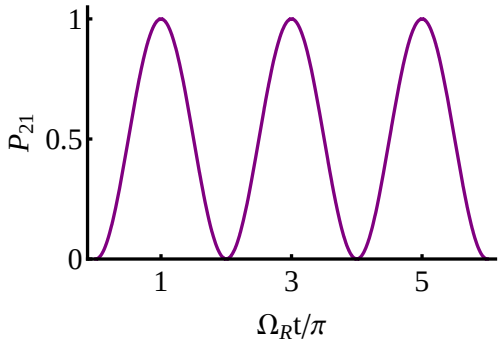

Figure 2.4.: Occupation probability for the upper level in the resonant case. The population of the excited state is zero at the beginning of the interaction. At later times the population is transferred from the ground to the excited state and then continues to cycle between the two levels.

2.2.2. Rate equations and bound-free transition

So far, the $^1S_0$ to $^1P_1$ transition has been dealt with explicitly. When considering the second ($^1P_1$ to continuum) transition certain simplifications can be made. Following the formalism of

[1] For the photoionisation process, this is a good assumption.

Einstein [61] it will now be shown that, in the limit of saturation, the time evolution of the S-P transition can be neglected, and the system can be treated as having a constant excited population of 50 %.

The description of the interaction of a two-level atom with electromagnetic radiation as given previously, reviews the population behaviour but does not take into account explicitly the processes leading to the phenomenon, namely spontaneous and stimulated emission and absorption of photons. However, Einstein derived a way of treating this processes by introducing the rate equation which links the population change to the corresponding absorption and emission (spontaneous and stimulated) transitions [57, 61–63]. For a two-level atom as illustrated in Fig. 2.3 interacting with a field of energy density $\rho(\omega)$ the rate equation is written as

$$\frac{\mathrm{d}N_1}{\mathrm{d}t} = -\frac{\mathrm{d}N_2}{\mathrm{d}t} = N_2 A_{21} - N_1 B_{12}\rho(\omega) + N_2 B_{21}\rho(\omega) \tag{2.8}$$

with N_1 the population of the lower energy level, N_2 the population of the higher energy level, A_{21} the Einstein coefficient for spontaneous emission from energy level 2 to energy level 1, B_{12} denoting the Einstein coefficient for absorption of a photon and B_{21} the Einstein coefficient for stimulated emission of a photon.
The energy density of the field saturates the transition if the stimulated emission is equal to the spontaneous emission, which can be formulated as

$$\rho(\omega)_s B_{21} = A_{21}. \tag{2.9}$$

If the energy density of the incident electromagnetic radiation exceeds the saturation value for the atomic transition, the population is equally divided between the two energy levels [63]. For the setup used in this thesis, the light source to drive the transition is a laser with a frequency equal to the transition frequency of the atom. Hence, the intensity is higher than the intensity needed to saturate the transition, and for the further investigation the assumption of having half the atoms in the upper level $^1\mathrm{P}_1$ reduces the process to a bound-free transition between $^1\mathrm{P}_1$ and the continuum states.

An atom is ionised if it absorbs a photon carrying an energy greater than the ionisation energy and thus undergoes a transition to a continuum state [62]. This process generates an atomic ion and a free electron. Probabilities for exciting an atom to the continuum, and thereby ionising it are expressed in terms of the photoionisation cross section, Q. This photoionisation cross section can be related to the oscillator strength, f_{ij}, connected to the line strength of the transition as

$$Q_{ij} = \frac{\pi e^2 h}{mc}\frac{\mathrm{d}f_{ij}}{\mathrm{d}E}. \tag{2.10}$$

In this equation, the cross section of a photoionisation process is related to the oscillatory strength change per energy interval. e denotes the elementary charge, h is the Planck constant, c is the velocity of light and m is the electron mass. Eq. 2.10 can be rewritten given the energy interval, dE, in terms of Rydbergs ($= \hbar^2/(2a_0^2 m)$ where a_0 is the Bohr radius)

$$Q_{ij} = 4\pi^2 \alpha a_0^2 \frac{\mathrm{d}f_{ij}}{\mathrm{d}\epsilon} \tag{2.11}$$

with α being the fine-structure constant. For simple cases, the derivative $df/d\epsilon$ can be derived by considering a bound-bound transition where the radial dipole matrix element is exchanged against the one for a bound-free transition. The spectral function obtained can then be extrapolated to find a discrete analogon

$$\frac{\Delta f_{ij}}{\Delta\epsilon} = \frac{Z_\mathrm{c}}{2|\epsilon_{n_j}|^{3/2}} f_{ij}, \tag{2.12}$$

denoting the binding energy for the excited electron in the upper state as $|\epsilon_{n_j}|$ (in Rydbergs) and $Z_c = (Z - N + 1)$ the effective core charge. If a single valence electron is subject to a photoionisation process, a hydrogen-like approximation can be implemented which leads to the expression

$$\overline{Q}_{n,\epsilon} \cong \frac{64\pi\alpha a_{0^2} Z_c^4}{3^{3/2} n^5 \epsilon^3} = 7.91 \times 10^{-18} \frac{n}{Z_c^2} \left(\frac{\epsilon_n}{\epsilon}\right)^3 \text{ cm}^2. \tag{2.13}$$

In Eq. 2.13 the photon energy is denoted ϵ (given in Rydbergs) and the threshold ionisation energy for the shell n is denote $\epsilon_n = Z_c^2/n^2$.

For the ionisation of ^{40}Ca a cross section of 0.55 Mb (1 Mb $= 10^{-22}$ m^2) can be calculated using Eq. 2.13 and a wavelength of 377 nm. This value gives a lower limit for the cross section of the process as it deals only with the the model simplified to the hydrogen-like behaviour. Nonetheless, the existence of resonances could easily increase the value by a factor of hundred or more, as was the case for the cross section measured by Lucas et al. for the same transition, at excitation wavelength of 377 nm [50]. As the excitation from ^{1}P$_1$ to the continuum is driven using a laser at 389 nm at the ionisation threshold a two-electron resonance behaviour increases the cross section for the process from 0.6 Mb as predicted by the hydrogen-like approximation, to the value (170 ± 60) Mb.

From the structure of Eq. 2.13 which is proportional to ϵ^{-3} it is obvious that for higher energies (shorter wavelengths) the cross section decreases. Therefore, it is beneficial for a large ionisation rate to keep the wavelength of the laser used in the experiment close to the ionisation threshold.

3. Frequency Doubling

Ever since a laser was first operated in 1960 [64] nonlinear optics has been of interest [65–67]. Observations conflicted with preceding assumptions concerning light passing through an optical medium. Assumptions of the independence of refractive indices and absorption indices on intensity, the constancy of an optical frequency when passing through a medium and the superposition principle no longer held. Instead it could be verified experimentally that the refractive index in nonlinear optics depends on the light intensity, the optical frequency can change and the superposition principle is violated [66]. Taking advantage of such phenomena led to an abundance of applications with frequency conversion systems as one example.
Frequency doubling or second-harmonic generation (SHG) is of particular importance as it can supply coherent light at wavelengths that can not be generated easily using laser diodes. Diodes in the yellow and orange wavelength range can not be produced due to a lack of materials with a corresponding bandgap to emit these wavelengths. The extension to wavelengths lower than 370 nm is currently not possible due to the fabrication techniques. The fabrication of diodes in the blue wavelength range is limited due to a lack of consumer demand which controls the development of products in this sector. While the market for red and infrared diodes is large and the 'blu ray' technology increased the demand for diodes at 405 nm, the selection of blue wavelengths is limited.

The photoionisation of calcium depends on a transition at 422 nm. As the availability of such diodes is severely restricted, SHG presents a useful technique to meet this challenge. In Sec. 3.1 the theory of nonlinear optics will be briefly reviewed, deriving the nonlinear wave equations with emphasis on second-harmonic generation and the mechanisms to optimise it. The basics for a realistic case using a Gaussian laser beam will be dealt with in Sec. 3.2.

3.1. Nonlinear optics

The interaction of an electromagnetic field with a dielectric medium results in the generation of a polarisation within the material. Considering classical light sources, the response of the medium will generally be linear, as the light intensity is weak. In the simplest case the polarisation density, $\mathcal{P}$, is proportional to the number density of dipole moments, N, and the dipole moment p.

$$\mathcal{P} = Np = \epsilon_0 \chi E \tag{3.1}$$

As can be seen in Eq. 3.1, the polarisation of the medium is proportional to the external electrical field E, the permittivity of free space, ϵ_0, and the electric susceptibility of the medium χ. Lasers, as coherent light sources of higher intensities, may excite a nonlinear response $\mathcal{P}^{NL}$ as well as a linear response $\mathcal{P}^{LIN}$ of the medium. One approach to express the nonlinearity is to claim that the number density of dipoles involved, N, is dependent on the optical field. Back action of the polarisation onto the incident field changes the intensity, leading to a change in the number of dipoles involved [66].

Even for focused laser light the electrical field incident on a medium is small compared to

interatomic electrical fields. Hence, the relation between the polarisation and the field can be expressed by a series expansion around a small electric field value ($E = 0$)

$$\mathbf{P}(\mathbf{r},t) = \mathbf{P}^{\mathrm{LIN}}(\mathbf{r},t) + \mathbf{P}^{\mathrm{NL}}(\mathbf{r},t) = \epsilon_0 \left(\chi^{(1)}\mathbf{E}(\mathbf{r},t) + \chi^{(2)}\mathbf{E}(\mathbf{r},t)\mathbf{E}(\mathbf{r},t) + \mathcal{O}(h)...\right) \tag{3.2}$$

In this equation $\chi^{(1)}$ is the first order susceptibility while $\chi^{(2)}$ expresses the second order susceptibility of the medium. Higher order terms $\mathcal{O}(h)$ exist but their treatment is beyond the scope of this thesis.
As can be seen from Eq. 3.2 every order of susceptibility higher than 1 gives rise to new frequencies due to the product of the electrical field terms. The mixing product of the exponential part of the electric field terms leads to the creation of field terms at new frequencies[1]. With this consideration a general expression for the second order polarisation can be introduced [65]

$$P_i(\omega) = \sum_{jk} \chi^{(2)}_{ijk}(\omega;\omega_m\omega_n) E_j(\omega_m) E_k(\omega_n). \tag{3.3}$$

Eq. 3.3 describes the ith component of the polarisation in terms of the second order susceptibility $\chi^{(2)}_{ijk}(\omega;\omega_m\omega_n)$ and the related mixing field components $E_j(\omega_m)$ and $E_k(\omega_n)$, ($\{i,j,k\} = \{x,y,z\}$). The notation $\chi^{2}_{ijk}(\omega;\omega_m\omega_n)$ points out that the susceptibility is connected to a field with frequency ω generated by mixing two fields with frequencies ω_n and ω_m. For ordinary frequency doubling all fundamental waves have the same frequency i.e. there is a of degeneracy whereby the frequencies in Eq 3.3 can be written as $\omega_m = \omega_n = \omega_1$, $\omega_2 = 2\omega_1$.

3.1.1. Nonlinear wave equation

After describing the polarisation arising from the interaction of an electromagnetic field with a nonlinear medium, the propagation of a wave in such a medium will be presented briefly in the following. A more detailed consideration can be found in [65, 66, 68] and a short derivation is presented in App. A.1.
An electromagnetic wave travelling through matter has to satisfy the wave equation

$$\left(\nabla^2 - \frac{1}{c^2}\frac{\partial^2}{\partial t^2}\right)\mathbf{E}(\mathbf{r},t) = \frac{1}{\epsilon_0 c^2}\frac{\partial^2}{\partial t^2}\mathbf{P}(\mathbf{r},t). \tag{3.4}$$

Here, c is the speed of light in vacuum, ϵ_0 is the permittivity in free space, $\mathbf{E}(\mathbf{r},t)$ denotes the electrical field and $\mathbf{P}(\mathbf{r},t)$ is the related polarisation of the medium, containing linear and nonlinear responses. Eq.3.4 can be rewritten using the fact that the linear response of the medium, $\mathbf{P}^{\mathrm{LIN}}$, effects only fundamental waves driving the process and hence can be described in terms of the refractive index ($n^2 = 1 + \chi^{(1)}$) $\mathbf{P}^{\mathrm{LIN}} = \epsilon_0(n^2 - 1)\mathbf{E}(\mathbf{r},t)$. This leads to a new wave equation to describe the propagation of electromagnetic waves in a dispersive dielectric medium:

$$\left(\nabla^2 - \frac{n^2}{c^2}\frac{\partial^2}{\partial t^2}\right)\mathbf{E}(\mathbf{r},t) = \frac{1}{\epsilon_0 c^2}\frac{\partial^2}{\partial t^2}\mathbf{P}^{\mathrm{NL}}(\mathbf{r},t). \tag{3.5}$$

This equation connects the wave $\mathbf{E}(\mathbf{r},t)$ with the nonlinear response $\mathbf{P}^{\mathrm{NL}}(\mathbf{r},t)$ of the medium. c denotes the velocity of light and n the refractive index. Using the slowly varying envelope approximation, which assumes a slow change of the wave amplitude compared to its wavelength, and splitting it into components of different frequency (l denotes the summation index

[1] Consider the multiplication of the exponentials like $e^{i\omega_n t} \cdot e^{i\omega_m t} = e^{i(\omega_n+\omega_m)t}$

cf. App. A) it reads in one dimension[65]

$$\left(2ik\frac{\partial}{\partial z}\underbrace{-k^2+\frac{n^2(\omega_l)\omega_l^2}{c^2}}_{=0}\right)\mathcal{E}(z)=\frac{\omega_l^2}{\epsilon_0 c^2}\mathcal{P}_l(z)e^{-ikz}. \tag{3.6}$$

This can be rewritten in terms of $\mathcal{P}_l(z)e^{-ikz}=4\epsilon_0 d_{\text{eff}}\mathcal{E}_m\mathcal{E}_n e^{-i\Delta kz}$ with d_{eff} the effective susceptibility of the material and the phase mismatch $\Delta k=k-k_m-k_n$.

$$\begin{aligned}\frac{d\mathcal{E}_3(\omega)}{dz}&=\frac{2i\omega d_{\text{eff}}}{cn(\omega)}\mathcal{E}_1\mathcal{E}_2e^{-i\Delta kz}\\ \frac{d\mathcal{E}_1^*(\omega_1)}{dz}&=\frac{-2i\omega_1 d_{\text{eff}}}{cn(\omega_1)}\mathcal{E}_3^*\mathcal{E}_2e^{-i\Delta kz}\\ \frac{d\mathcal{E}_2^*(\omega_2)}{dz}&=\frac{-2i\omega_2 d_{\text{eff}}}{cn(\omega_2)}\mathcal{E}_1\mathcal{E}_3^*e^{-i\Delta kz}\end{aligned} \tag{3.7}$$

The effective susceptibility, d_{eff}, arises from symmetry effects in crystals [69] and can be found for many nonlinear media using the SNLO software[2].

Second-Harmonic Generation (SHG)

An interesting special case of the coupled wave equations (Eq. 3.7) is second-harmonic generation (SHG) or frequency doubling. It describes the interaction of a nonlinear medium with an electromagnetic field of angular frequency ω_1 providing a response at the frequency $\omega_2=2\omega_1$.
This mechanism has to respect the fundamental laws of energy conservation (3.8) and momentum conservation (3.9)

$$\hbar\omega_2=2\hbar\omega_1 \tag{3.8}$$

$$\hbar\mathbf{k_{2\omega}}=2\hbar\mathbf{k}_\omega. \tag{3.9}$$

These principles set constraints on the interaction of the waves formulated in the **frequency matching** and **phasematching** conditions.
As frequency doubling describes the interaction of the medium with one electric field (the fundamental field), the number of coupled wave equations (Eq. 3.7) is reduced to two. Introducing a normalised amplitude $\mathcal{A}_l=\sqrt{\frac{n(\omega_l)}{\omega_l}}\mathcal{E}_l$ and a coupling coefficient $\Gamma=\frac{2d_{\text{eff}}}{c}\sqrt{\frac{\omega^3}{n_{2\omega}n_\omega^2}}$ [65] they read as

$$\begin{aligned}\frac{d\mathcal{A}_{2\omega}}{dz}&=i\Gamma\mathcal{A}_\omega^2e^{-i\Delta kz}\\ \frac{d\mathcal{A}_\omega}{dz}&=i\Gamma\mathcal{A}_{2\omega}\mathcal{A}_\omega^*e^{i\Delta kz}.\end{aligned} \tag{3.10}$$

General solutions for plane waves are formulated in the weak or the strong conversion regime.

[2] This software is available as a free download at http://www.as-photonics.com/SNLO.html

Weak and Strong conversion

The weak conversion regime describes a situation where the generated wave radiating at the doubled frequency does not significantly diminish the pump (fundamental) wave. Therefore, only the first equation from 3.10 plays a role. Solving this problem for the interaction of electromagnetic waves in a crystal with length L_c, a simple integration leads to the result

$$A_{2\omega} = \Gamma L_c \mathcal{A}_\omega^2 e^{i\Delta k L_c/2} \mathrm{sinc}\left(\Delta k L_c/2\right). \tag{3.11}$$

where $\mathrm{sinc}(x) = \sin(x)/x$.
As the intensity is proportional to the square of the normalised amplitude $I \propto |\mathcal{A}|^2$, it varies as the square of the crystal length. The behaviour of the phase mismatch is contained in the argument of the *sinc* term. From the condition $\mathrm{sinc}(\Delta k L_c/2) = 0$ the so-called coherence length can be defined. This is the length at which a phaseshift of π is introduced, corresponding to the "half period of the growth and decay cycle of the second harmonic" [70].

$$l_c = \frac{\pi}{\Delta k} = \frac{\lambda}{4(n_{2\omega} - n_\omega)} \tag{3.12}$$

It is clear that constant growth of the intensity with crystal length is only possible for perfect phasematching, where $\Delta k = 0$. The weak conversion regime is used in the photoionisation experiment that forms the basis for this thesis.

In contrast to the weak case, when considering **strong conversion** both Eqs. 3.10 must be taken into account as the generated second-harmonic wave acts back on the incident wave, damping its intensity. Solutions for the strong conversion case can be found in [65, 68].

3.1.2. Birefringent phasematching and quasi-phasematching

Because of its wavelength dependence, the refractive indices of fundamental and second-harmonic waves generally differ: $n(\omega) \neq n(2\omega)$. This gives rise to destructive interference between second-harmonic waves that are generated at different locations in the crystal, as they have different phases. In order to accomplish frequency doubling effectively some procedure has to be applied to maintain the relative phase between the second-harmonic waves. Different schemes have been established exhibiting a variety of advantages and disadvantages. Very common are birefringent phasematching techniques (PM) and quasi-phasematching (QPM) techniques. The former tries to manipulate the difference in refractive indices of fundamental and second-harmonic wave by means of the birefringence that occurs in different media. The latter reverses the sign of the nonlinear susceptibility with a certain periodicity. Additional but less widely used schemes are discussed in detail in [71].

Birefringent Phasematching

In order to achieve efficient SHG, the refractive indices of the fundamental and second-harmonic wave have to be equal leading to a nominally infinite coherence length ($l_c < L_c$) (compare with Eq. 3.12). By matching the refractive indices $n_\omega = n_{2\omega}$ the phase velocity of the interacting waves are no longer different and the intensity of the second harmonic can grow quadratically with crystal length. The birefringence phenomenon occurring in

anisotropic media is used to satisfy the condition $\Delta k = 0$. These materials, which are in practice mostly uniaxial crystals, have refractive indices that are not only dependent on the wavelength, but also on the polarisation of the wave and their direction with respect to the principal axis, which gives additional degrees of freedom to meet the constraint mentioned. Experimentally, the polarisation dependence can be used to fulfil $n_\omega = n_{2\omega}$ and achieve efficient SHG. To exploit this technique for a broad range of wavelengths, angle or temperature tuning is used (see Fig. 3.1a).

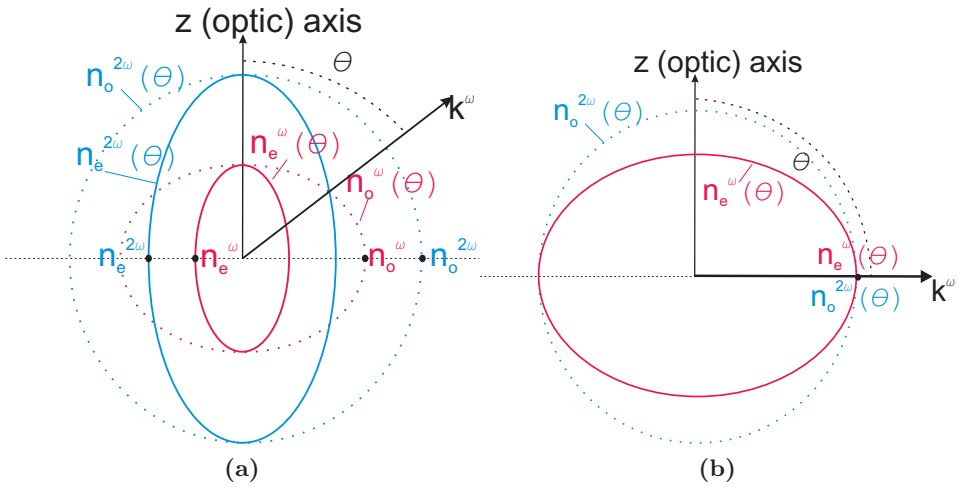

Figure 3.1.: (a) Index surfaces for ordinary (dotted lines) and extraordinary (solid lines) rays in a negative ($n_\mathrm{e} < n_\mathrm{o}$), uniaxial crystal. The blue lines depict the refractive index of the second harmonic while the red ones show the fundamental refractive indices. The point of intersection between the extraordinary second harmonic and the ordinary fundamental wave determines an angle θ at which the phasematching condition is fulfilled [65, 66, 72].(b) Indicatrix in case of temperature tuning. The fundamental wave is set as the extraordinary beam and the second-harmonic wave follows the ordinary beam path. Phasematching takes place at an angle of $\theta = 90\,^\circ$ with appropriate choice of temperature to match the refractive indices [71].

- **Angle or critical tuning**
  The already mentioned dependence of the refractive indices on the angle, θ, between the propagating wave and the optical axis can be used to correct for a phase mismatch. For uniaxial crystals, the propagation of a wave can be described by the formula

$$\frac{1}{n^2(\theta)} = \frac{\cos^2(\theta)}{n_\mathrm{o}^2} + \frac{\sin^2(\theta)}{n_\mathrm{e}^2} \tag{3.13}$$

  introducing the ordinary refractive index n_o and the extraordinary refractive index n_e. If the polarisation of the second-harmonic wave is orthogonal to the polarisation of the fundamental wave the phasematching is termed as **Type I phasematching**. If the fundamental wave consists of an ordinary and an extraordinary ray, the second-harmonic wave could be either of the ordinary type or the extraordinary type. This is called **Type II phasematching**. Fig. 3.1a depicts the situation using Eq. 3.13 for a negative uniaxial crystal ($n_\mathrm{e} < n_\mathrm{o}$) and type I phasematching. It illustrates that an intersection of the refractive indices for ordinary fundamental wave and extraordinary second-harmonic wave exists. If the incidence angle with respect to the optical axis is chosen to accord with this intersection, the phasematching condition is fulfilled and the generation of the frequency doubled wave will be efficient.

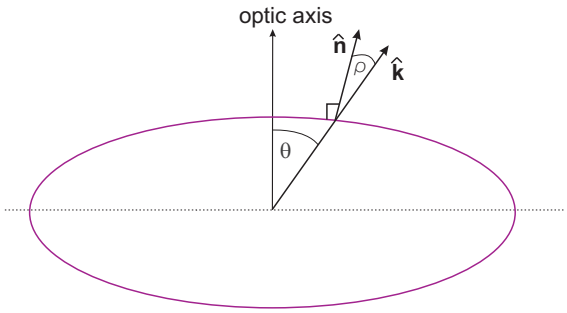

Figure 3.2.: Index ellipsoid for a refractive index. This illustrates the connection between the propagation direction, **k**, and the normal direction, **n**, that is parallel to the Poynting vector. The angle between the optical axis and the propagation direction is denoted θ. The angle between the normal vector and the propagation vector is ρ, the so-called walk-off angle [71].

A drawback that can occur with angle tuning is the phenomenon of walk-off. It describes the incongruity of the second-harmonic's propagation direction and its energy flow. The energy flow is represented by the Poynting vector which has the same direction as the normal vector to the ellipsoid depicting the refractive index. The situation is shown in Fig. 3.2. Walk-off leads to an elliptic beam profile of the second-harmonic wave as well as to a lower generated power.

- **Temperature or non-critical tuning**
  It is obvious from Fig. 3.2 that the disadvantages of walk-off in angle phasematching can be overcome if the angle between the propagation direction and the optical axis is equal to $\theta = 90\,^\circ$ (cf. Fig. 3.1b). Thus, the normal vector and the propagation vector have the same direction, leading to a walk-off angle $\rho = 0\,^\circ$. Both, the polarisation of the fundamental and second-harmonic waves and the angle they enclose with the optical axis are determined. Hence, the only possibility to achieve phasematching for the wavelength of interest relies on the different temperature dependence of the refractive indices at fundamental and harmonic wavelength. As the tolerances for angular deviations are larger in temperature tuning compared to angle tuning, the former is also referred to as non-critical PM while the latter is called critical PM.

Quasi-Phasematching (QPM)

QPM does not match the refractive indices to achieve phasematching. It maintains the average relative phase thus enabling the second-harmonic intensity to grow. As one coherence length is half a period of the growth and decay cycle of the second harmonic an inversion of the relative phase is forced after an odd number of coherence lengths. Changing the sign of power flow and thereby the relative phase between the incident and second-harmonic wave after an odd number of coherence lengths, the process is reset just at the maximum of a growth cycle. This way effective intensity increase can be achieved. If the reversal of power flow takes place every coherence length, the process is called first order QPM.

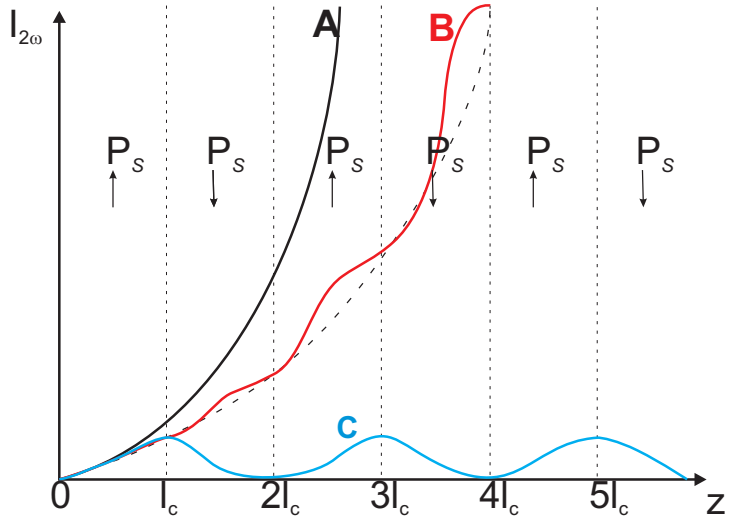

Figure 3.3.: Intensity of the second-harmonic wave as a function of the crystal length in z direction for different phasematching cases [70, 73]. Curve A corresponds to the PM case; Curve B shows the first order quasi-phasematching effect for sign inversion of the spontaneous polarisation, P_S, every coherence length; Curve C represents the behaviour for the non phasematched case.

QPM does not produce doubled frequencies as efficiently as PM, due to slower intensity growth rates as can be seen in Fig. 3.3. Nonetheless, it is an adequate alternative and allows the prospect of using isotropic media (such as GaAs) and the freedom of polarisation choice. The theoretical approach to SGH with quasi-phasematching is similar to the case for homogeneous media. Only the basic differences will be pointed out here. For a more detailed consideration the reader is referred to [70]. In contrast to the phasematching techniques, in QPM the nonlinear susceptibility changes its sign, leading to a change in the spontaneous polarisation, P_{S}, represented in Fig. 3.3. This periodic pattern can be taken into account using a Fourier series to denote the spatially varying susceptibility.

$$d(z) = d_{\mathrm{eff}} \sum_{m=-\infty}^{\infty} G_m e^{-iK_m z} \qquad G_m = \frac{2}{m\pi} \sin(m\pi L_{\mathrm{c}}/\Lambda) \tag{3.14}$$

The function G_m represents a Fourier coefficient taking into account the geometric period length, Λ. Inserting the Fourier series into the solution achieved for the coupled wave equations in the second-harmonic case and assuming weak conversion (Eq. 3.10) leads to a simplification: only the Fourier component which fulfils the phasematching condition (Eq. 3.15) is taken into account while all others contribute weakly. The condition to achieve QPM is met if the phase mismatch of the second-harmonic generation, Δk, equals the reciprocal domain space vector $K_m = \frac{2\pi m}{\Lambda}$, i.e. if there is a phase inversion at the domain edge

$$\Delta k = K_m. \tag{3.15}$$

Hence, $d(z)$ is reduced to its relevant harmonic, d_{Q}, which is related to the Fourier component meeting the phasematching condition as

$$d_{\mathrm{Q}} = d_{\mathrm{eff}} G_m. \tag{3.16}$$

Analysing the first order QPM effect ($m = 1$) for the optimum condition where $\sin(\pi L_{\mathrm{c}}/\Lambda) = 1$, it happens that the effective susceptibility is reduced by a factor of $2/\pi$

compared to the PM case

$$d_{\mathrm{Q}} = d_{\mathrm{eff}} \frac{2}{\pi}. \tag{3.17}$$

The expression for the second-harmonic field generated under these conditions is

$$A_{2\omega} \approx i \frac{\Gamma}{d_{\mathrm{eff}}} d_{\mathrm{Q}} L_c A_{\omega}^2 e^{i\Delta k L_{\mathrm{c}}/2} \mathrm{sinc}(\Delta k L_{\mathrm{c}}/2). \tag{3.18}$$

As for phasematching, angle and temperature tuning are needed to establish second-harmonic generation for the wavelength at hand. Formulas to derive tolerances for temperature and for angle tuning are given in general terms in [70] and specifically for ppKTP (periodically poled potassium titanyl phosphate $KTiOPO_4$) in [71]. Here, only the outcome of the calculations will be summarised for the parameters used in the experiment described in this work. Given this, a flux grown material is assumed, with a pump wavelength of $\lambda_\omega = 844\,\mathrm{nm}$, a harmonic wavelength of $\lambda_{2\omega} = 422\,\mathrm{nm}$, a period length of $\Lambda = 3.9582\,\mu\mathrm{m}$, a crystal length of $L_{\mathrm{c}} = 10\,\mathrm{mm}$ and a thermal expansion coefficient of $\alpha = 0.6 \times 10^{-6}$. With these parameters, the temperature bandwidth is $\Delta T_{\mathrm{FWHM}} = 1.4\,^{\circ}\mathrm{C}$ and the angular bandwidth of $\Delta\theta_{\mathrm{FWHM}} = 0.039\,\mathrm{rad} = 2.2\,^{\circ}$, assuming normal incidence. Thus, a temperature change of $0.7\,^{\circ}\mathrm{C}$ or a change of the incident angle of $1.1\,^{\circ}$ can halve the power of the second harmonic generated.

3.2. SHG using lasers as coherent light source

The importance of lasers for the development of nonlinear optics has been pointed out previously. Laser beams are well described in terms of Gaussian waves. In contrast to plane waves that can be seen as unbounded, a Gaussian beam has a minimum waist w_0 that can be varied. Focusing a laser beam leads to a smaller beam area at a certain point, increases the intensity there. However, the smaller the focus, the shorter is the confocal parameter. Considering the interaction with a nonlinear crystal we conclude from Eq. 3.11 that the intensity of a second-harmonic wave is dependent on the square of the fundamental's intensity. Thus it would be tempting to simply increase the intensity of the laser by focusing it. From Eq. 3.11 it is also obvious that the length of the crystal plays an important role. Therefore, merely confining the beam more strongly would not lead to the desired effect which is a large second-harmonic intensity. An optimisation between strong focusing leading to high maximum intensities, and weak focusing leading to longer interaction lengths has to be found.
The formal treatment given here is based on the article of Boyd and Kleinman [74] which was derived using the c.g.s. system. Only the basic results of this will be presented here but a more detailed approach can be found in App. A.2 and of course, in the original paper, as well as in reference [71] which uses the international units system (SI).

The formal treatment divides the nonlinear crystal into segments of thickness dz. Each segment interacts with the fundamental wave and contributes a certain amount to the generated second-harmonic wave. This amount differs for each segment due to the focusing of the beam, as the beam size in each is different. Mathematically this is accomplished by substituting the form of a Gaussian beam (Eq. A.5) into the coupled wave equation (Eq. 3.10). Detailed formulas introducing the normalised parameters used are given in App. A.2.

The expression for the second-harmonic power is calculated from the intensity of the wave and is given as

$$P_{2\omega} = \frac{16\pi^2 d_{\text{eff}}^2}{c\epsilon_0 \lambda_\omega^3 n_\omega n_{2\omega}} L_\text{c}\ e^{-\alpha' L_\text{c}} P_\omega^2 h(\sigma, \beta, \kappa, \xi, \mu) := \mathcal{K} P_\omega^2. \tag{3.19}$$

P_ω denotes the incident power, d_{eff} the effective susceptibility, n_ω and $n_{2\omega}$ are the refractive indices for the pump and the second-harmonic wave respectively, c is the velocity of light, λ_ω denotes the wavelength of the pump, L_c denotes the crystal length, $\alpha' = \alpha_\omega + \alpha_{2\omega}/2$ is a loss factor for both wavelengths and $h(\sigma, \beta, \kappa, \xi, \mu)$ is the Boyd-Kleinman factor, which represents a measure for the nonlinear interaction that generates second-harmonic waves. The dependence of the power generated by the nonlinear interaction on the Boyd-Kleinman factor $h(\sigma, \beta, \kappa, \xi, \mu)$ can be used for an optimisation depending on the waist of the Gaussian beam in the crystal.

The various terms of the Boyd-Kleinman factor are defined as

$$\begin{aligned}
\sigma &= \frac{\Delta k b}{2} && \text{phase mismatch} \\
\beta &= \frac{B}{\sqrt{\xi}} && \text{birefringence parameter} \\
\kappa &= \frac{\alpha b}{2} && \text{absorption factor} \\
\xi &= \frac{L_\text{c}}{b} && \text{focal strength} \\
\mu &= \frac{L_\text{c} - 2f}{L_\text{c}} && \text{focal position}
\end{aligned} \tag{3.20}$$

In these equations, b is the confocal parameter of the Gaussian beam (Eq. A.7), B is the walk-off parameter, α denotes the absorption in the material, Δk is the phase mismatch, and f is the focal position. For further analysis it will be assumed that absorption is negligible ($\kappa = 0$) and that the beam waist is at the optimal position, namely the centre of the crystal ($\mu = 0$). The Boyd-Kleinman factor can then be simplified to $h(\sigma, B, \xi)$. In the experiment described here, the crystal is temperature tuned ($B = 0$). However, for generality of discussion, B is included here. The only other free variable through which h might be optimised is the confocal parameter, b. The variation of h with B and ξ (and therefore b) for fixed σ is shown in Fig. 3.4.

The optimum output power for second-harmonic generation using phasematching techniques is reached for the parameters

$$B = 0 \qquad \xi(B = 0) = 2.84 \qquad h(B = 0) = 1.068 \tag{3.21}$$

A shift in the maximum of the function can be observed, when walk-off starts to play a role, i.e. $B \neq 0$. In this case, the optimum value of ξ decreases which is equivalent to the condition of weaker focusing.

For the temperature tuned (non-critical) QPM used in the experiment, $B = 0$. For a crystal length of $L_\text{c} = 10\,\text{mm}$ the optimal value of ξ requires a waist in the medium of $w_0 \approx 20\,\mu\text{m}$.

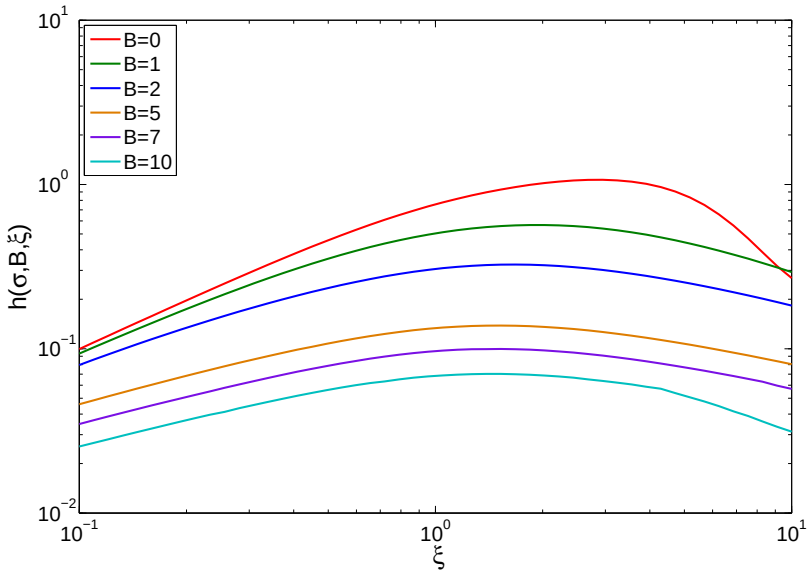

Figure 3.4.: The Boyd-Kleinman factor $h(\sigma, B, \xi)$ is plotted for varying parameters. The phase mismatch has been fixed at $\sigma = 0.57$ for this plot while the birefringence parameter B is altered. For increasing values of B, the maximum of $h(\sigma, B\xi^{-1/2}, \xi)$ shifts to lower values of ξ. The parameters for the maximum of the Boyd Kleinman factor are as given in Eq. 3.21.

3.2.1. Summary

The frequency-doubled system installed as a part of this thesis uses a ppKTP crystal to generate 422 nm second-harmonic light from 844 nm fundamental laser light. The process is assumed to happen in the weak conversion regime where the fundamental light intensity is not significantly decreased by back action of the generated second-harmonic light. Calculations showed a focus of 20 μm in the crystal centre to generate an optimum Boyd-Kleinman factor. The method used to introduce phasematching is quasi-phasematching. Tuning bandwidths for the crystal at hand are $\Delta T_{\mathrm{FWHM}} = 1.4\,^{\circ}\mathrm{C}$ and $\Delta\theta_{\mathrm{FWHM}} = 2.2\,^{\circ}$.

4. Output Enhancement with an Optical Cavity

Due to the typically low conversion efficiency of nonlinear crystals (normally below $0.05\,\mathrm{W}^{-1}$), satisfying second-harmonic output powers in the range of $100\,\mu\mathrm{W}$ to several mW were only achieved in the mid 1990s using high-power lasers with powers of at least several W. The problems arising from this, like the considerable electrical power required, thermal management and high costs could be overcome with optical cavities which 'recycle' the input light to increase the power of the fundamental wave, allowing appreciable second-harmonic powers for more modest fundamental powers.
For the experiment described here, a travelling-wave cavity in **bow-tie configuration** is used. Unlike standing-wave resonators, the travelling-wave ring resonator has an assigned wave direction, using the wave efficiently. Also the development of local high field intensities (at antinodes of the standing wave) is suppressed which preserves the crystal from damage.
The setup consists of two plane mirrors (the long arm, distance L) and two curved mirrors (the short arm, distance l) as can be seen in Fig. 4.1. The crystal is placed in the short arm of the cavity, where the waist of the Gaussian beam can be optimised to match the conditions for conversion.

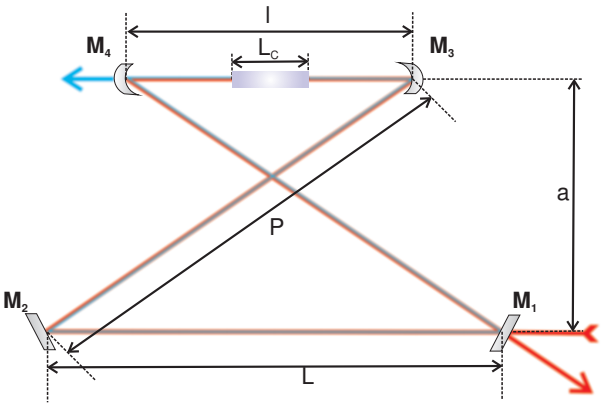

Figure 4.1.: The bow-tie resonator geometry as used in the experiment. The plane mirrors are separated by a distance L, the distance between a curved mirror and a plane mirror is denoted with $P = \frac{1}{2}\sqrt{4a^2 + (L+l)^2}$, the spacing of the curved mirrors is called l and the crystal length is L_c.

In Sec. 4.1, the building principles for a stable resonator will be given and extended to the realistic case using Gaussian beams with specific reference to the setup used in the experiment. Furthermore, Sec. 4.2 will provide insight into the effects of the cavity enhancement on the second-harmonic output power.

4.1. Creating a stable resonator - The ABCD matrices

This section will give a short introduction into the processes required to build a stable resonator, respecting the constraints at hand.

In order to describe the propagation of light through an arbitrary optical system ABCD matrices are used. The concept has been established in the early 20$^{\text{th}}$ century and became popular with the development of ever more demanding optics. Detailed considerations on the ABCD matrix technique can be found in optics textbooks as [65–67, 75] as well as in [76, 77].

The paraxial approximation describes rays as nearly parallel to a defining axis. They can therefore be described in terms of being at a distance r from the axis, and forming an angle Θ with it.

$$\begin{pmatrix} A & B \\ C & D \end{pmatrix} \cdot \begin{pmatrix} r \\ \Theta \end{pmatrix} \tag{4.1}$$

The passage through any optical system consisting of cascaded optical elements is then calculated by a multiplication of different matrices representing the optics and the vector of the ray as in Eq. 4.1. In Tab. 4.1 the most important matrix representations are summarised.

The matrix equations arising from the ABCD matrix description of the optical resonator system can be analysed most efficiently by calculating the eigenvalues $(\lambda_\mathrm{a}, \lambda_\mathrm{b})$ and eigenvectors $(\mathbf{r})$ of the matrix. To simplify the calculation of the eigenvalues, the value m is defined as half the trace of the matrix [67]:

$$m = \frac{A + D}{2}. \tag{4.2}$$

Hence, the eigenvalues can be calculated using the equation $\lambda_\mathrm{a}, \lambda_\mathrm{b} = m \pm \sqrt{m^2 - 1}$. The distinction between stable and unstable resonators can then be based on the analysis of the m value. The condition for building a stable and real resonator is given as

$$-1 \leq m \leq 1. \tag{4.3}$$

This constraint leads to complex eigenvalues with a value equal to unity. This leads to a description of rays traversing the system using a stable periodic function. Thus, they are oscillating along the axis between the components comprising the resonator.

4.1.1. ABCD matrix and Gaussian beams

For the consideration of lasers as coherent light sources the concept of matrix optics has to be expanded to Gaussian beams. The electric field of such a beam and the most important parameters are described in App. A.2. They can be readily described using the parameters (w_0, z_0), which are the waist, w_0, and the Rayleigh range, z_0, or using the so-called q - factor

$$\frac{1}{q} = \frac{1}{z - iz_0} = \frac{1}{R(z)} - i\frac{\lambda}{\pi w_0^2}. \tag{4.4}$$

Operation		ABCD Matrix
Translation	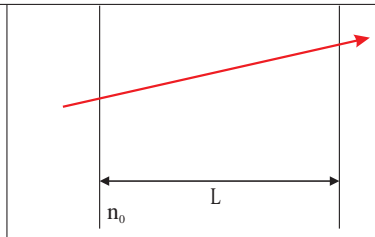	$\begin{pmatrix} 1 & \frac{L}{n_0} \\ 0 & 1 \end{pmatrix}$
Refraction (planar surface)	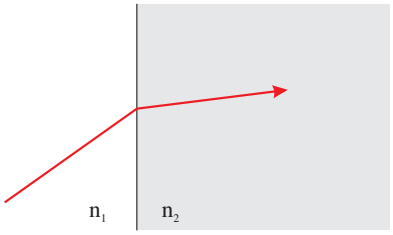	$\begin{pmatrix} 1 & 0 \\ 0 & \frac{n_1}{n_2} \end{pmatrix}$
Curved mirror, radius R	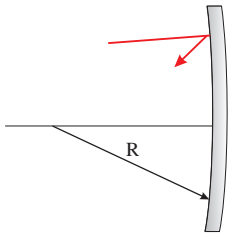	$\begin{pmatrix} 1 & 0 \\ \frac{-2}{R} & 1 \end{pmatrix}$
Thin lens, focal length f	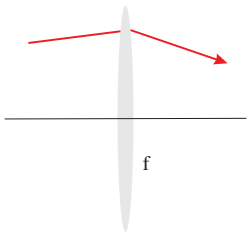	$\begin{pmatrix} 1 & 0 \\ -\frac{1}{f} & 1 \end{pmatrix}$

Table 4.1.: The ABCD matrices most important for the system under consideration here. This table is based on tables found in [65, 67, 77]

This latter expression comprises the parameters of a Gaussian beam defined along the z direction with the Rayleigh range $z_0 = \frac{\pi w_0^2}{\lambda}$, the beam waist w_0, the wavelength λ, and the wavefront's radius of curvature $R(z) = z\left(1 + \left(\frac{\pi n w_0^2}{\lambda z}\right)^2\right)$. It offers the possibility to link these variables with the components of the optical setup via the ABCD matrices. Gaussian beams propagating through an optical system are represented by

$$q_2 = \frac{Aq_1 + B}{Cq_1 + D} \tag{4.5}$$

with q_1 describing the beam before traversing the system and q_2 describing it afterwards. Considering a resonator it is important that $q_2 = q_1$. This means that the beam maps into itself after one round trip, and the field is therefore self-consistent. Using this, Eq. 4.5 can be solved giving solutions that can be related to Eq. 4.4.

$$\frac{1}{q_{1,2}} = \frac{D - A}{2B} \mp \frac{\sqrt{m^2 - 1}}{B} = \frac{1}{R(z)} - i\frac{\lambda}{\pi w_0^2} \tag{4.6}$$

In this way a connection is established between the physical properties of the optical system such as the radius of curvature, distances etc. and the waist within the cavity

$$w_0 = \sqrt{\frac{\lambda|B|}{\pi\sqrt{1-m^2}}}. \tag{4.7}$$

Hence, with Eq. 4.7 it is possible to calculate the waist at any point of the optical system. The position is always determined by the ABCD matrices involved in the calculation as will be shown in the next subsection.

4.1.2. ABCD matrices for a bow-tie cavity with a nonlinear crystal

After summarising the theoretical tools in the previous section, the method will be applied here for the experimental system realised: a bow-tie cavity containing a nonlinear crystal in the short arm.
The theory for Gaussian beams according to Boyd and Kleinman (see chapter 3 and App. A.2) optimises the output power of the second harmonic using the function $h(\sigma, B, \xi)$ (Eq. A.13). Due to the optimisation of the Boyd Kleinman factor to maximise the second-harmonic power generated, an ideal value for w_0 situated in the centre of the crystal is determined. This number is typically of order $20\,\mu$m and builds the basis for the cavity design with the ABCD matrix formalism. Hence, the waist position in the crystal centre gives the starting point to specify the matrices (Tab. 4.2).

Component	ABCD Matrix	Component	ABCD Matrix
Translation through half the crystal	$M_1 = \begin{pmatrix} 1 & \frac{L_c}{2n} \\ 0 & 1 \end{pmatrix}$	Translation crystal end to mirror Four	$M_2 = \begin{pmatrix} 1 & \frac{l-L_c}{2} \\ 0 & 1 \end{pmatrix}$
Mirror Four	$M_3 = \begin{pmatrix} 1 & 0 \\ \frac{-2}{\mathcal{R}_4} & 1 \end{pmatrix}$	Translation to Mirror Three	$M_4 = \begin{pmatrix} 1 & X \\ 0 & 1 \end{pmatrix}$
Mirror Three	$M_5 = \begin{pmatrix} 1 & 0 \\ \frac{-2}{\mathcal{R}_3} & 1 \end{pmatrix}$	Translation to the crystal	$M_6 = \begin{pmatrix} 1 & \frac{l-L_c}{2} \\ 0 & 1 \end{pmatrix}$
Translation to the crystal centre	$M_7 = \begin{pmatrix} 1 & \frac{L_c}{2n} \\ 0 & 1 \end{pmatrix}$		

Table 4.2.: This table includes all ABCD matrices necessary to calculate a waist in the bow-tie resonator. The matrices describe the optical components step by step using ascending numbers and starting in the crystal centre. For simplicity the path between the curved mirrors has been summed yielding $X = 2P + L = \sqrt{4a^2 + (L+l)^2} + L$; n is the refractive index of the crystal. The definition used is the same as in [78, 79].

In the matrices from Tab. 4.2 the only parameters that are readily set are the length of the crystal, L_c, its refractive index, n, and the radii of curvature of mirror three and four, $\mathcal{R}_3$ and $\mathcal{R}_4$ respectively. The matrix for a round trip in the bow-tie cavity, starting and ending in the centre of the crystal, is thus dependent on the distances between the plane mirrors, L, and between the curved mirrors, l.

$$M_{\mathrm{TOT}}(L,l) = M_7 \cdot M_6 \cdot M_5 \cdot M_4 \cdot M_3 \cdot M_2 \cdot M_1 = \begin{pmatrix} M_{11} & M_{12} \\ M_{21} & M_{22} \end{pmatrix}$$

The matrix elements M_{11} and M_{22} replace A and D respectively in Eq. 4.2 for the m factor and Eq. 4.7 for the waist. The formulas can both be optimised by a variation of the length parameters L and l. In order to get a positive real part and a vanishing imaginary part for the waist in the short arm, its length l is confined within a certain range as can be seen in Fig. 4.2. The constraints imposed by the stability condition lead to additional limits for the long arm length as only a pair of (L, l) yielding a value for m, that provides a stable cavity, can be used to construct a stable bow-tie resonator. However, when varying the lengths as indicated, computations show that the limits for the short arm length l are far more stringent.

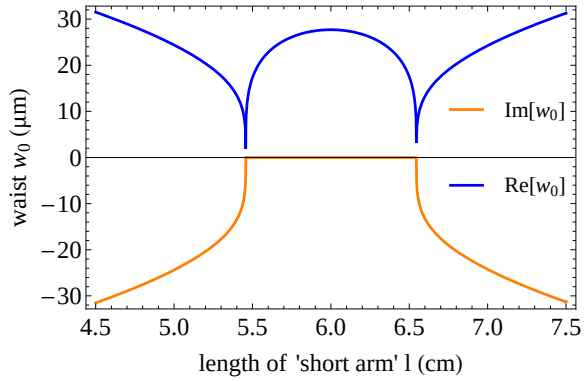

Figure 4.2.: The imaginary and real part of the waist in the short arm based on Eq. 4.7 are plotted here. The resonator is stable where the imaginary part equals zero. For this plot the parameters are $\mathcal{R}_3 = \mathcal{R}_4 = 5\,\text{cm}$, $n = 1,8412$, $L_c = 1\,\text{cm}$, $\lambda = 845 \times 10^{-7}\,\text{cm}$, $a = 4\,\text{cm}$, $L = 14.5\,\text{cm}$.

Having determined the length parameters for the cavity, it is an easy task to determine the waist in the long arm. A simple modification of the matrices from Tab. 4.2 is necessary to start from, and end at, the centre between the plane mirrors. Furthermore, the steps to calculate the waist in the long arm w_{la} are the same as for the waist in the short arm w_{sa}. Having calculated this parameter, it is possible to shape the incoming laser beam with lenses to get the spot size w_{la}. The lengths of the respective arms correspond to the calculations to produce a stable resonator.
The distance between long and short arm denoted a can be varied as well to have an additional condition for the setup of a stable resonator. However, this parameter a is, like the long arm length, L, not as critical as the length of the short arm, l, to implement a stable bow-tie cavity. However, it is recommendable to keep the value of a small, in order to minimise astigmatism.

4.2. Enhancement of the SHG power using a bow-tie resonator

It has already been pointed out in the very beginning of this chapter why resonant frequency doubling using a bow-tie cavity is promising. However, there exists a variety of configurations and possibilities as to how the basic principles can be implemented.
In this section the most important considerations of the analysis are pointed out and adapted for the case of interest: the generation of a second-harmonic wave supported by a surrounding cavity, resonant with the pump beam. More details can be found in [71, 79].

4.2.1. Parameters for resonant frequency doubling using a bow-tie cavity

SHG in an external resonator ('resonant SHG') can be described in terms of fields being reflected, transmitted and circulated by the cavity. To simplify the considerations a model is presented in Fig. 4.3 to clarify notation and the location of the field terms. In the following approach, the incident field will be denoted E_{in}, the field reflected from the input coupler is given as E_{ref}, and the field circulating within the cavity is E_{circ}.

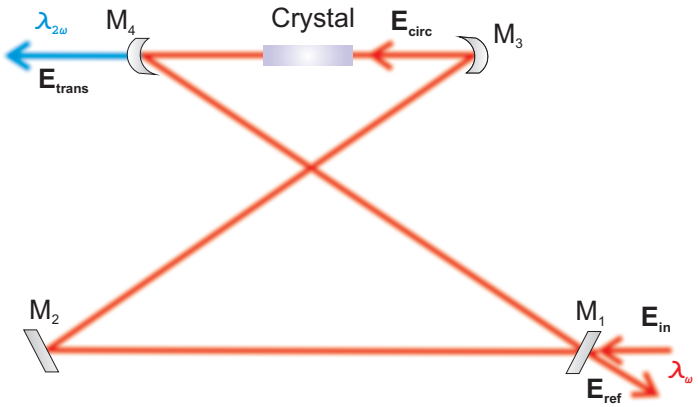

Figure 4.3.: The bow-tie resonator and the fields involved in the analysis. The plane mirrors are denoted M_1 and M_2 respectively; M_3 and M_4 are the curved mirrors. The fields are called E_{in} for the incident, E_{ref} for the reflected, E_{circ} for the field circulating in the cavity and E_{trans} for the transmitted, frequency doubled light. The notation in the theoretical approach is based on this picture, i.e. the coefficients are labeled numerically corresponding to mirrors of the same number and the fields are denoted as indicated here.

The reflection and transmission coefficients related to the cavity mirrors are assigned with the corresponding mirror number. Absorption at the mirrors is neglected. A distinction is made between amplitude coefficients for reflection r_i and transmission t_i with $i = 1, 2, 3, 4$ and power coefficients R_i and T_i, respectively. Due to energy conservation the power coefficients fulfil the equation $R_i + T_i = 1$ while for the amplitude coefficients the formula $t_i = \sqrt{1 - r_i^2}$ holds as $R_i = r_i^2$, $T_i = t_i^2$.

The nonlinear crystal gives rise to losses attributed to absorption and scattering, denoted T_{x}, as well as to a reduction of the field amplitude due to conversion. This latter loss will be described as $T_{\mathrm{SH}} = (1 - \mathcal{K}P_{\mathrm{circ}})$ with the factor $\eta_{\mathrm{SH}} = \frac{P_{2\omega}}{P_\omega} = \mathcal{K}P_\omega$ equivalent to the frequency doubling conversion efficiency. The variable $\mathcal{K} = \frac{2\omega^2 d_{\mathrm{eff}}^2 k_\omega}{\pi n^3 \epsilon_0 c^3} Lh(\sigma, B, \xi)$ can be derived from Eq. 3.19. As the fundamental power is the power circulating in the cavity a change in the index notation is made ($P_\omega \rightarrow P_{\mathrm{circ}}$) for consistency. Putting this together the crystal has a transmission coefficient of

$$T_{\mathrm{cryst}} = T_{\mathrm{x}} T_{\mathrm{SH}} = T_{\mathrm{x}}(1 - \mathcal{K}P_{\mathrm{circ}}). \tag{4.8}$$

For simplicity a resonator reflection amplitude coefficient

$$r_{\mathrm{m}} = r_2 r_3 r_4 t_{\mathrm{cryst}} \tag{4.9}$$

is introduced containing the mirrors' reflective coefficients and the crystal transmission. With these parameters, the fields circulating in, and reflected from, the cavity can be formulated.

Circulating field and related power

The field circulating in the cavity has to maintain a steady state. Its amplitude is diminished every round trip at the crystal due to reflection, absorption, scattering and the conversion in the crystal. To meet the steady state condition this loss has to be replenished by the incident field coupled into the resonator. This can be expressed with the equation

$$\frac{E_{\mathrm{circ}}}{E_{\mathrm{in}}} = \frac{it_1}{1 - r_1 r_{\mathrm{m}} e^{i\Phi}} \tag{4.10}$$

with a phase Φ accumulated during round trip. The circulating power pertaining to this is

$$\frac{P_{\mathrm{circ}}}{P_{\mathrm{in}}} = \frac{T_1}{(1 - \sqrt{R_1 R_{\mathrm{m}}})^2 + 4\sin^2(\Phi/2)}. \tag{4.11}$$

It is important to keep in mind that the resonant reflective coefficient r_{m} contains a part that is dependent on the power circulating in the cavity P_{circ}. A solution for the circulating power based on the input power can therefore be found by solving a cubic equation in P_{circ} which has been plotted for varying conditions in Fig. 4.5. Unless otherwise stated Eq. 4.11 is always considered at resonance ($\Phi = 2m\pi$).

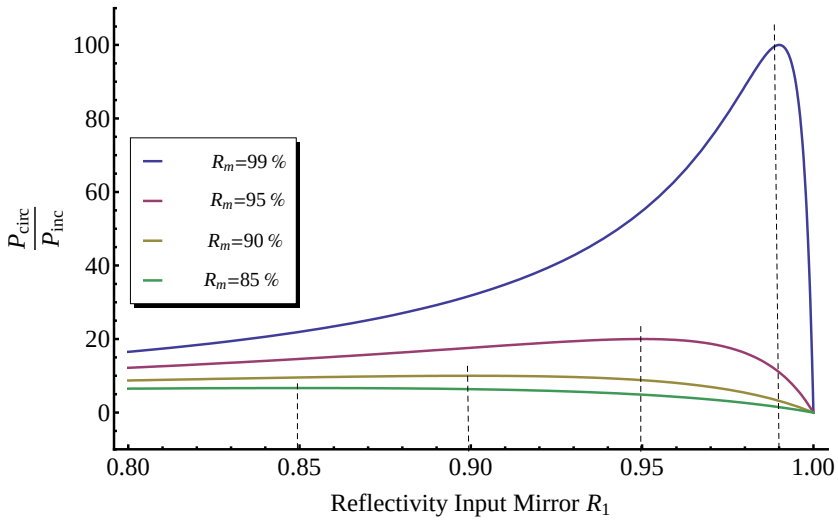

Figure 4.4.: The ratio of $P_{\mathrm{circ}}/P_{\mathrm{in}}$ based on Eq. 4.11 in case of resonance $\Phi = 2m\pi$; The curve is presented for different settings of the resonator reflectivity parameter R_{m}, neglecting losses due to conversion. From the figure can be determined, that the power circulating within the cavity can be much higher than the power incident on the cavity for $R_{\mathrm{m}} \to 1$. Therefore, a decrease in round trip losses is promising for effective power enhancement if losses due to conversion are negligible. Furthermore, the power ratio has its maximum value at the condition $R_1 = R_{\mathrm{m}}$, the so-called impedance matching condition.

Analysing Eq. 4.11 at resonance while *neglecting conversion losses* produces Fig. 4.4. From this plot, two important conclusions can be made: It is important to minimize round trip losses within the cavity to get a resonator reflectivity parameter close to unity ($R_{\mathrm{m}} \approx 1$). This generates a curve with high circulating power (close to 100 times the incident power for $R_{\mathrm{m}} = 0.99$). Furthermore, the maximum value is attained at the so-called **impedance matching** condition:

$$R_1 = R_{\mathrm{m}} = R_2 R_3 R_4 T_{\mathrm{cryst}}. \tag{4.12}$$

This is experimentally realised by the choice of an input coupling mirror with a transmission coefficient matching the losses in the rest of the cavity. If the conversion loss is taken into account, a dependence of the input coupling properties on the power of the pump laser is observed. This means that the optimal reflectivity of the input coupling mirror is dependent on the pump light power (compare with Fig. 4.7). For cavity enhanced SHG, the pump light power is the same as the circulating power.
Fig. 4.5 shows the behaviour of the circulating power vs. the pump light power for different input coupler reflectivities. While in Fig. 4.5a the lossless case is depicted, Fig. 4.5b takes losses due to conversion into account. As expected, the circulating power in the loss-free case exceeds the circulating power with conversion losses by far. In both figures the black curves denote the optimum condition of impedance matching. The parameters for the plots are taken from the experimental setup (see figure caption) and considering this, the choice of an input coupling mirror with a power reflectivity parameter of $R_1 = 95\,\%$ is appropriate. This is justified by effective pump light powers in the range of 20 mW to 60 mW where the impedance matching condition is best met by this value.

Reflected field and related power

The field reflected from the cavity can be described as a summation of the part of incident field which is directly back reflected and a term that represents the circulating field that leaks out of the resonator. Mathematically this is given as

$$\frac{E_{\mathrm{ref}}}{E_{\mathrm{in}}} = \frac{r_1 - r_{\mathrm{m}} e^{i\Phi}}{1 - r_1 r_{\mathrm{m}} e^{i\Phi}} \tag{4.13}$$

with the round trip phase Φ. The power in the reflected field is given by the equation

$$\frac{P_{\mathrm{ref}}}{P_{\mathrm{in}}} = \frac{(\sqrt{R_1} - \sqrt{R_{\mathrm{m}}})^2 + 4\sqrt{R_1 R_{\mathrm{m}} \sin^2(\Phi/2)}}{(1 - \sqrt{R_1 R_{\mathrm{m}}})^2 + 4\sqrt{R_1 R_{\mathrm{m}} \sin^2(\Phi/2)}}. \tag{4.14}$$

As already mentioned for the circulating power, the power dependence in the coefficient R_{m} may not be ignored. Taking a look at the reflected power when the condition for impedance matching (Eq. 4.12) is met, it is obvious that at resonance ($\Phi = 2m\pi$) all power incident on the cavity is coupled into it, and no reflection can be observed.

Finesse

Plotting the ratio of transmitted field to incident field against phase Φ, a figure with well defined maxima at $\Phi = 2m\pi$ is generated (see Fig. 4.6).

In frequency space the sharpness of these peaks can be appraised quantitatively using the finesse parameter. It is defined as the ratio of the free spectral range between consecutive resonance frequencies to the full width at half maximum of the curve: $\mathcal{F} = \Delta\nu_{\mathrm{FSR}}/\Delta\nu_{\mathrm{FWHM}}$. A derivation of this can be found in App. B. Here, only the basic results will be given for a bow-tie resonator with a nonlinear crystal inside.
The power coefficient R_{m} denotes again the resonator reflectivity including the crystal transmission (defined as in equation 4.9), R_1 is the reflectivity of the first mirror, $R_{\mathrm{T}} = \prod_{i=1}^{4} R_i$ is the product of all mirror reflectivities and $\mathcal{L}_{\mathrm{T}}$ are the total losses. The finesse

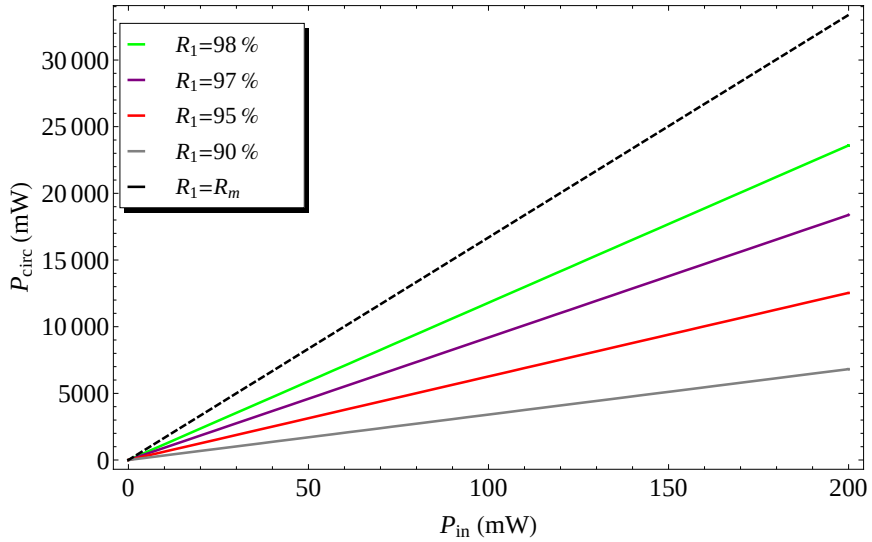

(a)

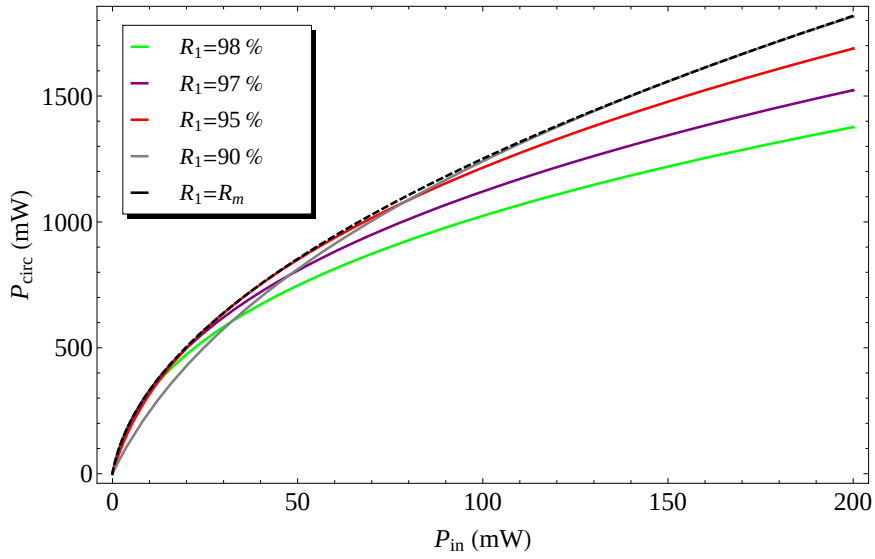

(b)

Figure 4.5.: (a) depicts the power circulating in the cavity in the absence of conversion losses due to the crystal. As expected, the power increases linearly with the incident power, getting steeper as the reflectivity of the input coupler gets higher. The maximum is reached at impedance matching. (b) shows the behaviour of the circulating power if losses occur. Because the circulating power is diminished at every round trip, it never grows as much as in the case without losses. The parameters for the plots are $\mathcal{K} = 0.028 \times 10^{-3}$, T_x =0.997, $R_2 = R_3 = R_4$ =0.998, taken from the real experimental setup (cf. chapter 5).

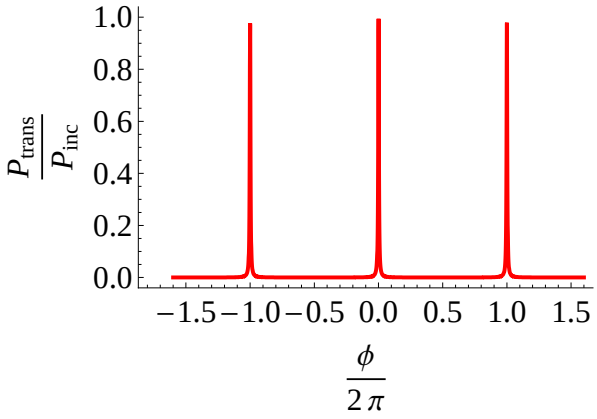

Figure 4.6.: The ratio of P_{trans}/P_{in} based on Eq. B.1 is plotted dependent on the phase Φ. The assumed value for the reflectivities are $R_i = 0.99$. The periodicity of the function arises from the resonance condition $\Phi = 2m\pi$.

for the cavity including SHG can then be written as

$$\mathcal{F}_{\text{SHG}} = \frac{\pi}{2\arcsin\left(\frac{1-\sqrt{R_1 R_{\text{m}}}}{2(R_1 R_{\text{m}})^{1/4}}\right)} \approx \frac{\pi(R_{\text{T}}(1-\mathcal{L}_{\text{T}}))^{1/4}}{\left(1-\sqrt{R_{\text{T}}(1-\mathcal{L}_{\text{T}})}\right)}. \tag{4.15}$$

In the formula above, the last term uses the relation $\arcsin\alpha \approx \alpha$ assuming sharply defined resonance. With the assumption $R_{\text{T}} \approx 1$ the equation can be simplified

$$\mathcal{F}_{\text{SHG}} \approx \frac{\pi}{\left(1-\sqrt{R_{\text{T}}(1-\mathcal{L}_{\text{T}})}\right)}. \tag{4.16}$$

The mirror reflectivities are well known and the finesse, $\mathcal{F}_{SHG}$, when generating a second-harmonic wave can be measured. The overall losses can be determined by solving this equation for $\mathcal{L}_{\text{T}}$.

4.2.2. Resonator enhancement of the second harmonic

All formulas of the previous section take into account how the fundamental power is influenced by the cavity, but no statement about the effect on the generated light has been made so far. Therefore, an enhancement factor, $\mathcal{Q}$, will be introduced here to enable quantitative statements on the overall conversion efficiency [79, 80].

The overall enhancement can be described as the ratio of the generated field to the field that pumps the conversion. In resonantly enhanced SHG the pump field is represented by the circulating field:

$$P_{2\omega} = \mathcal{K} P_{\text{circ}}^2 \tag{4.17}$$

Eq. 4.17 corresponds to Eq. 3.19 abbreviating the prefactor as $\mathcal{K} = \frac{16\pi^2 d_{eff}^2}{c\epsilon_0 \lambda_\omega^3 n_\omega n_{2\omega}} lh$ and effectively denoting the circulating power as fundamental power. The overall conversion efficiency is written as

$$\mathcal{Q} = \frac{P_{2\omega}}{P_{\text{in}}}. \tag{4.18}$$

Substituting the expression for $P_{2\omega}$ and simplifying as much as possible with respect to changing P_{circ} against P_{in} the factor can be given as

$$\sqrt{\mathcal{Q}} = \sqrt{\mathcal{K} P_{\mathrm{in}}} \frac{T_1}{\left(1 - \sqrt{1 - T_1}\sqrt{(1-\mathcal{L})(1 - \sqrt{\mathcal{K}\mathcal{Q}P_{\mathrm{in}}})}\right)^2} \tag{4.19}$$

with the overall losses $\mathcal{L}$ in the cavity (neglecting conversion losses) due to absorption and scattering from the crystal and the reflection coefficients of the mirrors given by $(1 - \mathcal{L}) = R_2 R_3 R_4 T_x$. For the impedance matched case further simplifications can be made using the fact that the transmission coefficient of the input coupling mirror has to match the passive losses in the resonator as well as the conversion losses (compare with Eq. B.12). However, the losses are dependent on the incident power and therefore the generated second-harmonic power can be maximised by choosing the appropriate reflectivity input mirror in accordance with this, as can be seen in Fig. 4.7. The figure illustrates a shift to lower values of the reflectivity coefficient needed in order to achieve maximum generated second-harmonic power for increasing incident power. Hence, for an incident fundamental power of $P_{\mathrm{in}} = 100\,\mathrm{mW}$ the impedance matched reflective coefficient is $R_1 = 92\,\%$ while for fundamental powers as low as $P_{\mathrm{in}} = 30\,\mathrm{mW}$ the reflective coefficient has to equal $R_1 = 95\,\%$ to fulfil the impedance matching condition.

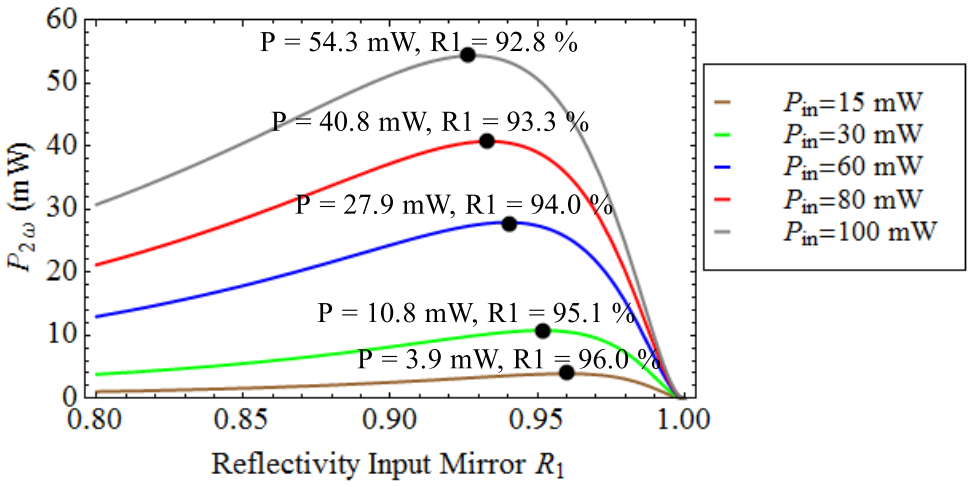

Figure 4.7.: The generated second-harmonic power as a function of the input coupling mirror's reflectivity R_1 for different incident powers. The computation was done using Eq. 4.19 and Eq. 4.11 with the single pass conversion efficiency $\mathcal{K} = 0.028 \times 10^{-3}$ mW and losses attributed to an imperfect reflectivity of the mirrors and the crystal transmission of $\mathcal{L} = 2\,\%$. It is obvious, that the optimum for the reflectivity of the input coupling mirror is shifted towards lower values with increasing pump light power.

The importance of the right reflectivity value for the input coupling mirror can be depicted also if the overall conversion efficiency given in Eq. 4.17 is plotted as a function of the incident power as in Fig. 4.8. The circulating power can be calculated from Eq. 4.11 at resonance and solving the resultant cubic equation.

As can be seen from Fig. 4.8, the experimental setup at hand yields an overall conversion efficiency that approaches 50 % in the optimum case. The region of interest concerning

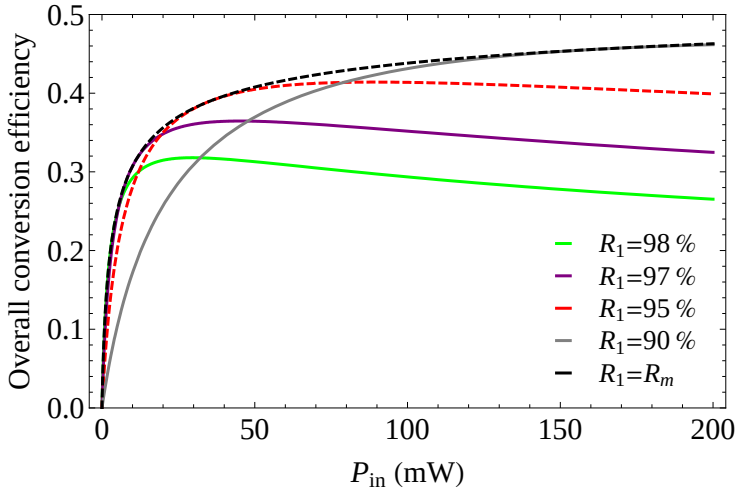

Figure 4.8.: The overall conversion efficiency as a function of the incident fundamental power for different values of the input coupling reflectivity R_1. The black curve denotes the impedance matched case. The plot was generated using Eq. 4.11 and Eq. 4.17 with the single pass conversion efficiency $\mathcal{K} = 0.028 \times 10^{-3}$, T_x =0.997 and $R_2 = R_3 = R_4$ =0.998, taken from the real experimental setup. The optimum curve ($R_1 = R_m$) approaches 50 % overall conversion efficiency. The other curves lie below or meet the optimum in certain regions of incident fundamental power.

incident fundamental power lies between 20 mW and 60 mW, where the optimum curve varies approximately 4 % (between 36 % and 40 %). As already stated when analysing the circulating power including losses, the optimum reflectivity for the input coupling mirror is around 95 %.
In order to get a quantitative statement for the second-harmonic power that can be generated, further analysis is carried out. Including the fact that at impedance matching the incident power is increased by the inverse transmission coefficient $P_{circ} = P_{in}(T_1^{opt})^{-1}$ the conversion efficiency is

$$\mathcal{Q} = \frac{\mathcal{K} P_{in}}{(T_1^{opt})^2}. \tag{4.20}$$

Using the expression $T_1^{opt} = \frac{\mathcal{L}}{2} + \sqrt{\left(\frac{\mathcal{L}^2}{4} + \mathcal{K} P_{in}\right)}$ for the optimum transmission coefficient as derived in App. B, the generated power can be represented by

$$P_{2\omega} = \frac{P_{in}}{\left(X_{FOM} + \sqrt{1 + X_{FOM}^2}\right)^2} \tag{4.21}$$

with $X_{FOM}^2 = \frac{\mathcal{L}^2}{4\mathcal{K} P_{in}}$; FOM denotes the figure of merit.

Comparing single-pass conversion and SHG using a surrounding cavity for impedance-matched conditions as in Fig. 4.9 makes the advantages of the latter obvious. At a pump power of 30 mW, the single-pass conversion generates only about 20 μW while for perfect conditions the cavity enhanced setup would give an output of 13 mW. This yields a discrepancy of 3 % comparing Figs. 4.8 (optimum case at 40 %) and 4.9 (optimum case at 43 %) which is not yet fully understood. The measured output at that pump power (see chapter 6) which was in the best case around 3 mW can be calculated assuming losses of $\mathcal{L}$ = 8 % originating from the imperfectly reflecting mirrors and the crystal

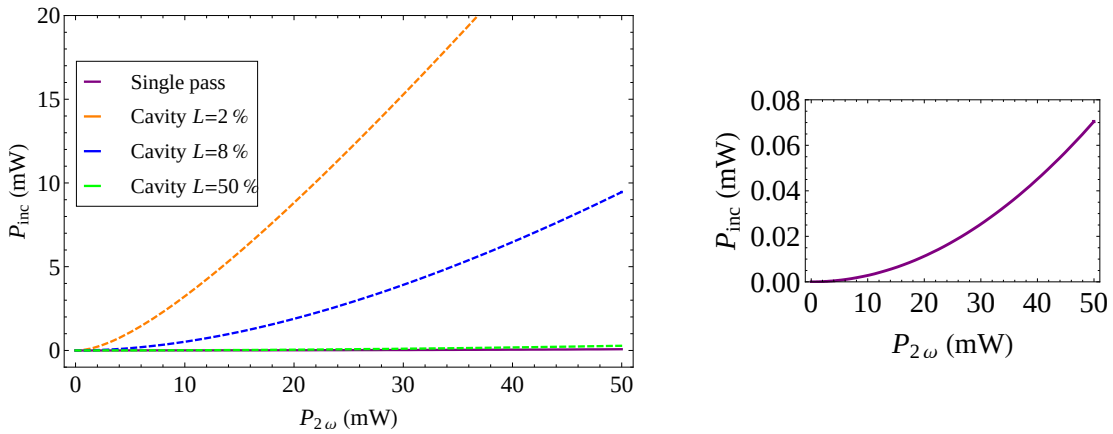

Figure 4.9.: The converted power as a function of the pump power for single pass (based on Eq. 4.17 and Eq. 3.19) and cavity enhancement with 2 %, 8 % and 50 % losses respectively (based on Eq. 4.21). The right figure shows a magnification of the single-pass curve, depicting the expected quadratic behaviour. The parameters used are $d_{\text{eff}} = 9.8\,\text{pm/V}$, $\lambda = 845\,\text{nm}$, $n_\omega = 1.8412$, $n_{2\omega} = 1.947814$, $L_c = 1\,\text{cm}$ and $h_{\max} = 1.068$ for the ideal case. This leads to a conversion efficiency of $\mathcal{K} \approx 2.8\,\%$. The overall losses in the cavity, related to imperfect reflection of the mirrors and the crystal transmission, are estimated to be $\mathcal{L} = 2\,\%$. However, a value of $\mathcal{L} = 8\,\%$ matches the output found in chapter 6 more closely. And with losses in the range of $\mathcal{L} = 50\,\%$ the cavity enhancement would yield the same output as the single pass conversion.

transmission. Only if the losses in the resonator increase strongly, approaching a value of $\mathcal{L} = 50\,\%$, are the single pass power and the enhanced power similar.

5. Photoionisation Setup

As described in chapter 2, photoionisation represents an advantageous method of loading ion traps. Thus, it is widely used to generate ions from different atomic species. However, the application to ^{40}Ca is restricted by the shortage of laser diodes at some required wavelengths, which can be overcome using a frequency doubled system.

This thesis is based on the assembly of a laser system to photoionise ^{40}Ca using 422 nm light from a frequency doubled 844 nm laser and a 377 nm laser diode. This chapter provides a description of the experimental setup for photoionisation, giving a detailed survey of the characteristics and most important parameters (see Fig. 5.1 for the complete assembly). Sec. 5.1 introduces the characteristics of the light sources (844 nm and 377 nm diode lasers as well as the 422 nm frequency doubled beam), including diagrams of the setup. Sec. 5.2 applies the theoretical approach regarding cavities for frequency doubling developed in chapter 4 to the system at hand and Sec. 5.3 describes the locking scheme used. As the crystal temperature is a critical parameter in the frequency doubling for 422 nm, Sec. 5.4 gives a description of the experimental realisation of the temperature control. The description of the overlapping of the 422 nm laser and the 377 nm laser and their coupling efficiencies into a fiber to deliver light to the trap given in Sec. 5.5 concludes the chapter.

5.1. Characterisation of the lasers

5.1.1. 844 nm laser

The source for the 844 nm is a ready-mounted laser head[1], controllable with standard diode-laser supply electronics[2]. It contains a diode with a central wavelength of 844 nm with grating stabilisation in Littrow configuration. Furthermore, the mount includes temperature stabilisation to guarantee good lasing conditions. Coarse adjustment of the wavelength (tuning range around 17 nm) can be performed using a micrometre screw at the side of the head to change the grating angle. Fine adjustments can be accomplished using the piezo actuator included in the setup to displace the grating (change the external-cavity length). Built into the laser head is an optical isolator with an attenuation of 60 dB. The specifications at an operating temperature of 20 °C are summarised in Tab. 5.1.

The performance of the laser system was reassessed measuring the optical output power at 20 °C. The results obtained by the measurement are in good agreement with the specifications. A plot of the output power as a function of the drive current is shown in

[1] TOPTICA; DL pro laser series; LD-0850-0300-4

[2] TOPTICA; Sys DC 110; standard equipment to operate the laser head consisting of DC 110, DCC 110, DTC110 and SC110

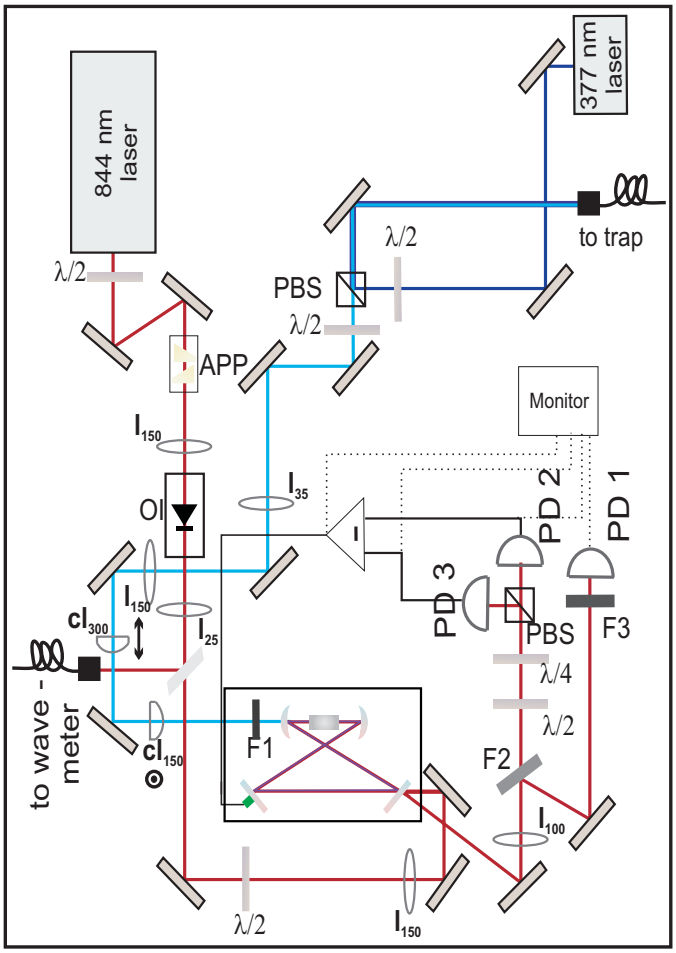

Figure 5.1.: Photoionisation laser setup, including both, the 422 nm frequency doubled system and the 377 nm laser diode as well as the components to overlap and couple both into the fibre leading to the trap. Three different photodiodes (PD1 - PD3) are used to generate an error signal (see Sec. 5.3) and to monitor the reflected signal. The filters used are denoted F, being a narrow band-pass filter centered at 417 nm to remove leaking 844 nm light after the cavity (F1 - FF01/417), an attenuator plate with 10 % transmission to prevent the photodiodes (PD1, PD2) from saturation (F2) and an neutral density (ND) filter with 3.2 % transmission (F3). The anamorphic prism pair is abbreviated APP, OI stands for optical isolator and PBS denotes a polarising beam splitter. The lenses are marked with l_f if they are spherical and cl_f if they are cylindrical lenses. The focal length is given as a subscript in mm.

Parameter	Symbol	Value Data sheet	Value Measured	Unit
Threshold Current	I_{th}	69.0	68.0	mA
Operating Current	I_{OP}	255.0	255.0	mA
Maximum Current	I_{max}	269.0		mA
Maximum Voltage	V_{max}	2.15		V
Slope Efficiency	η_{s}	0.76	0.72	W/A
Optical output power	P_{O}	113.0	103.0	mW

Table 5.1.: The table summarises the characteristic parameters for the 844 nm laser diode at an operation temperature of 20 °C according to the data sheet and compares them to the measured values. The laser is typically operated at a lower current (100 mA) with correspondingly lower output power 23.3 mW.

Fig. 5.2. The output beam is predominantly s-polarised (> 95 %) and has an elliptical shape with an aspect ratio of vertical axis : horizontal axis = 1 : 3.

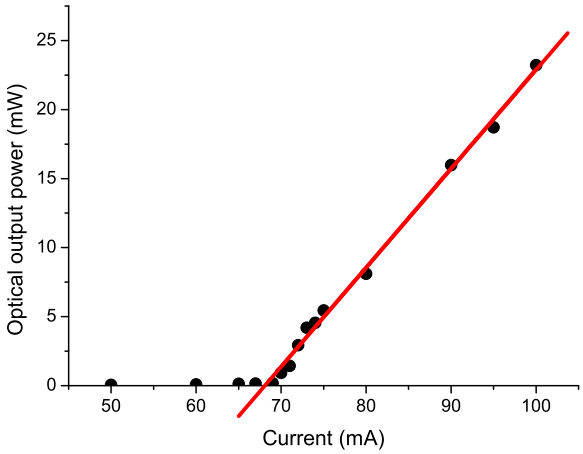

Figure 5.2.: Characterisation of the 844 nm laser diode at 20 °C. A linear fit to the measured data gives a linear equation $P = 0.72(\mathrm{W/A})I(\mathrm{A}) - 48.9(\mathrm{W})$, determining the slope efficiency as $\eta_s = 0.72\,\mathrm{W/A}$ and the threshold current as $I_{\mathrm{th}} = 68.0\,\mathrm{mA}$.

Optical path

To purify the polarisation and to correct for the ellipticity, a $\lambda/2$ waveplate and an anamorphic prism pair[3] (APP, see Fig. 5.3) are introduced into the setup. The $\lambda/2$ waveplate assures the adjustment of the polarisation in a way to match the Brewster angle of the APP and hence increase the optical power transmitted. Thus, a circular beam shape with tunable polarisation is generated. A system of three lenses is set up in order to achieve proper mode matching to the cavity. The first and second lens form a 6:1 lens telescope ($f = 150\,\mathrm{mm}$: $f = 25\,\mathrm{mm}$, both AR coated for 700 nm - 870 nm) to reduce the beam size. The second and the third lens ($f = 150\,\mathrm{mm}$ AR coated at 700 nm - 870 nm) are each mounted on single-axis micro-positioning stages. The lens positions can then be finally adjusted to create a 200 μm beam waist at the centre of the cavity's long arm and ensure good mode matching. An additional optical isolator[4] (OI), with an attenuation of 35 dB, was introduced to the system to reduce back-reflections from the resonator to the laser. This was done at a later time, hence its location within the lens telescope system due to limited space in the setup, is not the optimum choice as the traversing beam is not collimated. However, input coupling into the cavity could not be increased above 25 % without the optical isolator, while 60 % input coupling was achieved if the isolator was included.
Wavelength monitoring with a wavelength meter[5] is possible as approximately 4 % of the laser power is coupled into a fibre using a beam pick off. The coupling into the cavity, which is constructed according to the parameters as described in Sec. 5.2, is achieved with two mirrors. The light back-reflected from the first cavity mirror permits

[3] THORLABS; PS879 3x magnification
[4] ISOWAVE; I-80-T5-M (tunable)
[5] TOPTICA; Wavelength Meter Ångstrom WS/7MC8

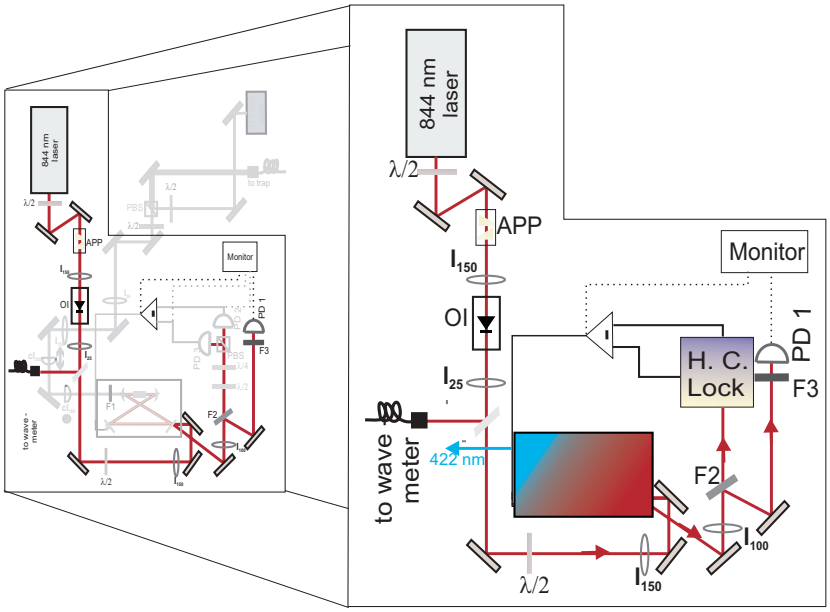

Figure 5.3.: The beam path described as in the text. APP: anamorphic prism pair; OI: optical isolator; l_f lens with focal length in mm;

the installation of a Hänsch - Couillaud locking scheme [81] which facilitates the locking of the cavity to the laser. For this purpose, an additional $\lambda/2$ waveplate has to be introduced in the optical path before the input coupling mirror of the cavity. More details on the lock can be found in Sec. 5.3.
Losses, mainly due to absorption and scattering effects, are at 34 % for the total optical path from the laser to the cavity.

5.1.2. 422 nm laser

The first transition in the photoionisation process demands 422 nm light. This is generated with frequency doubling. The conversion from 844 nm to 422 nm light is accomplished using a nonlinear ppKTP crystal[6] in a bow-tie cavity to enhance the second-harmonic generation. Details on the crystal are summarised in Tab. 5.2 and the cavity is described in Sec. 5.2.

The dependence of the 422 nm light power on the pump light power incident on the cavity is given by Eq. 4.21. To characterise the system after choosing the optimum temperature for the wavelength at hand (see Sec. 5.4) the pump power emerging from the 844 nm laser was changed, and the optical output power at 422 nm was measured. To avoid influences on the result due to mode hops or a reduction in input coupling efficiency, both parameters were checked regularly and discrepancies were corrected for. The characterisation is illustrated in Fig. 5.4, with a fit using Eq. 4.21. The mismatch in fit and actual measured data is partially attributed to possible temperature fluctuations. Additionally, the chosen input coupling mirror with a reflectivity of 95 % meets the impedance matching condition only in the range of 25.0 mW to 50.0 mW incident pump power. Thus, for power values not lying within this range, the conversion efficiency and the generated second-harmonic power is not at its optimum (see Fig. 4.8).

[6] RAICOL CRYSTALS LTD.; ppKTP

Parameter	Symbol	Value	Units
Dimensions	b × h × l	(1 × 2 × 10)	mm
Period length	Λ	3.9582	μm
Maximum Temperature	$T_{\max}$	200	°C
Average Heating Rate	R	5	°C/min
Temperature tuning bandwidth	ΔT_{FWHM}	1.4	°C
Angle tuning bandwidth	$\Delta\theta_{\mathrm{FWHM}}$	2.2	°
Crystal transmission (measured)		0.997	%
Refractive index at 844 nm	n_ω	1,84446241	
Refractive index at 422 nm	$n_{2\omega}$	1,962971228	

Table 5.2.: The table represents a summary of the important crystal properties.

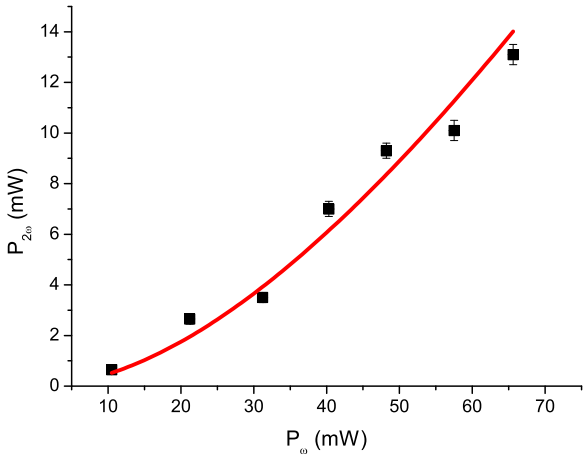

Figure 5.4.: Power generated at 422 nm after the cavity, $P_{2\omega}$, in dependence on the pump light power at 844 nm incident at the cavity, P_ω. The fit was generated using Eq. 4.21 with a single pass conversion efficiency $\mathcal{K} = 0.028 \times 10^{-3}\mathrm{W}^{-1}$ and losses of $\mathcal{L} = 8\,\%$.

The 422 nm light emerging from the cavity has to be shaped in order to achieve efficient fibre coupling. As the beam profile is elliptical with a strong divergence, a system of lenses is used to collimate and form the laser profile (see Fig. 5.5). A circular shape is generated with a 1:2 cylindrical lens telescope ($f = 150$ mm and $f = 300$ mm, both AR coated 350 nm - 700 nm). This is followed by a 1:4 telescope ($f = 150$ mm and $f = 35$ nm, both AR coated 370 nm - 450 nm) to collimate the beam before it is overlapped with the 377 nm laser as described in Sec. 5.5. The overall losses of the 422 nm laser power for the optical path from the cavity to immediately before the polarising beam splitter (PBS) for overlapping with the 377 nm laser light are 10 %.

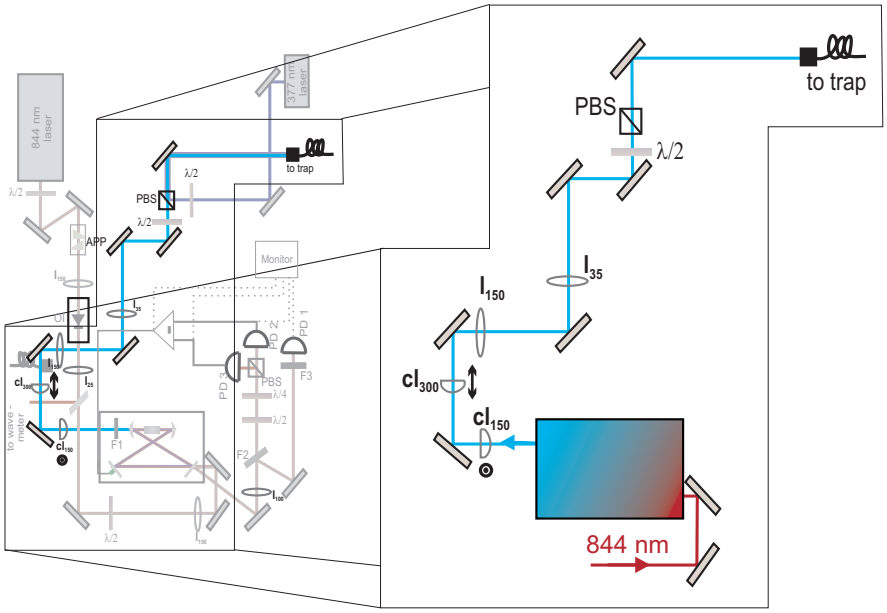

Figure 5.5.: Beam path for the 422 nm between the cavity and the fibre to the trap. l_f lens with focal length in mm; cl_f cylindrical lens with focal length in mm.

5.1.3. 377 nm laser

The setup of the 377 nm laser consists of a diode[7] with a central wavelength at 377 nm and a temperature stabilising laser mount[8]. The laser diode itself, as well as the temperature stabilised mount, are supplied and controlled with a laser diode combi controller[9]. The specifications at 25 °C, optical output power 20.0 mW according to the data sheet are summarised in Tab. 5.3.

Parameter	Symbol	Value Data sheet	Value Measured	Unit
Threshold Current	I_{th}	49.9	50.0	mA
Operating Current	I_{OP}	72.4	72.4	mA
Maximum Current	I_{max}	110		mA
Operating Voltage	V_{OP}	5.1	5.0	V
Maximum Voltage	V_{max}	6.5		V
Slope Efficiency	η_{s}	0.89	0.41	W/A
Optical output power	P_{O}	20.0	10.0	mW
Beam Divergence Angle (parallel)	θ_{par}	9.6	10.2	°
Beam Divergence Angle (perpendicular)	θ_{per}	23.9	22.2	°

Table 5.3.: The table summarises the characteristic parameters for the 377 nm laser diode at an operation temperature of 25 °C according to the data sheet and compares them to the measured values.

The temperature stabilisation can be configured using the PID (proportional-integral-

[7] TOPTICA; LD-0375-0020-1
[8] THORLABS; TCLDM9
[9] THORLABS; ITC510

derivative) actuators to achieve a good temperature stability. As the thermistor is a thermoelectric cooler (TEC) element, the temperature values are given in kΩ, the set point for the running system is chosen as 10 kΩ which corresponds to 25 °C according to the manual for the temperature stabilised laser mount [82]. In order to prevent the diode from damage, the maximum current is set to 99.5 mA, well below the maximum of 110.0 mA given in the data sheets (see Tab. 5.3). A measurement of the output power in dependence on the supply current, as well as a characterisation of the beam shape, were carried out.

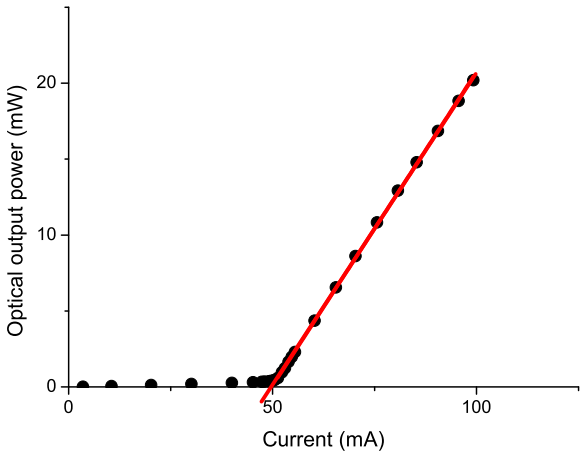

Figure 5.6.: Characterisation of the 377 nm laser diode at 25 °C. A linear fit to the measured data gives a linear equation $P = 0.41(\mathrm{W/A})I(\mathrm{A}) - 20.6(\mathrm{W})$, determining the slope efficiency as $\eta_s = 0.41\,\mathrm{W/A}$ and the threshold current as $I_{th} = 50.0\,\mathrm{mA}$.

The measured threshold current of 50.0 mA is in good agreement with the specification ($I_{th} = 49.9\,\mathrm{mA}$) while the measured slope efficiency of 0.41 W/A differs considerably from the data sheet ($\eta_s = 0.89\,\mathrm{W/A}$) (compare with Fig. 5.6). This may be due to dirt on the window of the diode which could not be removed by simple cleaning techniques. Thus, the diode starts to lase at the value anticipated but the optical output power is always below the expected values.

Optical path

An adjustment of the beam shape is done using a ready-mounted aspheric lens[10] with the help of a spanner wrench[11]. Appropriate collimation can be achieved over approximately 1.5 m, which is sufficient to overlap the 377 nm laser beam with the 422 nm laser beam and couple them into a fibre (see Sec. 5.5). However, the beam displays strange interference patterns as it diverges in the far field. This could not be overcome by remounting and cleaning the diode and the lens, but the effects on the resulting coupling are negligible. Therefore, the beam path as illustrated in Fig. 5.7 only consists of mirrors, no additional lens telescope is used to shape the beam profile. However, an additional telescope might improve the input coupling efficiency as is described further in Sec. 5.5.

[10] THORLABS; aspheric lens C610TM-A with a lens adapter S1TM09
[11] THORLABS; SPW909

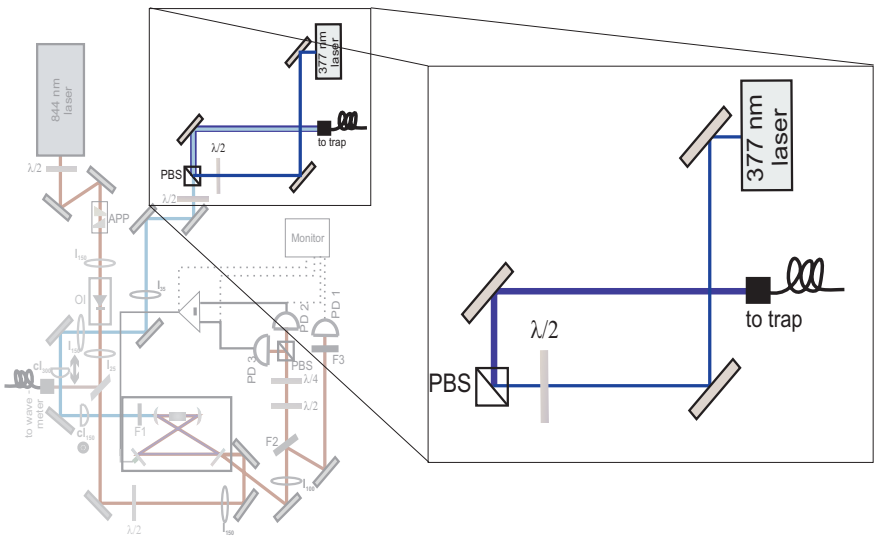

Figure 5.7.: Path of the 377 nm laser between the laser diode in its temperature stabilised mount and the fibre, leading to the trap.

5.2. Cavity

The construction of a cavity around a nonlinear crystal results in enhancement of the generated second-harmonic power. Since the basic principles for setting up a stable resonator for a frequency-doubling system were already explained in chapter 4, only the parameters used in the system are given here. The parameters of the setup are influenced by the components used (for example by the crystal length, and the radius of curvature of the mirrors) as well as by the waist one wants to obtain. The mirrors built into the system are summarised in Tab. 5.4. Based on a desired waist in the 'short arm' of $w_{\mathrm{sa}} = 23\,\mu$m, and with a given radius of curvature (ROC) for M_3 and M_4 of -50 mm, the remaining parameters are varied to achieve a stable cavity. The stable condition chosen for the setup at hand (see Fig. 5.8) is a 'short-arm length' of $l = 59$ mm, a 'long-arm length' of $L = 145$ mm and a spacing between both arms of $a = 43$ mm. This gives the desired value of a waist with $w_{\mathrm{la}} = 193\,\mu$m, situated in the centre of the 'long arm'. The lens system for the 844 nm laser already mentioned in Sec. 5.1 assures that the laser beam can be mode-matched. Computation shows the sensitive stability dependence on the 'short-arm length', l, while a variation of the 'long-arm length', L, or the parameter denoting the spacing between the long and the short arm, a, do not quickly give rise to instability.

	Configuration	ROC (mm)	R at 844 nm (%)	R at 422 nm (%)
M_1	plane	inf	95.0	-
M_2	plane	inf	99.8	< 15.0
M_3	concave	- 50	99.8	< 15.0
M_4	concave	- 50	99.8	< 15.0

Table 5.4.: The table gives an overview of the mirrors forming the cavity. All were purchased from LASEROPTIK. The value for the input coupling mirror was chosen according to a computation as in Fig. 4.7. ROC denotes the radius of curvature while R stands for reflectivity

A simple way to set up the resonator is to plot a plan (cf. Fig. 4.1) according to the

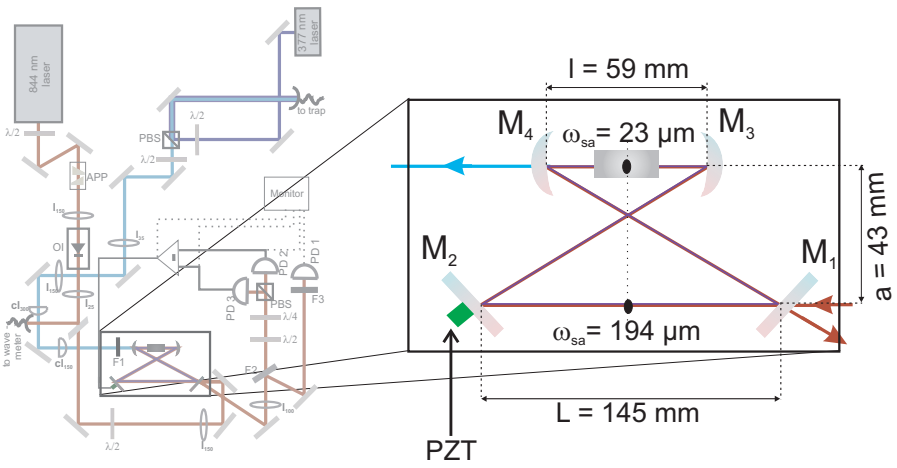

Figure 5.8.: Cavity constructed, including the vital parameters; The green 'extension' of M_2 is the piezo actuator, used to lock the cavity to the laser as described in Sec. 5.3.

simulations, that is used as a template for the setup. Once mirrors M_2 to M_4 have been put into place, the input coupling mirror M_1 is introduced. While scanning the piezo with a saw tooth voltage, rough optical overlapping can be accomplished using an IR viewer[12]. Afterwards, the signal is monitored with a photodiode. Initially, input coupling efficiencies did not exceed 25 % despite the 60 dB optical isolator already installed in the laser head. Only when an additional 35 dB isolator was built in the efficiency could be increased to its present value of 55 %. Following optimisation of input coupling the modes remaining (see Fig. 5.12) do not disturb the SHG or the locking process. The resonator is stabilised with the Hänsch - Couillaud method, using the laser as a reference.
The measured value for the finesse of the cavity including the crystal but without frequency conversion was 60. This value deviates from the theoretical value of 104, calculated using Eq. B.6, by a factor of 1.7. For the calculations, the cavity reflectivity parameter was assumed to be $R_m = 0.941$ including losses due to the passage through the crystal. The discrepancy is possibly attributable to imperfect reflecting mirrors and a clipping of the beam by the crystal mount.

5.3. Hänsch - Couillaud stabilisation

The possibility to control and stabilise laser frequencies is one of the prerequisites for the experimental work with atomic transitions and precision measurements. In the discussed experimental setup, the 34.7 MHz linewidth of the transition from $^1S_0$ to $^1P_1$ at 422 nm wavelength represents an important constraint on the laser linewidth while the transition from the $^1P_1$ state to the continuum at 377 nm wavelength does not need to be stabilised. The Hänsch - Couillaud stabilisation method is used to lock the cavity to the laser, as the cavity setup for resonant second-harmonic generation already includes a 'polarisation element' needed to implement this scheme [81] in the form of a birefringent nonlinear crystal.

The Hänsch - Couillaud scheme is based on the polarisation analysis of the beam re-

[12] EMO ELEKTRONIK

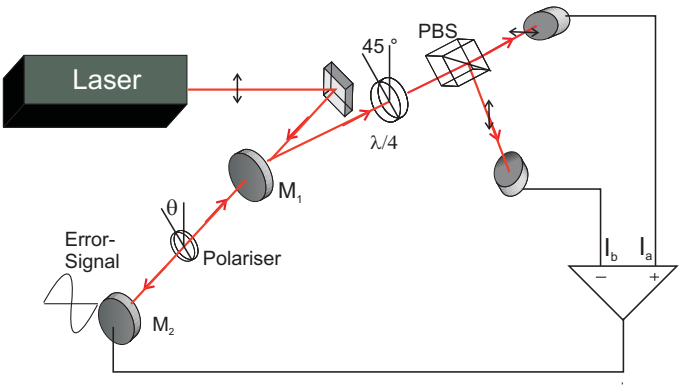

Figure 5.9.: Basic setup of a scheme to lock a cavity to a laser with the Hänsch - Couillaud stabilisation method (based on [81]).

flected from the cavity in the case where, a polarisation element is introduced (see basic setup Fig. 5.9). The linearly polarised light emitted from the laser is coupled into a cavity containing a polariser element in the form of a plate (cf. original proposal [81]). The incident field can be described in terms of the angle, θ, formed between the transmission axis of the polariser and the polarisation axis of the incident laser beam. Therefore, the light can be represented in terms of two orthogonal, linearly polarised components that are parallel or perpendicular to the transmission axis. The component orthogonal to the transmission axis of the intracavity polariser is reflected at the input coupling mirror M_1 while the parallel component accumulates a frequency dependent phase shift when reflected. Thus, the resulting reflected beam becomes elliptically polarised if the relative phase between parallel and orthogonal components changes. The expressions for the parallel and perpendicular components of the reflected beam can be written as

$$E_{\parallel}^{(r)} = E_{\parallel}^{(i)} \left(\sqrt{R_1} - \frac{T_1 R}{\sqrt{R_1}} \frac{\cos(\delta) - R + i\sin(\delta)}{(1-R)^2 - 4R\sin^2(\delta/2)} \right) \qquad E_{\perp}^{(r)} = E_{\perp}^{(i)} \sqrt{R_1} \tag{5.1}$$

with the transmission and reflection of the first mirror R_1 and T_1 and the amplitude ratio between successive round trips R [81]. At resonance, $\delta = 2m\pi$, the reflected field components are in phase. The reflected beam is linearly polarised with a slight angular shift compared to the laser output polarisation. However, if the resonance condition is not fulfilled, Eq. 5.1 implies a phase shift due to the imaginary part of the parallel reflected field component, the reflected beam is elliptically polarised. The polarisation can be analysed using a $\lambda/4$ waveplate and a polarising beam splitter (PBS). If the angle between the fast waveplate axis and the polarisation axis of the PBS is chosen to be 45 °, equal intensity output will be detected in case of resonance. A differential amplifier compares the signals incident on the detectors and the error signal generated (see Eq. 5.2) is used as a servo-loop feedback to the cavity. A piezo actuator element varies the cavity's length according to the output of the operation amplifier.

$$I_a - I_b = I^{(i)} 2\cos(\theta)\sin(\theta) \frac{T_1 R \sin(\delta)}{(1-R)^2 + 4R\sin^2(\delta/2)} \tag{5.2}$$

The generated error signal (see Fig. 5.10 (calculated)) exhibits a zero crossing when the cavity is at resonance and steep slopes on both sides. Due to the significant extension of the wings from the zero crossing, the capture range is large, allowing re-locking even

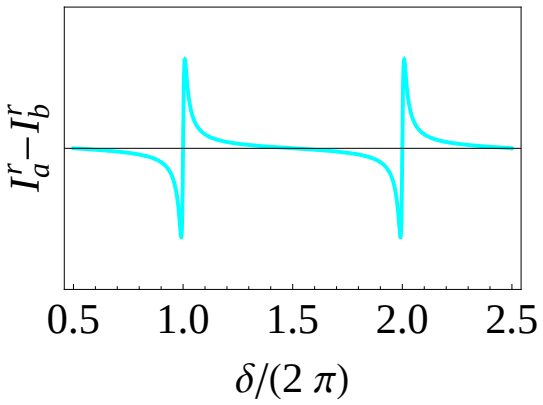

Figure 5.10.: Calculated error signal obtained for a Hänsch - Couillaud locking scheme. The parameters used are: input coupler transmission of $T_1 = 5\,\%$, an amplitude ratio of $R = 0.95$, an angle $\theta = 7.5\,^\circ$ and an incident intensity of $I^i = 1000\,\mathrm{W/m^2}$.

after large frequency excursions. Though the error-signal intensity is maximised for an angle $\theta = 45\,^\circ$ between the incident polarisation and the transmission axis of the incavity polariser, operation at smaller angles does not only offer a better signal-to-noise ratio but also increases the proportion of the light field coupled into the cavity.

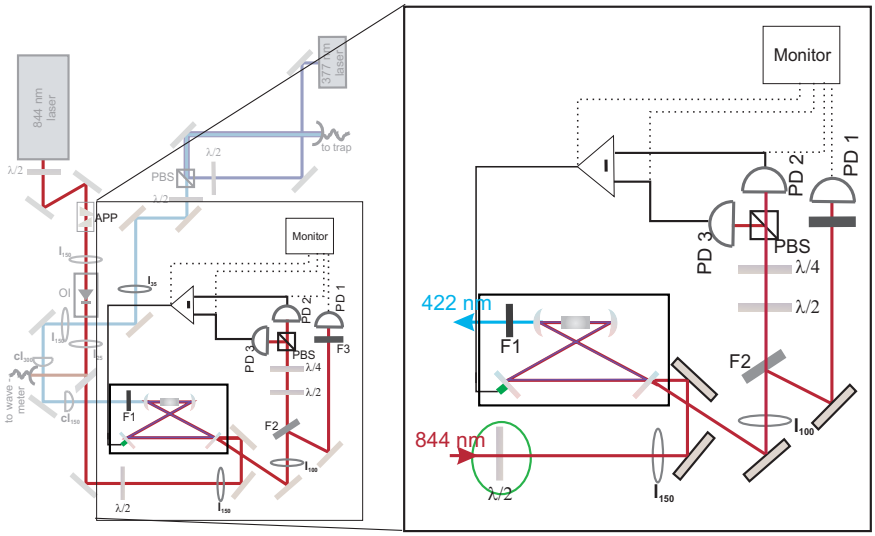

Figure 5.11.: Components used in the actual setup to lock the cavity to the laser; While the green, encircled $\lambda/2$ plate is used to set the angle θ, the combination of the $\lambda/2$ -, $\lambda/4$ waveplate and PBS serve as the polarisation analyser.

Experimental implementation

The setup of the cavity, using a nonlinear crystal for resonant second-harmonic generation, resembles already the basic cavity setup as introduced by Hänsch and Couillaud [81]. The function of the polariser plate is performed by the crystal, that is birefringent and hence can be used to separate the field into components parallel and perpendicular to its transmission axis. The angle θ is determined using a $\lambda/2$ waveplate just before the input coupling mirror of the cavity. The reflected fundamental beam ($\lambda = 844\,\mathrm{nm}$)

exhibits strong divergence and must therefore be focused with a lens ($f = 100\,\text{mm}$, AR coated 700 nm - 870 nm) before it passes through an attenuator plate with a transmission of 10 % (F2). Subsequently the beam passes the polarisation analyser consisting of a $\lambda/2$-, a $\lambda/4$ waveplate and a polarising beam splitter (PBS). The $\lambda/2$ plate followed by the $\lambda/4$ waveplate assures a simple setting of the setpoint i.e. the setting of the outputs according to PD 2 and PD 3 in a way that they cancel at resonance. The p- and s-polarised output signals of the PBS are detected with photodiodes[13] and the resultant signals are fed into a PID controller[14]. As the maximum output of the PDs is 12 V, but the input signal fed into the PID controller must not exceed ±5 V, 10 dB attenuators[15] are introduced. Soldering the pin connections of a Sub-D9-Connector according to the manual [83] allows the use of the PID controller as an operation amplifier which is necessary to calculate the difference of the photodiode signals. The signals shown in Fig. 5.12 are directly subtracted from each other and the result is used in a servo-loop to change the voltage of the piezo actuator[16] at the second mirror, M_2, of the cavity, and hence the cavity length.

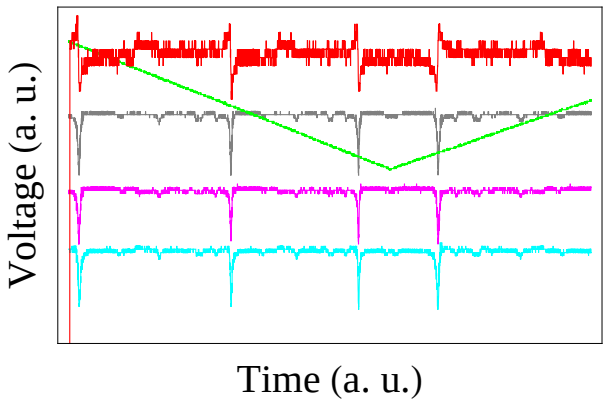

Figure 5.12.: Typical oscilloscope signals obtained from the Hänsch - Couillaud setup shown in Fig. 5.11. CH1 depicts the input on PD1, a reference signal; CH2 and CH3 are the signals from PD2 and PD3; MATHS is the difference given by (CH2 - CH3), and CH4 shows the triangular voltage, scanning the piezo. Small side dips are recognizable in the PD-signals representing additional modes appearing in the cavity. However, they do not influence the locking or conversion efficiency.

5.4. Temperature stabilisation of the crystal

The optimal temperature for the second-harmonic generation is strongly dependant on the fundamental wavelength, but in order to ionise ^{40}Ca a temperature of 76.6 ° has to be chosen. A change of 0.7 ° from this temperature leads to a 50 % reduction of the generated harmonic power (see chapter 3). Control and stabilisation of the temperature is therefore a challenge that has to be met in order to build a reliable source for laser light at 422 nm. To assure good heat conduction and stable positioning, the crystal is surrounded by a 50 μm indium foil[17] and placed within an aluminum mount (see

[13] THORLABS; PDA36A-EC, 400 nm - 1100nm
[14] TOPTICA; PID 110
[15] MINI-CIRCUITS; HAT-10+
[16] THORLABS; AE0203D04F
[17] GOODFELLOW; IN000200/28

Fig. 5.13). Additionally, the entire cavity setup is surrounded by a box. This reduces temperature changes related to airflow and movement in the lab.

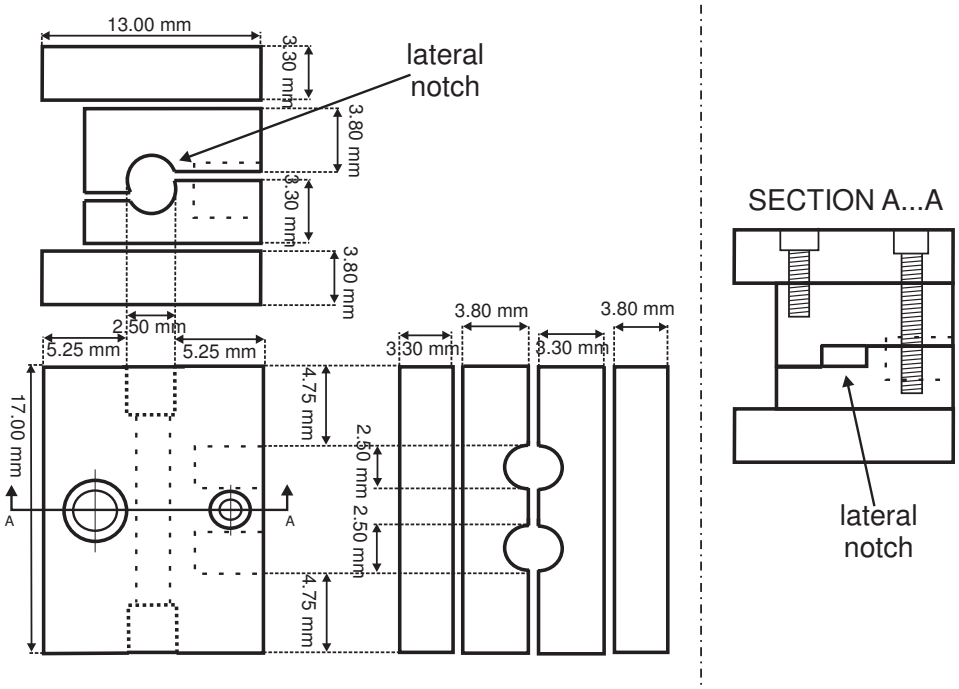

Figure 5.13.: Crystal mount. Not shown are heating wires and temperature sensors. Either end of the lateral notch has been enlarged to maximise the light throughput.

Two distinct temperature control methods were used, differing in the heating agent as well as in the electrical control setup used (cf. Tab. 5.5).

	Setup I	**Setup II**
T agent	Heating wire	Peltier (TEC)
T sensor	NTC and PT100	NTC
Regulator	Home-made Wheatstone Bridge Home-made PID control	Toptica DTC 110 SVL

Table 5.5.: The table compares the components of both setups. Setup II is used to control and stabilise the crystal temperature during the time writing.

The first implemented setup conducted the heat through thermo-coax heating wires[18] that were fixed directly to the crystal mount. The error signal for the PID controller was provided by the output signal from a Wheatstone bridge connected to a PT 100 temperature sensor. An additional PT100 was used for monitoring. The output from the servo was used to control the temperature of the crystal. The long-term temperature stability reached with this setup was 0.1 °C/12 hours, the measured power of second-harmonic light generated as a function of the temperature is plotted in Fig. 5.14a. The data points for that figure were taken with a waiting time of 7 minutes 30 seconds at a pump power of 50.0 mW incident on the cavity and an input coupling of 30 % at a pump wavelength of $\lambda = 845.6$ nm. Maximum second-harmonic generation occurred at

[18] THERMOCOAX; 1NcAc05

a measured temperature of $(67.9 \pm 0.5)\,°C$. The temperature tuning bandwidth was determined to be $(2.4 \pm 0.2)\,°C$ which exceeds the calculated value of $1.4\,°C$ by nearly a factor of two. This discrepancy may be attributable to the measurement method: the temperature of the controller was difficult to set precisely and the step size of the controller was not well calibrated.

The brittle core of the thermo-coaxial cable led to a broken soldering spot between the heating wires and the controller. This should be noted as a possible failure mode for future applications. Repairing the setup by fixing the soldering point led to larger temperature variations $0.24\,°C/12\,$hours and an increased time to heat up the crystal and reach a stable temperature. This can be related to a shorter heating wire leading to a smaller resistance and hence the requirement to increase the current to heat the crystal with the same power as before. However, even previously (with the longer wire) the PID operation was current limited which led to the instabilities.
As the frequency doubling takes place at a temperature within the range of a Peltier element, a change-over of the temperature stabilisation was carried out to circumvent future problems related to the warm up times, temperature stability and the soldering of the heating wires. Thus, a Peltier element[19] was introduced as a heating element receiving an input signal directly from a commercial temperature controller[20]. The temperature is measured with a negative temperature coefficient sensor (NTC). The long-term stability of the setup is better than $0.25\,°C/12\,$hours and the average heating rate is $2.6\,°C$/minute. The measurement of the second-harmonic output power as a function of the temperature is shown in Fig. 5.14b. The data points were taken with a waiting time of 2 minutes, a pump power of 25.0 mW incident on the cavity and an input coupling of 62 % at a wavelength of $\lambda = 845.3\,$nm. Maximum second-harmonic generation is achieved at a temperature of $(76.6 \pm 0.1)\,°C$. The difference of $8.7\,°C$ in the measured maximum temperatures comparing the plots of Fig. 5.14 can be justified by a difference of the fundamental wavelengths of $\approx 0.3\,$nm used for the measurement. This leads to a difference of the period length required to fulfil the phasematching condition. Thus, a shift in the temperature for maximum SHG can be observed. An additional but secondary effect is that setup I measured the temperature directly at the position of the temperature sensors and that values were never calibrated to the temperature at the crystal position. However, a calibration was carried out for the second temperature stabilisation using the Peltier element as heating agent (see App. C for the calibration curve). A temperature measured with an NTC at the same position as the PT100 in the previously used setup was compared to the actual temperature at the crystal position measured with a PT1000. Additionally, while operating the temperature stabilisation over a month, shifts from the initial maximum SHG temperature occurred. Though the mechanism is not yet fully understood, the behaviour might be linked to a self regulation towards thermal equilibrium. However, this will be further investigated. The temperature tuning bandwidth found with the Peltier setup is $(1.7 \pm 0.1)\,°C$ which is in reasonable agreement with the calculated value of $1.4\,°C$.

[19] FARNELL; 5W 1156599
[20] TOPTICA; DTC 110 SVL

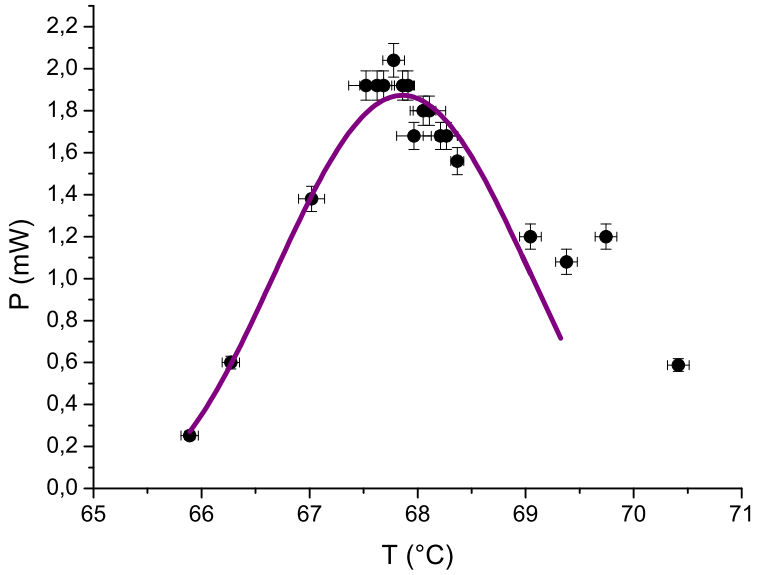

(a) Power vs temperature setup I

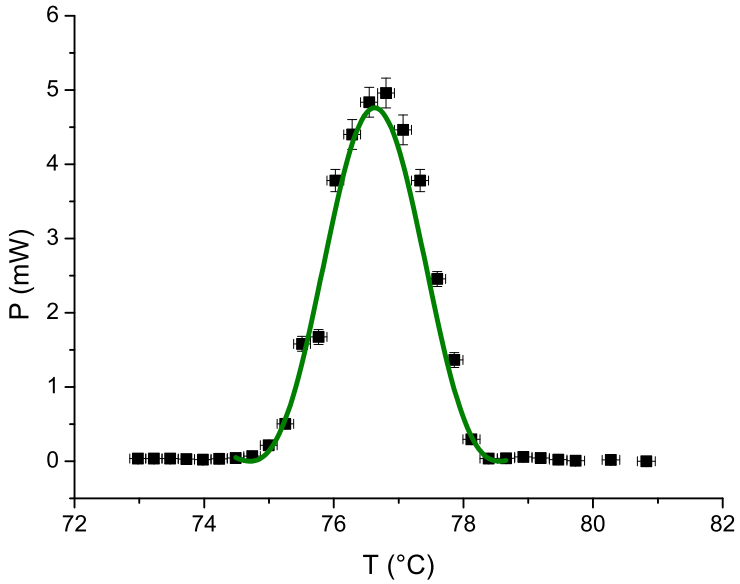

(b) Power vs temperature setup II

Figure 5.14.: The optical power is plotted as a function of the crystal temperature. The fit is carried out using the function $P = A\mathrm{sinc}^2(\pi w(T - T_\mathrm{c}))$ with the amplitude fit parameter denoted A, the parameter influencing the width of the curve w and the shift of the peak value given as T_c. The fit parameters for Fig. (a) are $A = (1.9{\pm}0.1)\,\mathrm{mW}$, $w = (0.35{\pm}0.01)\,(^\circ\mathrm{C})^{-1}$ and $T_\mathrm{c} = (67.9{\pm}0.5)\,^\circ\mathrm{C}$. Fig. (b) shows a similar curve for the setup using the Peltier element as heating agent. The fit parameters are $A = (4.8 \pm 0.5)\,\mathrm{mW}$, $w = (0.52 \pm 0.01)\,(^\circ\mathrm{C})^{-1}$ and $T_\mathrm{c} = (76.6 \pm 0.1)\,^\circ\mathrm{C}$. The large temperature difference for maximum SHG power can be attributed mainly to a difference in the fundamental wavelengths of $\approx 0.3\,\mathrm{nm}$ for the measurements.

5.5. Fibre coupling and overlap with 377 nm laser

As a concluding step for the photoionisation laser system, the laser beams for the transitions at 377 nm and 422 nm respectively have to be overlapped and coupled into a fibre to deliver light to the trap. Fig. 5.15 depicts the components used. Presently, this part of the system is over determined as it consists of four mirrors: two mirrors to steer the 422 nm beam and the 377 nm beam, respectively. It also has four degrees of freedom to couple the light into the fibre, introduced by an additional mirror and the fibre holder. However, up to now this choice of assembly has been beneficial in order to optimise the fibre coupling efficiency. Overlapping of both beams is realised with a PBS and using a $\lambda/2$ waveplate to adjust the beam polarisation. After coupling the 422 nm laser light into the fibre using mirror M (see Fig. 5.15) and the fibre holder, the 377 nm laser light is superimposed, using mirrors M_c and M_d.
The single mode fibre[21], with a transmission wavelength at 400 nm, is connected with a fibre collimator[22] to the fibre holder. Therefore, an adjustment is possible to improve the coupling efficiency if the mode of the laser does not overlap properly with the fibre's mode. While the mode of the 422 nm laser is well shaped and an input coupling efficiency of 30 % was reached with the fibre collimation lens in the original position set by the company, the input coupling for the 377 nm laser was as low as 5 %. Thus, the fibre collimation lens was slightly adjusted to increase the coupling efficiency at the lower wavelength. The measurement showed a conflictive behaviour for the input coupling efficiencies, that could either be maximised for the 377 nm light with poor 422 nm light coupling or vice versa. The final setting, which is the optimum if both wavelengths are coupled in as well as possible, led to an input coupling efficiency of 13 % at 422 nm and 11 % at 377 nm.
When the fibre lens is adjusted for maximal coupling of the 422 nm light, the mode of the 377 nm laser is not well coupled into it. Using only one additional lens in the 377 nm beam (directly in front of the diode) offers insufficient degrees of freedom to perfectly mode match this beam into the fibre. The mode matching could be improved with further beam shaping optics, but the total coupled power at present is sufficient to perform experiments.

5.6. Summary

The characterisation of the 844 nm laser showed a threshold current of $I_{\mathrm{th}} = 68.0\,\mathrm{mA}$ and a slope efficiency of $\eta_{\mathrm{S}} = 0.72\,\mathrm{W/A}$. Due to the losses of 34 % over the beam path, a maximum optical power of 65 mW incident on the cavity can be achieved. The 422 nm light is generated in a ppKTP crystal at a temperature of $T = 76.6\,^{\circ}\mathrm{C}$. This temperature value is valid for a fundamental wavelength in air[23] of 845.3499 nm. Changes of this value lead to a modified phase-matching condition and result in a shift of the temperature for maximum SHG. The crystal temperature is controlled and stabilised using a Toptica box (DTC 110 SVL). The second-harmonic light generated is enhanced using a bow-tie cavity having a finesse of 20, losses in the cavity due to scattering of light from the crystal, absorption in the crystal and conversion losses are estimated to be at 8 %. The maximum generated second-harmonic light power was 13 mW at a fundamen-

[21] AMS TECHNOLOGIES; QPMJ 3A3A 400-3/125-3-10-1
[22] SCHÄFTER KIRCHHOFF; 60FC-4-A6,2S-01
[23] This is the setting for the wavemeter.

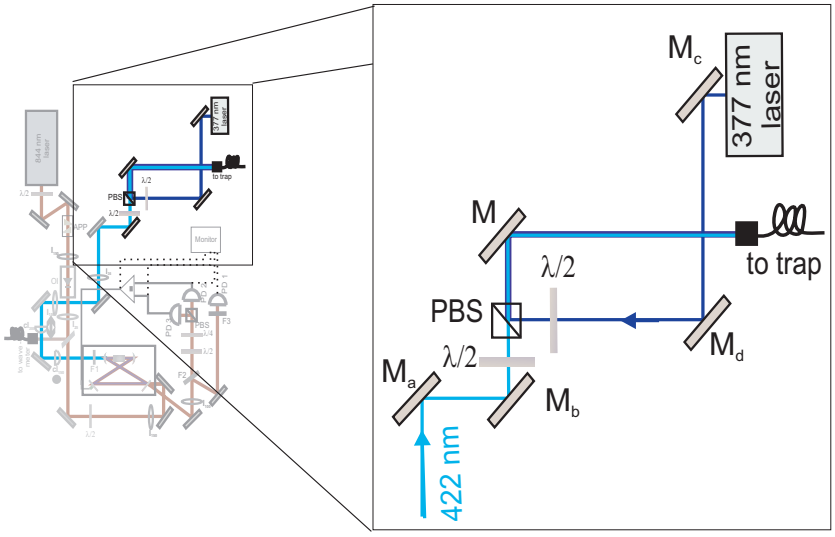

Figure 5.15.: Setup used to achieve overlapping and fibre coupling of the 377 nm and 422 nm laser light. Both beams can be independently steered by two mirrors in front of the waveplates and the PBS, in order to guarantee good overlap.

tal light power of 65 mW. For the first experiments the incident power was reduced to 15 mW producing a second-harmonic light power of 0.6 mW. The stabilisation is performed using the Hänsch - Couillaud locking scheme, stabilising the cavity to the laser. The 377 nm laser has a threshold current of $I_{\mathrm{th}} = 50.0\,\mathrm{mA}$ and a slope efficiency of $\eta_{\mathrm{S}} = 0.41\,\mathrm{W/A}$. The low slope efficiency (less than half the value denoted in the specifications) is attributed to dirt on the diode window which could not be removed. The maximum optical power was measured to be 20.0 mW, and at the time of writing the typical value used for experiments was 6.0 mW.
Coupling of the photoionisation light to the trap is assured using a single mode, optical fibre centered at a wavelength of 400 nm. Input coupling efficiencies are around 13 % for the 422 nm laser and 11 % for the 377 nm laser.
While the setup described in this chapter has been tested to be fully functional (see chapter 6) one future improvement is to increase the fibre coupling efficiency by introducing better mode shaping of the 377 nm laser. Furthermore, both, the cavity itself and the setup as a whole need stable housing in order to decrease the influence of external perturbations.

6. Experimental Implementation

The aim of the work presented here is the assembly of a laser system to photoionise ^{40}Ca using a frequency - doubling system for 422 nm light and a laser diode at 377 nm wavelength. The ultimate purpose of the photoionisation setup is to enable ion trapping using radio-frequency (RF) fields in various experimental setups. The previous chapters provided a description of the theoretical considerations behind the system (chapter 2 - chapter 4), and the assembly of said system (chapter 5). The system's application that verified full functionality is described here.

This chapter introduces the surface-trap used in Sec. 6.1 and the vacuum chamber at hand in Sec. 6.2. Furthermore, the detection using a CCD camera will be described in Sec. 6.3 and finally, the experimental results will be presented in Sec. 6.4.

6.1. Surface-electrode trap

The operation principles for surface-electrode traps [37, 38] rely on the same basic physics as the commonly-used linear traps [15, 16, 84]. A brief introduction to linear traps will therefore be given before the change to surface-electrode traps is described and motivated .

Linear Paul Trap

Parabolic potentials mediate linear forces, that enable the confinement of a particle to a particular region. One possibility to generate such potentials is electric - and magnetic multipole fields [15]. One commonly used way of producing such fields is a linear ion trap (see Fig. 6.1). This provides a combination of a spatially-varying, time-dependent electric field in the RF-frequency range and a static electric field [16]. The potential, $(\Phi(x, y, z, t))$, can be written as follows [16]

$$\Phi(x, y, z, t) = \frac{U}{2}(\alpha x^2 + \beta y^2 + \gamma z^2) + \frac{V}{2}(\alpha' x^2 + \beta' y^2 + \gamma' z^2) \tag{6.1}$$

where U denotes the DC voltage, V is the RF voltage and α,β,γ and α',β',γ' are constants fixed by the geometry. As the potential has to obey the Laplace equation, $\Delta\Phi = 0$, at any time, there are constraints to the coordinate constants:

$$\begin{aligned} \alpha + \beta + \gamma &= 0 \\ \alpha' + \beta' + \gamma' &= 0. \end{aligned} \tag{6.2}$$

For the geometry of the linear RF trap which is characterised by a radial confinement in the x-y plane due to the RF field and a DC confinement in the z direction (cf. Fig. 6.1),

the choice to fulfil these conditions is

$$\begin{aligned} -(\alpha+\beta) &= \gamma > 0 \\ \alpha' &= \beta' \\ \gamma' &= 0. \end{aligned} \tag{6.3}$$

Having determined the relationship between the coordinate constants, it is possible to write down the equations of motion in all directions for a particle of mass m and charge $Z|e|$ within the designated potential. A simple transformation to dimensionless constants using the parameters given in Eq. 6.4 gives rise to the Mathieu differential equation as written in Eq. 6.5 [16].

$$a_{\mathrm{x}} = \frac{4Z|e|U\alpha}{mr_0^2\omega_{\mathrm{rf}}^2} \qquad q_{\mathrm{x}} = \frac{2Z|e|V\alpha'}{mr_0^2\omega_{\mathrm{rf}}^2} \qquad \tau = \frac{\omega_{\mathrm{rf}}t}{2} \tag{6.4}$$

$$\frac{d^2x}{d\tau^2} + [a_x - 2q_x\cos(2\tau)]x = 0 \tag{6.5}$$

The solution to this equation can be derived using the Floquet theorem which is beyond the scope of this thesis but is nicely described in [16]. In principle, a distinction can be made between stable solutions, which confine the oscillating particle, and unstable solutions. A commonly used 3D realisation as a linear trap setup (with stability parameters $q_z = \gamma' = 0$; $q_y = -q_x$) is depicted in Fig. 6.1. Typically, the parameters from Eq. 6.4 are chosen to be around $a_x = 0$ and $q_x < 0.5$.

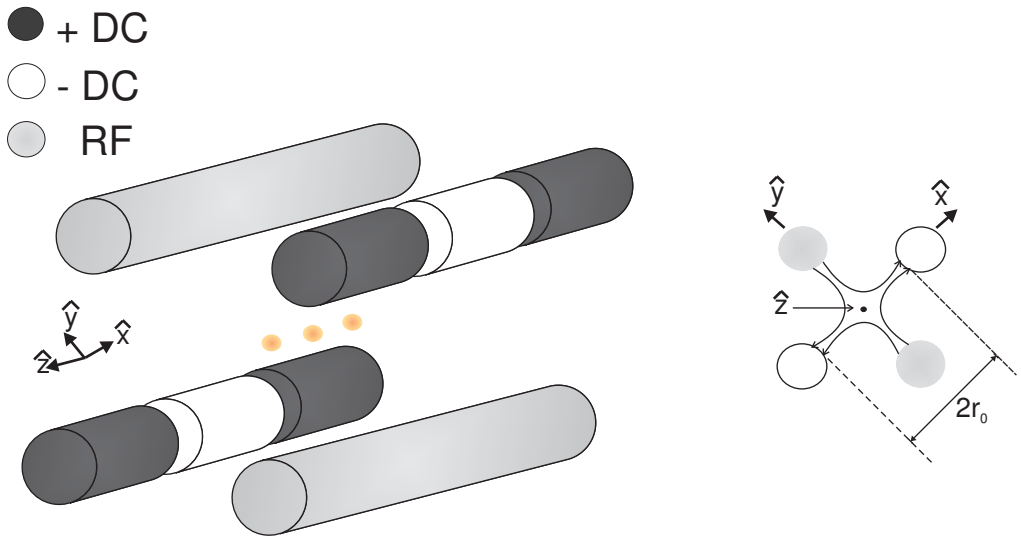

Figure 6.1.: Electrode arrangement for a linear trap. While the applied RF-frequency potential assures radial confinement, confinement in the z direction is implemented by applying a DC voltage to the outer segments [16]

Even once an ion is trapped and cooled the residual ion motion within the trap is not generally negligible. It consists of a slow secular motion (in the MHz range) which describes a harmonic oscillation of the ion within the time averaged trapping potential and 'micromotion', which is a fast movement at the trap-drive frequency, modulating the secular motion. The amplitude of the micromotion is minimised on the RF axis of the trapping potential.

Surface-Electrode Ion Trap

Trapped ions in a string arrange themselves into a linear (rather than zigzag) configuration, provided the confining potential is sufficiently anisotropic [85]. That is to say, the ratio of the axial to radial frequencies, ω_z^2/ω_r^2, must be sufficiently low. The critical ratio becomes lower for increasing ion number.
Naively, ion trap quantum computing could be scaled by increasing the number of ions in a harmonic potential. However, the constraint on trap isotropy gives rise to problems when scaling to large ion numbers [34]. Namely, if the axial frequency is reduced in order to retain a linear configuration, then the gate speed of the computation is also reduced. Conversely, if the axial frequency is kept constant (and the radial frequency increased), then the mode structure of the many-ion string becomes so dense as to create significant limitations on mode-specific laser addressing.
In order to use the extraordinary scaling properties of quantum computing using many ions, many separate traps can be used, each holding a small number of ions [36, 38, 86]. To facilitate the fabrication and scaling of such architectures to include many trapsone approach to scale down linear traps is to 'open' the 3D geometry, arranging all electrodes in one plane (for example, as in Fig. 6.2b). The trapping region is along the symmetry line above the trapping electrodes.

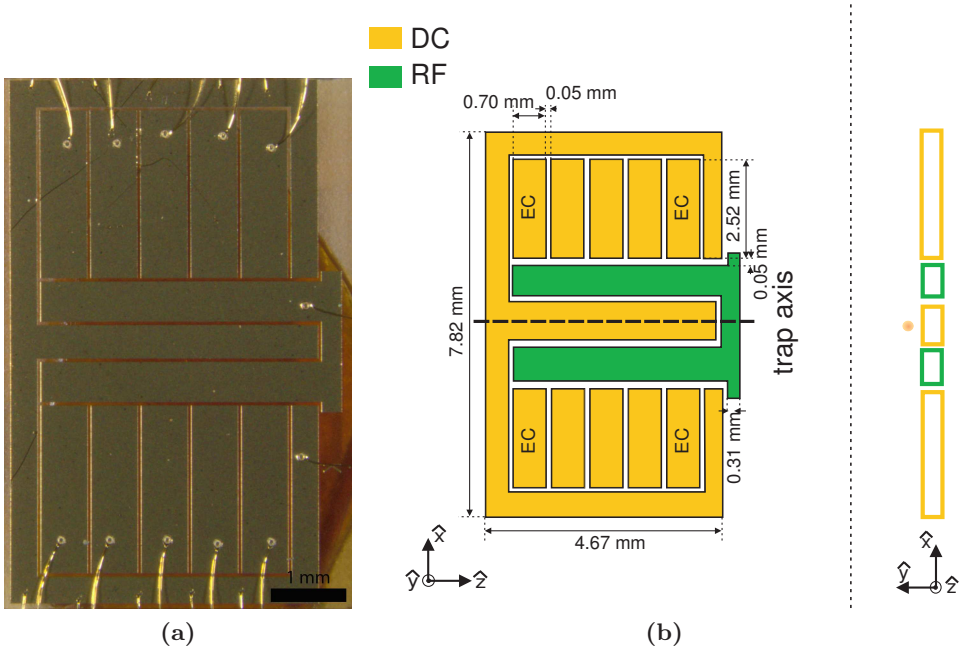

Figure 6.2.: (a) Photograph of the trap with visible gold wire bonds. (b) Plan view and cross section of the electrode arrangement and specifications for the surface-electrode trap are illustrated. EC denotes the segments used as end cap electrodes.

As illustrated in Fig. 6.2b the trap consists of eleven DC electrodes (yellow) that serve as RF ground and two RF electrodes (green) which are held at DC ground. The ions are trapped along the trap axis, marked with a dotted line (plan view) and a dot (cross section). According to simulations the ion - electrode distance is 485 μm. The five segments of the outermost electrodes can be individually addressed, allowing a superposition of the RF-frequency nodes and the saddle point of the static potential and thereby min-

imising micromotion.
The trap was fabricated at ETH Zürich by N. Daniilidis using gold on a sapphire substrate. Its average surface roughness, as measured with an atomic force microscope, and with a profilometer is $\approx 20\,\mathrm{nm}$. However, some additional dirt deposition in form of clusters with a size in the μm range has been observed over the whole surface. The trap is mounted on a standard CPGA (ceramic pin grid array) chip carrier using a stack of glass spacers to set the correct height of the chip. The trap is connected to the chip carrier using $25\,\mu$m gold wire bonds facilitating individual voltage supply for every electrode. The electrodes have a width of $700\,\mu$m and the gaps between them are $50\,\mu$m across. The applied RF-frequency voltage of 620 V peak to peak with a frequency of $2\pi\times10.5\,\mathrm{MHz}$ results in a radial trapping frequency of $\omega_\mathrm{r} = 2\pi \times 3\,\mathrm{MHz}$ (calculated). The applied DC end cap voltage ensures axial trapping of the ion (z axis) and is set to 40 V. DC voltages of -8 V are applied to the remaining segmented electrodes in order to overlap the minima of the pseudopotential created by the applied RF voltages and saddle point of the DC potentials.

6.2. Vacuum chamber

The vacuum system used during the experiments and described here was built by M. Niedermayr (see Fig. 6.3). It is based on an octagonal chamber[1] and has an outer diameter of 212.3 mm, an inner diameter of 160.0 mm and a height of 70.6 mm. Seven of the lateral ports as well as the bottom port are sealed with viewports[2] allowing optical access (the window diameter and the inner diameters of the ports are 38.1 mm). The eighth lateral port is used as a feedthrough for the ion-pump systems. The typical system pressure was reduced from $10^{-9}\,\mathrm{mbar}$ to $10^{-11}\,\mathrm{mbar}$ after the first heating of the Ca-oven and subsequent tightening of the screws and nuts. The top port has three feedthroughs: one to offer a connection for the DC wires from the filterboard to the trap, one to supply current to the Ca-oven and a third to apply RF-frequency voltage to the trap. The oven is formed by a stainless steel tube with a diameter of 2 mm, filled with calcium. As the trap is mounted top down in the centre of the vacuum chamber, the bottom viewport provides optical access for fluorescence detection with a CCD camera as described in Sec. 6.3.

6.3. Imaging

The ion fluorescence is detected using a CCD camera[3]. Fluorescence light is collected using an objective[4] ($\mathrm{f} = 66\,\mathrm{mm}$) that is mounted on a xyz stage[5] beneath the vacuum setup (see Fig. 6.3). The objective is positioned so that the trap electrodes are in focus and imaged onto the CCD camera with a magnification of 3.5. The objective can be moved (using the translation stage) to focus on the expected trapping region, $485\,\mu$m from the trap surface. It should be noted that one full turn of the micrometre screw

[1] KIMBALL; MCF800-SO2000800 Spherical Octagon with Metric Threaded Holes
[2] TORR SCIENTIFIC
[3] L.O.T.-ORIEL; A-DV 885-KC-VP iXon + EMCCD Detektor
[4] SILLOPTICS
[5] NEWPORT; M 461

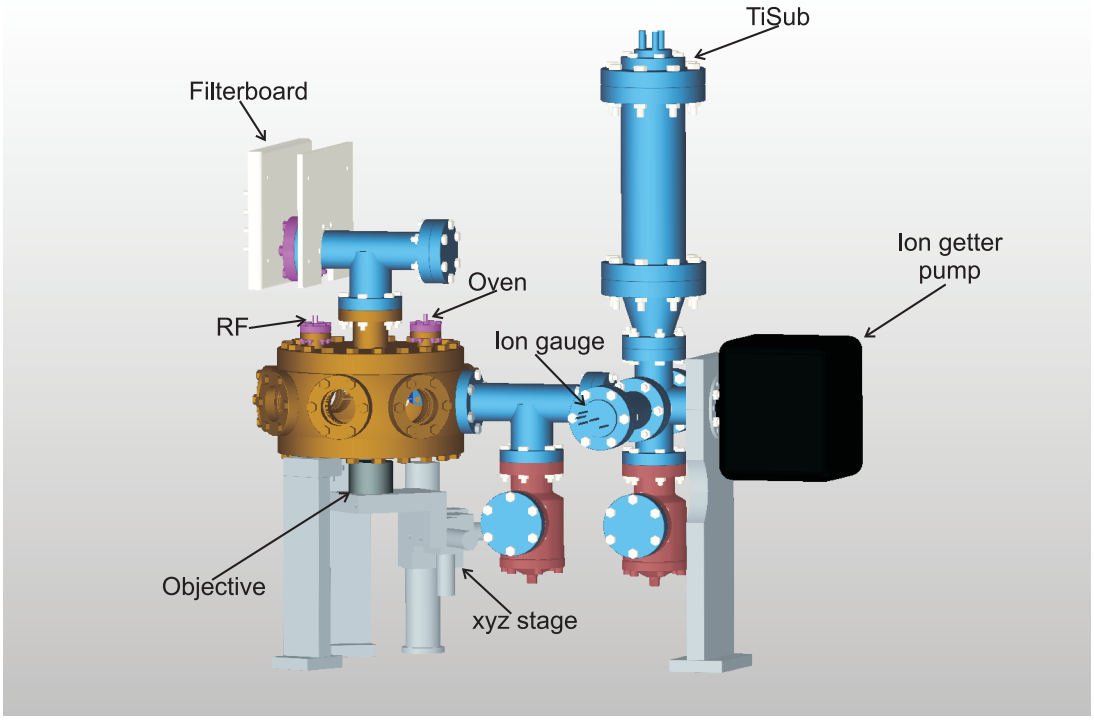

Figure 6.3.: Schematic of the present vacuum setup. (Courtesy of Michael Niedermayr)

corresponds to a change in position of 500 μm. In order to detect only certain wavelengths, narrow band-pass filters[6] centered at 417 nm and 395 nm are used. These allow detection of atomic fluorescence during loading, and detection of scattered cooling light during Doppler cooling.

6.4. Experimental results

Full functionality of the doubling system contributing to the photoionisation setup has been proven by measuring atomic fluorescence. In addition, the first ions trapped in our setup with a surface-electrode trap will be presented here. In the following, both measurements, the atomic fluorescence detection and the observation of the first trapped ions, are described including information regarding the experimental settings.

6.4.1. Atomic fluorescence

For the measurement of the atomic fluorescence the transition at 422 nm wavelength is used to excite the atoms. The light emitted as the excited atoms decay back to the ground state is observed with the CCD camera using a band-pass filter centered at 417 nm ($\Delta\lambda = 30$ nm) to reduce background light. The light is delivered from the photoionisation setup to the trap using a single mode optical fibre[7]. The fibre output is focused using a lens ($f = 300$ mm, AR coated 370 nm to 430 nm) to create a waist of approximately $w_0 = 75\,\mu$m at the centre of the trap. Two mirrors are introduced before the trap in order to align the beam (see Fig. 6.4).

[6] SEMROCK; FF01-395/11-25, FF01-417/60-25
[7] AMS TECHNOLOGIES; QPMJ 3A3A 400-3/125-3-10-1

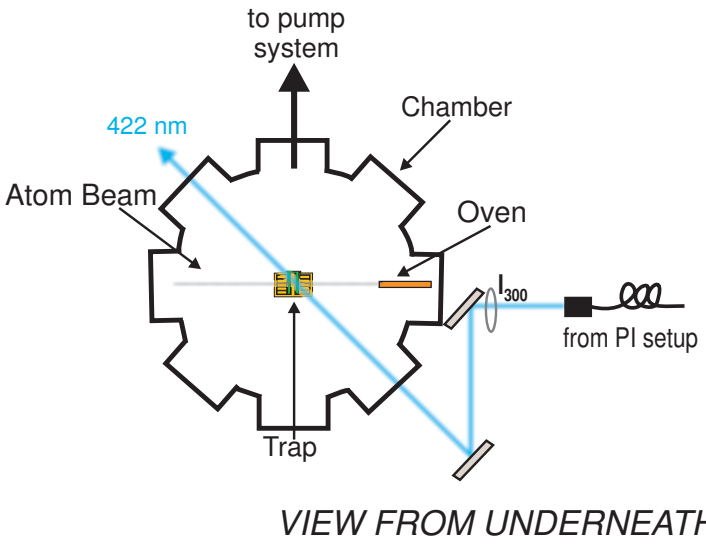

Figure 6.4.: Components used to guide the 422 nm laser beam through the chamber. Not to scale.

The current used to heat the oven was increased from 6 A to a final value of 11.25 A before fluorescence was first observed. A waiting time of several minutes between each current step assured outgassing of the oven without excessively heating it. After every current step an increase in the pressure could be observed followed by a slow return to the initial pressure value. This can be attributed to dirt residues in the oven that were evaporated during heating and filtered out of the system by the ion getter pump. The initial pressure of the vacuum chamber was 10^{-9} mbar which increased while running the oven to a final value of 10^{-8} mbar for the first observations of ions. When the process of outgassing the oven was completed, the oven current could be reduced to a value of 8.5 A for additional measurements and the pressure stayed in the range of 10^{-9} mbar. A minimum value of 7 A is needed in order to produce a discernable calcium beam. As the atom beam from the oven has a certain velocity distribution, the frequency the atoms 'see' is different from the value originally set, due to the Doppler shift $\nu_{\text{atom}} = \nu_{\text{Laser}}\left(1 - \frac{v_{\text{atom}}}{c}\right)$. In order to account for the Doppler shift of the transition frequency and to correct for drifts of the laser frequency (which is not locked), the laser with central fundamental wavelength of 845.3455 nm is scanned over a range of 2 GHz at a repetition rate of once every 5 s. For the second-harmonic light generated in the doubling system this corresponds to a central wavelength of 422.67275 nm and a scanning range of 4 GHz at the same scan duration. The parameters for first observing atomic fluorescence are a fundamental wavelength of (845.348 ± 0.002) nm (second-harmonic wavelength of (422.674 ± 0.001) nm) at an oven current of 11.25 A and a pressure of 10^{-8} mbar (see Fig. 6.5). The discrepancy of 2.3 GHz between the measured transition wavelength and the literature value (422.67262 nm) can be attributed to a systematic inaccuracy when dealing with the value given by the wavemeter. In contrast to the literature value that gives a vacuum wavelength, the wavemeter measures the wavelength in air and calculates the vacuum value. Hence, ambient conditions such as pressure and temperature influence it.

Further measurements at 8.5 A showed a production of the calcium beam after 90 s leading to a clear fluorescence signal. This signal decreases from maximum value to zero within 20 s after turning of the oven (cf. Fig. 6.6).

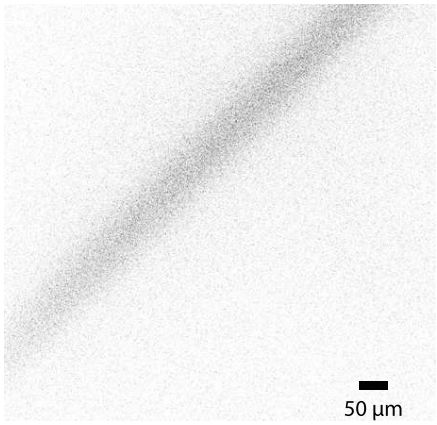

Figure 6.5.: The observed atomic fluorescence for a ^{40}Ca beam as inverse picture.

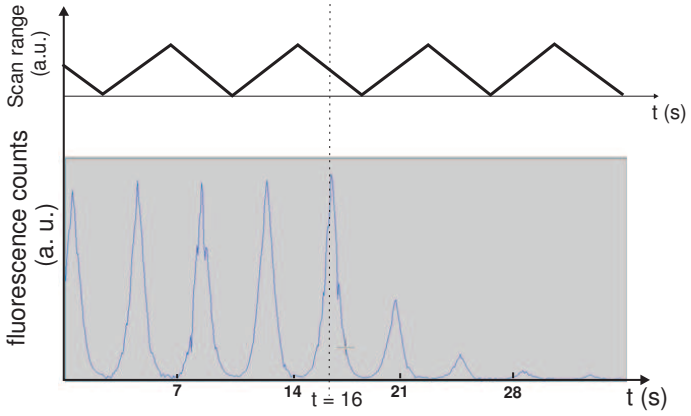

Figure 6.6.: Fluorescence counts as a function of time with the laser being scanned across the atomic resonance. The oven was turned off at $t = 16\,\mathrm{s}$.

6.4.2. Loading

Having tested the frequency doubled system at 422 nm and having determined the settings required to observe atomic fluorescence, attempts were made to trap $^{40}Ca^{+}$. Both photoionisation wavelengths (422 nm and 377 nm) traverse the trap collinearly, along the path illustrated in Fig. 6.4. Additionally, laser beams at 397 nm and at 866 nm are overlapped with the photoionisation beams in a counter propagating direction (cf. Fig. 6.7).

Ions that are produced with the photoionisation lasers are trapped by the applied RF-frequency and static potentials. The 397 nm wavelength transition is used to detect the ions (see Fig. 2.2) while the laser at 866 nm is used to repump the ions from the long-lived (dark) $D_{3/2}$ state into which they would otherwise be optically pumped. To get a good signal both the filters at 417 nm and at 395 nm ($\Delta\lambda = 7\,\mathrm{nm}$) were used. The settings of the trap were a peak to peak voltage of 620 V, an endcap voltage of 40 V, a DC voltage of $-8\,\mathrm{V}$ for the remaining segmented electrodes and an RF-frequency of $\omega_{\mathrm{rf}} = 2\pi \times 10.5\,\mathrm{MHz}$. Scanning both the 397 nm - and the 866 nm laser over a range of approximately 2 GHz produced the picture in Fig. 6.8.

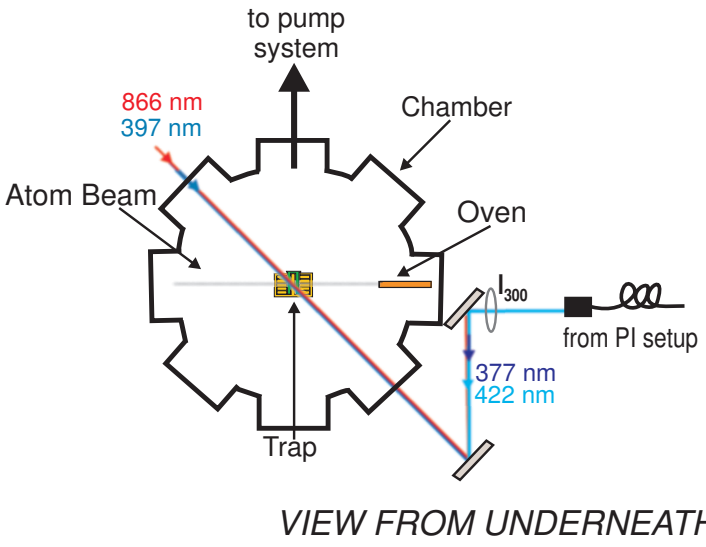

Figure 6.7.: Beam paths for the lasers used to trap ions. Not to scale.

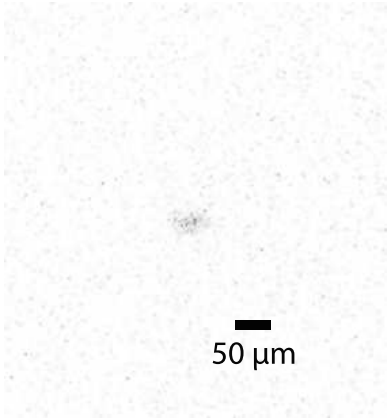

Figure 6.8.: The first ions trapped in the room-temperature setup with a surface-electrode ion trap (inverse photograph).

6.5. Summary

The development of linear RF traps to planar, scalable trap geometries increased the need for clean and fast loading methods. Due to the advantages mentioned in chapter 2, photoionisation represents a good implementation of this, fulfilling the requirements posed. This chapter describes the validation of full functionality of the photoionisation system laid out in chapter 2.
First, a short introduction of the system components is given which covers a brief survey of the working principles of a linear RF ion trap and the transition to a surface-electrode tap. The trap, the vacuum chamber and imaging systems are described in detail. Finally, the experimental results are presented.
Atomic fluorescence was observed at a fundamental wavelength of (845.348 ± 0.002) nm which corresponds to a second-harmonic wavelength of (422.674 ± 0.001) nm with an oven current of 11.25 A and a pressure of 10^{-8} mbar. For additional measurements the oven current could be reduced to 8.5 A and the pressure decreased to 10^{-9} mbar. For the first ions trapped the voltages of the surface-electrode trap were a peak to peak voltage of 620 V, an endcap voltage of 40 V, a DC voltage of -8 V for the remaining segmented

electrodes and an RF-frequency of $\omega_{\mathrm{rf}} = 2\pi \times 10.5\,\mathrm{MHz}$. After having photoionised the calcium, the lasers at 397 nm and 866 nm were scanned to assure cooling, repumping and detection.

7. Conclusion and Outlook

This thesis describes the theoretical and experimental prerequisites to achieve photoionisation of calcium with a frequency-doubled 422 nm laser and a 377 nm laser diode. Particular emphasis is given to the topic of frequency doubling. This work also presents results that demonstrate the system to be fully functional.
A brief review of the theory of nonlinear optics is given, in order to theoretically introduce frequency doubling using a nonlinear crystal. The results for the case of a nonlinear crystal interacting with Gaussian beams, which well describes the behaviour of a real laser beam, is given. Different possibilities to tune the power of the second harmonic generated are presented with a certain emphasis on the technique used - namely quasi-phasematching. As the doubling system should be implemented with an ordinary diode laser with maximum optical output power in the range of 100 mW, a cavity in bow-tie configuration was chosen in order to increase the fundamental power in the crystal and thereby increase the effective conversion efficiency. The theoretical considerations are given in detail, allowing the reconstruction of the steps taken and the implementation for the system at hand.
The thesis describes the experimental components used to implement the photoionisation system. The beam shaping of both the fundamental light at 844 nm and the second-harmonic light at 422 nm is characterised. Furthermore, the cavity and crystal parameters are stated and both the theory and implementation of the Hänsch - Couillaud locking scheme is given. As temperature tuning emerged to be a crucial step in order to generate maximum second-harmonic optical power, the setups used to control and stabilise the crystal temperature are introduced. Differences between the setups, and possible failure modes are pointed out in order to refine future applications. Additionally, the beam path of the 377 nm laser and the overlap of it with the 422 nm light are described.
A first test demonstration of the functionality of the 422 nm light source has been the observation of atomic fluorescence. The fluorescence signal could be first measured at an oven current of 11.25 A which caused the background pressure to rise to 10^{-8} mbar. In addition, the photoionisation setup was tested to fully ionise ^{40}Ca and ions were trapped in our surface-electrode trap at room temperature for the first time. For this purpose, the two-step photoionisation process was turned off after a time sufficient to produce ions and the lasers at 397 nm and 866 nm were scanned to assure Doppler cooling, repumping and detection of the trapped ions.

Currently, the system has been in operation for several months and has been shown to operate reliably. Small adjustments must be made in order to guarantee optimal 422 nm light generation. In the future, and in addition to its use to produce calcium ions in a room-temperature setup, the photoionisation system will be used to load a trap at cryogenic temperatures. As reliable loading is available, a characterisation and optimisation of the trap apparatus will be the next step in order to achieve the long-term goal of trapping two-dimensional ion configurations.

A. A Survey of Frequency Doubling

This appendix provides an expansion of the formalism introduced in chapter 3. The considerations are derived in more detail for the nonlinear wave equation in Sec. A.1 and for the analysis of frequency doubling with Gaussian beams in Sec. A.2.

A.1. Deriving the nonlinear wave equation

Using the description of wave propagation in matter as given in Eq. 3.5, single-frequency Helmholtz equations can be derived (Eq. A.1).

$$\left(\nabla^2 + \frac{n^2(\omega_l)\omega_l^2}{c^2}\right)\mathcal{E}(\mathbf{r},t)e^{i\mathbf{kr}} = -\frac{\omega_l^2}{\epsilon_0 c^2}\mathcal{P}_l(\mathbf{r}) \tag{A.1}$$

To obtain this, different frequency components $\mathbf{P}^{NL}(\mathbf{r},t) = \sum_l (\mathcal{P}_l(\mathbf{r})e^{-i\omega_l t} + \ c.c.)$ and the formalism introduced in Sec. 3.1 for the field have to be used [65]. Eq. A.1 can be simplified by confining the wave propagation to one dimension and using the assumption that the amplitude changes slowly compared to the wavelength[1].

$$\left|\frac{\partial^2\mathcal{E}(z)}{\partial z^2}\right| << k\left|\frac{\partial\mathcal{E}(z)}{\partial z}\right| \tag{A.2}$$

Applying this approximation to equation A.1 the formula is given as

$$\left(2ik\frac{\partial}{\partial z}\underbrace{-k^2 + \frac{n^2(\omega_l)\omega_l^2}{c^2}}_{=0}\right)\mathcal{E}(z) = \frac{\omega_l^2}{\epsilon_0 c^2}\mathcal{P}_l(z)e^{-ikz} \tag{A.3}$$

which finally leads to the coupled wave equations for $\mathcal{P}_l(z)e^{-ikz} = 4\epsilon_0 d_{\text{eff}}\mathcal{E}_m\mathcal{E}_n e^{-i\Delta kz}$:

$$\begin{aligned}
\frac{d\mathcal{E}_3(\omega)}{dz} &= \frac{2i\omega d_{\text{eff}}}{cn(\omega)}\mathcal{E}_1\mathcal{E}_2 e^{-i\Delta kz} \\
\frac{d\mathcal{E}_1^*(\omega_1)}{dz} &= \frac{-2i\omega_1 d_{\text{eff}}}{cn(\omega_1)}\mathcal{E}_3^*\mathcal{E}_2 e^{-i\Delta kz} \\
\frac{d\mathcal{E}_2^*(\omega_2)}{dz} &= \frac{-2i\omega_2 d_{\text{eff}}}{cn(\omega_2)}\mathcal{E}_1\mathcal{E}_3^* e^{-i\Delta kz}
\end{aligned} \tag{A.4}$$

with d_{eff} the effective susceptibility and $\Delta k = k - k_m - k_n$.

[1] This is sometimes referred to as the slowly varying envelope approximation or slowly varying wave approximation [66, 68]

A.2. The Boyd-Kleinman approach

In this section, Eq. 3.19, which describes the power of a generated second-harmonic wave, will be derived. A detailed discussion of circular Gaussian beams and their interaction with anisotropic media can be found in the original paper by Boyd and Kleinman [74]. The analysis here is strongly based on the online support material connected to [71] originating from the same assumptions but written in the SI system.

A circular laser beam is described in terms of Gaussian modes (cf. Fig. A.1)

$$E(r) = \frac{\mathcal{E}_0}{2}\frac{w_0}{w(z)}e^{-\frac{\alpha_1}{2}z}e^{\frac{r^2}{w^2(z)}}e^{-i(k_1 z-\Psi(r,z)-\Phi(z))} \tag{A.5}$$

where $r = \sqrt{x^2+y^2}$ is the distance to the z axis in which the beam propagates, $\mathcal{E}_0$ denotes the amplitude, k_1 is the wave vector in a medium and α_1 is an attenuation factor. Furthermore Eq. A.5 contains the waist, w_0, the beam radius, $w(z)$, the Guoy phase, $\Phi(z)$, and a term $\Psi(r,z) = \frac{k_1 r^2}{2R(z)}$ which includes the beam curvature $R(z)$.

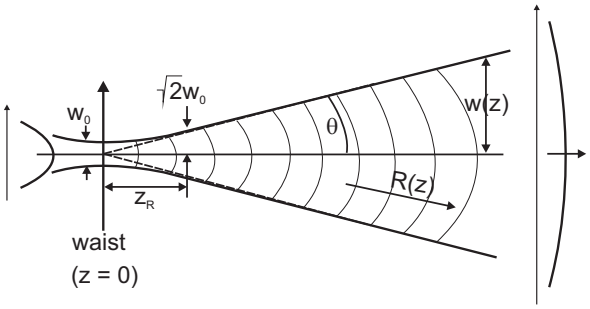

Figure A.1.: Gaussian beam shape introducing the parameters relevant for its description.

$$\begin{aligned} w(z) &= w_0\sqrt{1+\left(\frac{\lambda z}{\pi n w_0^2}\right)^2} && \text{beam radius} \\ R(z) &= z\left(1+\left(\frac{\pi n w_0^2}{\lambda z}\right)^2\right) && \text{beam curvature} \\ z_0 &= \frac{\pi n w_0^2}{\lambda} && \text{Rayleigh length} \end{aligned} \tag{A.6}$$

For the further analysis the confocal parameter, b, and the diffraction half angle, θ, are of importance:

$$b = 2z_0 = w_0^2 k_1 \tag{A.7}$$

$$\theta = \frac{\lambda}{\pi w_0 n} = \frac{2w_0}{b}. \tag{A.8}$$

The generated field at an arbitrary point outside the crystal can be determined by solving the coupled wave equation (Eq. 3.10). This can be explained as a summation over a number of crystal slices, with infinitesimal thickness dz. Every slice contributes to the second-harmonic wave generated as the incident wave interacts within it.
Assuming that the observation of the wave produced will take place in the far field at

a position (x', y', z'), a number of approximations can be accomplished to simplify the analysis. Furthermore some normalised spatial coordinates are introduced using the crystal length, L_c, the walk-off angle, ρ, and an arbitrary waist position, $\zeta = \frac{2(z-f)}{b}$.

$$\begin{aligned} u &= \frac{x' - \rho(L_c - f)}{w_0 \zeta} \\ v &= \frac{y'}{w_0 \zeta} \\ \beta &= \frac{\rho}{\theta} \end{aligned} \tag{A.9}$$

The second-harmonic intensity is proportional to the square of the field amplitude. The power is then simply an integration of the intensity over area

$$\begin{aligned} P_{2\omega} =& \frac{c\epsilon_0 n_{2\omega}}{8} \frac{k_{2\omega}^2}{n_{2\omega}^4} d_{\text{eff}}^2 \frac{E_0^4}{(\zeta')^2} e^{-\alpha_{2\omega} L_c} b^2 \pi^2 e^{-2\alpha f} \cdot \\ & \cdot \left(w_0 \zeta' \int_{-\infty}^{\infty} du\ e^{-4u^2} \left| H(\sigma', \kappa, \xi, \mu) \right|^2 \right) \left(w_0 \zeta' \int_{-\infty}^{\infty} dv\ e^{-4v^2} \right) \end{aligned} \tag{A.10}$$

using the following notation:

$$\begin{aligned} \kappa &= \frac{\alpha b}{2} \\ \sigma &= \frac{\Delta k b}{2} && \text{phase mismatch} \\ \sigma' &= \sigma + 4\beta u \\ \xi &= \frac{L_c}{b} && \text{focal strength} \\ \mu &= \frac{L_c - 2f}{L_c} && \text{focal position} \\ H(\sigma', \kappa, \xi, \mu) &= \frac{1}{2\pi} \int_{-\xi(1-\mu)}^{\xi(1+\mu)} \frac{e^{-\kappa\zeta} e^{i\sigma'\zeta}}{1 + i\zeta} \end{aligned} \tag{A.11}$$

The bulky expression Eq. A.10 can be formulated in a more convenient way by introducing the Boyd-Kleinman factor $h(\sigma, \beta, \kappa, \xi, \mu)$

$$F(\sigma, \beta, \kappa, \xi, \mu) = \frac{2}{\sqrt{\pi}} \int_{-\infty}^{\infty} du\ e^{-4u^2} \left| H(\sigma + 4\beta u, \kappa, \xi, \mu) \right|^2 \tag{A.12}$$

$$h(\sigma, \beta, \kappa, \xi, \mu) = \frac{\pi^2}{\xi} e^{\mu \alpha L_c} F(\sigma, \beta, \kappa, \xi, \mu). \tag{A.13}$$

Using, in addition, the relation between power and field amplitude

$$P_\omega = \frac{c\epsilon_0 n_\omega E_0^2 \pi w_0^2}{4}, \tag{A.14}$$

the final formula to calculate the power of a second-harmonic wave generated reads

$$P_{2\omega} = \frac{16\pi^2 d_{\text{eff}}^2}{c\epsilon_0 \lambda_\omega^3 n_\omega n_{2\omega}} P_\omega^2 L_c\ e^{-\alpha' L_c} h(\sigma, \beta, \kappa, \xi, \mu). \tag{A.15}$$

Eq. A.15 includes the incident power, P_ω, the crystal length, L_c, the effective susceptibility, d_{eff}, as well as the velocity of light, c, the refractive indices for pump and second-harmonic wave, n_ω and $n_{2\omega}$, the wavelength of the fundamental light, λ_ω, and an absorption factor, $\alpha' = \alpha_\omega + \alpha_{2\omega}/2$.

B. Resonant SHG

The generation of a frequency-doubled wave by a nonlinear crystal in a cavity is an interesting prospect, as lasers with low power output can be used as a pump. However, the fields involved are more complicated than in the case for a simple (linear-response) resonator. The conversion process in the crystal is dependent on but also influences the field circulating in the cavity. For the following explanation the nomenclature of Fig. 4.3, the distinction between amplitude coefficients (lower case letters) and power coefficients (upper case letters) as introduced in chapter 4, and the crystal transmission coefficient given by Eq. 4.8 are used. Absorption of the mirrors is neglected. The derivation of the finesse is provided in Sec. B.1. In Sec. B.2 a detailed consideration of the resonant enhancement is given.

B.1. Finesse

A derivation for the finesse of multiple beam interference can be found in [87]. Here, an outline is given on how the finesse formula can be derived and what the modifications are for a bow-tie configuration and a bow-tie resonator with SHG respectively.
Multiple beam interference results in a formula for the transmission of a bow-tie resonator using $R_\mathrm{T} = \prod_{i=1}^{4} R_i$ to simplify the notation.

$$\frac{P_\mathrm{trans}}{P_\mathrm{in}} = \frac{T_1 T_4 R_2 R_3}{(1-\sqrt{R_\mathrm{T}})^2 + 4\sqrt{R_\mathrm{T}}\sin^2(\frac{\Phi}{2})} \tag{B.1}$$

In Fig. 4.6 the ratio of transmitted power to incident power is plotted. The maxima in the figure have a period of $\Phi = 2\pi$ which corresponds to the resonance condition for the cavity. The value $\Delta\Phi$ is defined as the full width at half maximum for this curve.
Taking this as an input to an evaluation of Eq. B.1 leads to

$$\Delta\Phi = 4\arcsin\left(\frac{1-\sqrt{R_\mathrm{T}}}{2(R_\mathrm{T})^{1/4}}\right). \tag{B.2}$$

During a round trip a phase Φ between the circulating and the incident beam is achieved

$$\Phi = 2\pi\frac{L_\mathrm{opt}}{\lambda} = \frac{2\pi L_\mathrm{opt}\nu}{c}. \tag{B.3}$$

The phase is related to the optical path the light takes in the cavity, L_opt, the wavelength of the light, λ, or its frequency, $\nu = c/\lambda$. Hence, the resonance condition $\Phi = 2m\pi$ can be met by adjusting the optical path length. Relating the acquired phase to the resonance condition and solving it for the frequency, the formula $\nu_m = m\frac{L_\mathrm{opt}}{c}$ is achieved. The distance between consecutive resonance frequencies can then be described as the free spectral range $\Delta\nu_\mathrm{FSR}$

$$\Delta\nu_\mathrm{FSR} = \nu_{m+1} - \nu_m = \frac{L_\mathrm{opt}}{c}. \tag{B.4}$$

Taking into account these considerations the phase difference can be rewritten as a frequency difference

$$\begin{aligned}\Delta\nu_{\mathrm{FWHM}} &= \frac{c}{\pi L_{\mathrm{opt}}} 2\arcsin\left(\frac{1-\sqrt{R_{\mathrm{T}}}}{2(R_{\mathrm{T}})^{1/4}}\right) \\ &= \frac{\Delta\nu_{\mathrm{FSR}}}{\pi} 2\arcsin\left(\frac{1-\sqrt{R_{\mathrm{T}}}}{2(R_{\mathrm{T}})^{1/4}}\right).\end{aligned} \tag{B.5}$$

The finesse can then be given as the ratio of the free spectral range to the full width at half maximum of the frequency:

$$\mathcal{F}_{\text{bow tie}} = \frac{\Delta\nu_{\mathrm{FSR}}}{\Delta\nu_{\mathrm{FWHM}}} = \frac{\pi}{2\arcsin\left(\frac{1-\sqrt{R_{\mathrm{T}}}}{2(R_{\mathrm{T}})^{1/4}}\right)}. \tag{B.6}$$

If a setup including a bow-tie resonator containing a nonlinear crystal is involved, the finesse changes due to conversion losses, as the fundamental light is converted into the second-harmonic field. The field of interest is given by Eq. 4.11 assuming resonance and introducing the cavity reflectivity parameter $R_{\mathrm{m}} = R_2R_3R_4T_{\mathrm{x}}(1-\mathcal{K}P_{\mathrm{circ}})$. With an analysis analogous to the one described previously, the finesse can be shown to be

$$\mathcal{F}_{\mathrm{SHG}} = \frac{\pi}{2\arcsin\left(\frac{1-\sqrt{R_1R_{\mathrm{m}}}}{2(R_1R_{\mathrm{m}})^{1/4}}\right)} \approx \frac{\pi(R_{\mathrm{T}}(1-\mathcal{L}_{\mathrm{T}}))^{1/4}}{\left(1-\sqrt{R_{\mathrm{T}}(1-\mathcal{L}_{\mathrm{T}})}\right)}. \tag{B.7}$$

In the formula above, the last term uses the relation $\arcsin\alpha \approx \alpha$ assuming sharply defined resonance. $R_{\mathrm{T}} = \prod_{i=1}^{4} R_i$ represents the total reflectivity of all mirrors and the parameter $\mathcal{L}_{\mathrm{T}}$ indicates all losses that the transition through the resonator introduces $(1-\mathcal{L}_{\mathrm{T}}) = T_{\mathrm{x}}(1-\mathcal{K}P_{\mathrm{circ}})$. Further simplicity is gained by taking the total reflectivity as close to unity $R_{\mathrm{T}} \approx 1$.

$$\mathcal{F}_{\mathrm{SHG}} \approx \frac{\pi}{\left(1-\sqrt{R_{\mathrm{T}}(1-\mathcal{L}_{\mathrm{T}})}\right)} \tag{B.8}$$

This offers a possibility to determine the losses in the cavity, given the finesse.

B.2. SHG with a resonator

The overall conversion efficiency is introduced as

$$\mathcal{Q} = \frac{P_{2\omega}}{P_{\mathrm{in}}} = \frac{\mathcal{K}P_{\mathrm{circ}}^2}{P_{\mathrm{in}}} \tag{B.9}$$

which can be rewritten using Eq. 3.19 and substituting Eq. 4.11 (resonant case) into it, and taking the square root:

$$\sqrt{\mathcal{Q}} = \sqrt{\mathcal{K}P_{\mathrm{in}}}\frac{T_1}{\left(1-\sqrt{R_1R_{\mathrm{m}}}\right)^2}. \tag{B.10}$$

This can be rewritten to point out the dependence of the power upon R_m

$$\begin{aligned}\sqrt{\mathcal{Q}} &= \sqrt{\mathcal{K}P_\mathrm{in}}\frac{T_1}{\left(1-\sqrt{1-T_1}\sqrt{R_2R_3R_4T_\mathrm{x}(1-\mathcal{K}P_\mathrm{circ})}\right)^2}\\ &= \sqrt{\mathcal{K}P_\mathrm{in}}\frac{T_1}{\left(1-\sqrt{1-T_1}\sqrt{(1-\mathcal{L})(1-\sqrt{\mathcal{K}\mathcal{Q}P_\mathrm{in}})}\right)^2}\end{aligned} \tag{B.11}$$

In the latter expression of Eq. B.11, the total losses in the resonator not attributed to conversion losses are summarised in the factor $\mathcal{L}$, where $(1-\mathcal{L}) = R_2R_3R_4T_\mathrm{x}$. The $\mathcal{Q}$-factor is only dependent on the incident power. In the case of impedance matching the incident power is increased by $(T_1)^{-1}$. It is therefore related to the circulating power by $P_\mathrm{circ} = \frac{P_\mathrm{in}}{T_1^\mathrm{opt}}$. The optimum transmission coefficient for the input coupling mirror T_1^opt to get impedance matching is equal to the resonator losses and the losses due to conversion

$$T_1^\mathrm{opt} = \mathcal{L} + \mathcal{K}\frac{P_\mathrm{in}}{T_1^\mathrm{opt}}. \tag{B.12}$$

The enhancement factor can then be rewritten yielding

$$\sqrt{\mathcal{Q}} = \sqrt{\mathcal{K}P_\mathrm{in}}\frac{T_1}{\left(1-\sqrt{1-T_1}\sqrt{(1-\mathcal{L})(1-\mathcal{K}\frac{P_\mathrm{in}}{T_1})}\right)^2}. \tag{B.13}$$

To give a closed expression for T_1^opt a quadratic equation has to be solved, leading to the solution

$$T_1^\mathrm{opt} = \frac{\mathcal{L}}{2} + \sqrt{\left(\frac{\mathcal{L}^2}{4} + \mathcal{K}P_\mathrm{in}\right)}. \tag{B.14}$$

If this condition (Eq. B.12) is met, the overall conversion efficiency reduces to

$$\sqrt{\mathcal{Q}} = \frac{\sqrt{\mathcal{K}P_\mathrm{in}}}{T_1^\mathrm{opt}}. \tag{B.15}$$

Hence, using Eq. B.9 the generated second-harmonic power is related to the incident power as

$$\begin{aligned}P_{2\omega} &= \frac{\mathcal{K}P_1^2}{(\frac{\mathcal{L}}{2}+\sqrt{\frac{\mathcal{L}^2}{4}+\mathcal{K}P_\mathrm{in}})^2}\\ &= \frac{P_\mathrm{in}}{\frac{\mathcal{L}^2}{4\mathcal{K}P_\mathrm{in}} + 2\sqrt{\frac{\mathcal{L}^2}{4\mathcal{K}P_\mathrm{in}}}\sqrt{\frac{\mathcal{L}^2}{4\mathcal{K}P_\mathrm{in}}+1} + \left(1+\frac{\mathcal{L}^2}{4\mathcal{K}P_\mathrm{in}}\right)}\\ &= \frac{P_\mathrm{in}}{\left(X_\mathrm{FOM}+\sqrt{1+X_\mathrm{FOM}^2}\right)^2}.\end{aligned} \tag{B.16}$$

The factor $X_\mathrm{FOM}^2 = \frac{\mathcal{L}^2}{4\mathcal{K}P_\mathrm{in}}$ and FOM is an abbreviation for figure of merit.

C. Laser Setup

In this appendix, useful reference information is summarised to facilitate the operation of the photoionisation system built as a part of this work. Sec. C.1 gives the calibration curve for the temperature stabilisation of the frequency-doubling crystal. Sec. C.2 gives a brief introduction to turning on the doubling system, and also basic trouble-shooting. Concluding, Sec. C.3 summarises the basic steps in designing a second-harmonic generation (SHG) system.

C.1. Calibration of TOPTICA's DTC 110 SVL

When rebuilding the doubling-crystal temperature stabilisation, the home-built Wheatstone bridge and PID controller was replaced with a Peltier element and a temperature stabilisation circuit developed by Toptica. This provided a quick solution guaranteeing convenience and ease use. Toptica, however, readily admits that the temperature controller is not well calibrated at elevated temperatures. To assure meaningful temperature measurements, a calibration was carried out before heating up the crystal for the first time. This was done by connecting the Peltier element and the negative temperature coefficient (NTC) temperature sensor to the Toptica box (DTC 110 SVL) and measuring the temperature in the crystal holder, where the crystal would be situated in the real setup, with a thermistor (PT1000). Beginning from 35 °C a deviation from the temperature monitored with the DTC 110 SVL could be observed, as summarised in Fig. C.1.

C.2. Using the 422 nm frequency doubler

Powering up the system to get 422 nm light can be accomplished following the steps listed below.

1. Assure that the laser diode at 844 nm is temperature stabilised (DTC 110 Monitor). If this is not the case, put the 'on/off' dip switch on the DTC 110 in position 'on' and set the temperature to the desired value (at the time of writing, T_{diode} = 18.3 °C). When the temperature is stable, set the 'on/off' dip switch for the DCC 110 to 'on', and the 'on/off' dip switch for the ScanControl module and the PID 110 module to position 'on'. Then push the green button on the DCC 110 monitor unit - the diode is supplied with power.

2. Check that the frequency generator supplies a saw-tooth signal for the PID 110 (the settings should be chosen such that scanning of the doubling-cavity's piezo assures monitoring of at least two free spectral ranges; good values are an amplitude of 10 V, a frequency of 60 Hz and an offset voltage of -3 V). Set the 'reg.' (regulation) switch to position 'off' and the 'mod.' (modulation) switch to position 'in' to scan the cavity. Switch on the photodiodes in the setup and the oscilloscope and check

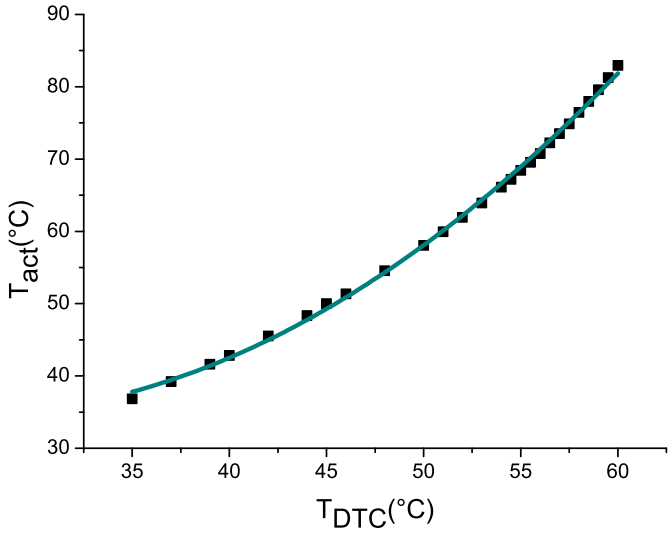

Figure C.1.: The measured temperatures in the crystal position (T_{act}) as a function of the temperature given by the DTC 110 SVL (T_{DTC}). The fit gives the nonlinear relation $T_{\mathrm{act}} = 62\,(^{\circ}\mathrm{C}) - 2.1 T_{\mathrm{DTC}}\,(^{\circ}\mathrm{C}) + 0.041\,(^{\circ}\mathrm{C})^{-1} T_{\mathrm{DTC}}^2\,(^{\circ}\mathrm{C})^2$ between the actual temperature at the crystal position and the monitored temperature.

the monitored signals. CH1 represents the reference signal while CH2 and CH3 are the signals used for the locking system. CH4 shows the monitor output of the PID 110.

3. After having been operated for 10 min to 15 min the laser is stable enough to adjust the wavelength using the wavemeter. A supply current of approximately 110 mA produces sufficient second-harmonic power to run an experiment. It is good to double check the mode stability with the photodiode signals displayed at the oscilloscope. If the signal is really broad and noisy, the laser is most probably about to undergo a mode hop.

4. Having set the laser to the desired wavelength, it is recommendable to increase the input coupling to the cavity if possible. It is not necessary to use the resonator mirrors themselves for this purpose - the two preceding input coupling mirrors are sufficient.

5. Changes in the wavelength often result in a slight variation of the locking signal. This is accounted for when overlapping the signals of CH2 and CH3 with the help of the $\lambda/2$ and $\lambda/4$ waveplates in the locking system. The difference of the signals can be displayed at the oscilloscope as well, giving a better feeling for the behaviour.

6. The lock can be easily established using the PID 110. In the present system, change the setting of the 'mod.' switch to position 'off' and the position of the 'reg.' switch to 'lock'. If the lock is not working properly at first, an increase of the gain factor often suffices.

7. Provided the crystal is at the correct temperature (at the time of writing, the value from the Toptica temperature control is 57.4 °C which corresponds to a crystal temperature of 76.6 °C) 422 nm light should now be produced.

Trouble-shooting

- **Wavelength unstable**
  If the laser wavelength appears to be quite unstable, it is possibly due to an approaching mode hop. Change the supply current and the piezo voltage with the DCC 110 and the ScanControl, respectively. After a power outage it may happen that an additional change has to be made using the micrometre screw to adjust the grating, or by adjusting the temperature, to find a stable operation point again. It is recommended to keep the laser running for about half an hour at least, before any changes are carried out. Otherwise, it might not yet be in a regime where it is stably operating. These steps may alter the beam pointing and so the input coupling efficiency to the cavity should always be subsequently optimised, especially after a power outage. In the latter case, it might also be useful to not only use the input coupling mirrors as usual, but to take into account the other cavity mirrors as well. A check of the beam path after the cavity and the fibre coupling efficiency conclude the procedure.

- **Input coupling decreased**
  With the setup at hand a decrease in input coupling occurs rarely; minor adjustments are required every few weeks. Possible causes, however, include a change in wavelength or an unwanted change in the setup. It is easiest to check all possible error sources, starting by the wavemeter, moving on the possible change in components and checking the $\lambda/2$ waveplate before the resonator. At the time of writing this is set to $324\,^\circ$ (which is also marked on it) as this is the angle where the input coupling is good and the lock works best. If all other possibilities have been ruled out and all attempts to increase the input coupling efficiency only using the input coupling mirrors have been tried, the cavity mirrors have to be readjusted. As described for the case of unstable wavelength, the beam path and coupling efficiencies after the resonator have to be checked properly.

- **Bad locking behaviour**
  A bad error signal can be usually traced down to either a decreased input coupling (see instructions above) or because of a mismatch of the signal coming from PD2 and PD3. In the latter case, use the $\lambda/2$ waveplate in the locking system to maximise one signal, increase it further with the $\lambda/4$ waveplate (i.e. so that all light goes to only one PD).Rotate the waveplates to reduce the signal of the maximised PD to half its maximum value (i.e. reshare the light equally between the two PDs). It is good to check the progress of this process using the 'math' (difference) signal on the oscilloscope.
  If the error signal looks good and the lock still will not work by simply increasing the gain, the PID settings may have to be renewed: Set both the 'reg.' (regulation) switch and the 'mod.' (modulation) switch in position 'off' and try to find an offset voltage for the piezo which is at or around resonance (scan it by turning the 'output offset' potentiometer[1] and as the signal of PD1, PD2 or PD3 on the oscilloscope screen goes down, the resonator matches the resonance condition). A good rule of thumb to set the PID settings is P approximately 3 turns with the

[1] Clockwise decreases the offset voltage, anticlockwise increases it!

potentiometer screwdriver, I roughly 2.5 turns and D about 3.5 turns in clockwise direction, measured from the position in which they are turned completely off. The gain should be set to 2. Set the 'reg' switch to 'lock' and try to get a locking signal that is as smooth as possible by varying the settings of P, I and D. If the Hänsch - Couillaud lock in our setup works well, it can follow the laser scanning with a repetition rate of once every five seconds over a range of 2 GHz without problems. If the laser supply current is increased or decreased, the PID settings for the lock may no longer be optimally adjusted for the situations. Hence, it can happen that a simple increase in the gain factor will not suffice. In this case as well, new PID values should be implemented as described.

- **No blue light**
  There are several reasons why the operation of the frequency doubling system does not provide light at 422 nm wavelength. Check to see that
  - the wavelength is correct
  - the input coupling is at a good value (typically around 50 %),
  - the crystal temperature stabilisation is working and is at the correct temperature.

In general, the stability observed so far was sufficient. Even after not having been operated for two weeks, the settings have to undergo only minor changes before stably providing 422 nm light again.

C.3. Considerations for building a doubler

For setting up a doubling system, the following steps outline the things to do:

1. Choose an appropriate crystal.
   Factors influencing the decision are:
   - Which wavelength should be generated; Comparison of the effective susceptibilities for different materials;
   - What crystal length is suitable; Considerations concerning costs, focusing and wavelength bandwidth;
   - How easy is the handling of the crystal; Are there certain conditions that have to be met (is the crystal hygroscopic, should any extreems of temperature be avoided etc.);
   - What type of phasematching should be used (birefringent or quasi-phasematching or even other possibilities);
   - In which range does the temperature for maximum second-harmonic intensity lie; Consider the heating element that can be used;
   - How strongly does angle tuning influence the second-harmonic power generated and how big is the introduced walk-off.
   - Should the crystal be Brewster cut or be AR coated.
2. The cavity should be simulated using the data of the mirrors you want to use and the space that is designated to it (see chapter 4).

3. Impedance matching considerations have to be made (see chapter 4).

4. Set up the system according to your simulations. Use lenses to achieve matching of the laser mode onto the cavity mode (see chapter 5). Couple light into the cavity with an efficiency as high as possible.

5. When good input coupling is achieved, vary the crystal temperature about the expected set point and try to find the temperature where maximum second-harmonic power is generated.

6. Having tuned the temperature, angular tuning can be carried out. After each change in crystal position, the input coupling efficiency has to be optimised again. Sometimes, it is necessary to tune the temperature again after tuning the angle.

Bibliography

[1] R. P. Feynman, *Simulating Physics with Computers*, Int. J. Theor. Phys. **21**, 467 (1982).

[2] D. Deutsch, *Quantum theory, the Church-Turing principle and the universal quantum computer*, in *Proc. R. Soc. London, Ser. A*, 1985.

[3] D. Deutsch and R. Jozsa, *Rapid solution of problems by quantum computation*, Proc. R. Soc. Lond. A **439**, 553 (1992).

[4] P. W. Shor, *Algorithms for Quantum Computation: Discrete Logarithms and Factoring*, in *IEEE*, 1994.

[5] J. I. Cirac and P. Zoller, *Quantum Computations with Cold Trapped Ions*, Phys. Rev. Lett. **74**, 4091 (1995).

[6] L. K. Grover, *Quantum Mechanics Helps in Searching for a Needle in a Haystack*, Phys. Rev. Lett. **79**, 325 (1997).

[7] A. R. Calderbank and P. W. Shor, *Good quantum error-correcting codes exist*, Phys. Rev. A **54**, 1098 (1996).

[8] D. P. DiVincenzo, *The Physical Implementation of Quantum Computation*, Fortschr. Phys. **48**, 771 (2000).

[9] R. Blatt, *The quantum revolution - towards a new generation of supercomputers*, in *Proc. ICOLS*, 2007.

[10] D. Leibfried, C. Roos, P. Barton, H. Rohde, S. Gulde, A. B. Mundt, F. Schmidt-Kaler, J. Eschner, and R. Blatt, *Towards quantum computation with trapped calcium ions*, in *Proc. QIPC-Y2K*, 2000.

[11] H. Häffner, W. Hänsel, C. F. Roos, P. O. Schmidt, M. Riebe, M. Chwalla, D. Chekal Kar, J. Benhelm, U. D. Rapol, T. K. Orber, C. Becher, O. Gühne, W. Duer, and R. Blatt, *Quantum computation with trapped ions*, in *Controllable Quantum States*, 2008.

[12] J. C. Bergquist, R. G. Hulet, W. M. Itano, and D. J. Wineland, *Observation of Quantum Jumps in a Single Atom*, Phys. Rev. Lett. **57**, 1699 (1986).

[13] W. Nagourney, J. Sandberg, and H. Dehmelt, *Shelved Optical Electron Amplifier: Observation of Quantum Jumps*, Phys. Rev. Lett. **56**, 2797 (1986).

[14] T. Sauter, W. Neuhauser, R. Blatt, and P. E. Toscheck, *Observation of Quantum Jumps*, Phys. Rev. Lett. **57**, 1696 (1986).

[15] W. Paul, *Electromagnetic traps for charged and neutral particles*, Rev. Mod. Phys. **62**, 531 (1990).

[16] D. Leibfried, R. Blatt, C. Monroe, and W. D., *Quantum dynamics of single trapped ions*, Rev. Mod. Phys. **75**, 261 (2003).

[17] M. Riebe, H. Häffner, C. F. Roos, W. Hänsel, J. Benhelm, G. P. T. Lancaster, T. W. Körber, C. Becher, F. Schmidt-Kaler, D. F. V. James, and R. Blatt, *Deterministic quantum teleportation with atoms*, Nature **429**, 734 (2004).

[18] M. D. Barrett, J. Chiaverini, T. Schätz, J. Britton, W. M. Itano, J. D. Jost, E. Knill, C. Langer, D. Leibfried, R. Ozeri, and D. J. Wineland, *Deterministic quantum teleportation of atomic qubits*, Nature **429**, 737 (2004).

[19] S. Olmschenk, D. N. Matsukevich, P. Maunz, D. Hayes, L.-M. Duan, and C. Monroe, *Quantum Teleportation Between Distant Matter Qubits*, Science **323**, 486 (2009).

[20] D. L. Moehring, P. Maunz, S. Olmschenk, K. C. Younge, D. N. Matsukevich, L.-M. Duan, and C. Monroe, *Entanglement of single-atom quantum bits at a distance*, Nature **449**, 68 (2007).

[21] C. F. Roos, M. Riebe, H. Häffner, W. Hänsel, J. Benhelm, G. P. T. Lancaster, C. Becher, F. Schmidt-Kaler, and R. Blatt, *Control and Measurement of Three-Qubit Entangled States*, Science **304**, 1478 (2004).

[22] B. B. Blinov, D. L. Moehring, L.-M. Duan, and C. Monroe, *Observation of entanglement between a single trapped atom and a single photon*, Nature **428**, 153 (2004).

[23] C. Monroe, D. M. Meekhof, B. E. King, W. M. Itano, and D. J. Wineland, *Demonstration of a Fundamental Quantum Logic Gate*, Phys. Rev. Lett. **75**, 4714 (1995).

[24] F. Schmidt-Kaler, H. Häffner, M. Riebe, S. Gulde, G. P. T. Lancaster, T. Deuschle, C. Becher, C. F. Roos, J. Eschner, and R. Blatt, *Realization of the Cirac-Zoller controlled-NOT quantum gate*, Nature **422**, 408 (2003).

[25] B. DeMarco, A. Ben-Kish, D. Leibfried, V. Meyer, M. Rowe, B. M. Jelenkovic, W. M. Itano, J. Britton, C. Langer, T. Rosenband, and D. J. Wineland, *Experimental Demonstration of a Controlled-NOT Wave-packet Gate*, Phys. Rev. Lett. **89**, 267901 (2002).

[26] D. Leibfried, B. DeMarco, V. Meyer, D. Lucas, M. Barrett, J. Britton, W. M. Itano, B. Jelenkovic, C. Langer, R. Rosenband, and D. J. Wineland, *Experimental demonstration of a robust, high-fidelity geometric two ion-qubit phase gate*, Nature **422**, 412 (2003).

[27] T. Monz, K. Kim, W. Hänsel, M. Riebe, A. S. Villar, P. Schindler, M. Chwalla, M. Hennrich, and R. Blatt, *Realization of the Quantum Toffoli Gate with Trapped Ions*, Phys. Rev. Lett. **102**, 040501 (2009).

[28] S. Gulde, M. Riebe, G. P. T. Lancaster, C. Becher, J. Eschner, H. Häffner, F. Schmidt-Kaler, I. L. Chuang, and R. Blatt, *Implementation of the Deutsch-Jozsa algorithm on an ion-trap quantum computer*, Nature **421**, 48 (2003).

[29] J. Chiaverini, J. Britton, D. Leibfried, E. Knill, M. D. Barrett, R. B. Blakestad, W. M. Itano, J. Jost, C. Langer, R. Ozeri, S. T., and D. J. Wineland, *Implementation of the Semiclassical Quantum Fourier Transform in a Scalable System*, Science **308**, 997 (2005).

[30] D. Leibfried, E. Knill, S. Seidelin, J. Britton, R. B. Blakestad, J. Chiaverini, D. B. Hume, W. M. Itano, J. D. Jost, C. Langer, R. Ozeri, R. Reichle, and D. J. Wineland, *Creation of a six-atom 'Schroedinger cat' state*, Nature **438**, 639 (2005).

[31] J. Chiaverini, D. Leibfried, T. Schätz, M. D. Barrett, R. B. Blakestad, J. Britton, W. M. Itano, J. D. Jost, E. Knill, C. Langer, R. Ozeri, and D. J. Wineland, *Realizsation of quantum error correction*, Nature **432**, 602 (2004).

[32] R. Gerritsma, G. Kirchmair, F. Zähringer, E. Solano, R. Blatt, and C. F. Roos, *Quantum simulation of the Dirac equation*, Nature **463**, 1 (2010).

[33] D. Hanneke, J. P. Home, J. D. Jost, J. M. Amini, D. Leibfried, and D. J. Wineland, *Realization of a programmable two-qubit quantum processor*, Nature Phys. **6**, 1 (2009).

[34] R. J. Hughes, D. F. V. James, E. H. Knill, R. Laflamme, and A. G. Petschek, *Decoherence Bounds on Quantum Computation with Trapped Ions*, Phys. Rev. Lett. **77**, 3240 (1996).

[35] A. M. Steane, *How to build a 300 bit, 1 giga-operation quantum computer*, Quantum Inf. Comput. **7**, 171 (2007).

[36] D. Kielpinski, C. Monroe, and J. Wineland, *Architecture for a large-scale ion-trap quantum computer*, Nature **417**, 709 (2002).

[37] J. Chiaverini, R. B. Blakestad, J. Britton, J. D. Jost, C. Langer, D. Leibfried, R. Ozeri, and D. J. Wineland, *Surface-electrode architecture for ion-trap quantum information processing*, Quantum Inf. Comput. **5**, 419 (2005).

[38] S. Seidelin, J. Chiaverini, R. Reichle, J. J. Bollinger, D. Leibried, J. Britton, J. H. Wesenber, R. B. Blakestad, R. J. Epstein, D. B. Hume, W. M. Itano, J. D. Jost, C. Langer, R. Ozeri, N. Shiga, and D. J. Wineland, *Microfabricated Surface-Electrode Ion Trap for Scalable Quantum Information Processing*, Phys. Rev. Lett. **96**, 253003 (2006).

[39] C. E. Pearson, D. R. Leibrandt, W. S. Bakr, W. J. Mallard, K. Brown, and I. L. Chuang, *Experimental investigation of planar ion traps*, Phys. Rev. A **73**, 032307 (2006).

[40] F. Splatt, M. Harlander, M. Brownnutt, F. Zähringer, R. Blatt, and W. Hänsel, *Deterministic recording of $^{40}Ca^{+}$ ions in a linear segmented Paul trap*, New J. Phys. **11**, 1 (2009).

[41] L. Deslauriers, S. Olmschenk, D. Stick, W. K. Hensinger, J. Sterk, and C. Monroe, *Scaling and Suppression of Anomalous heating in Ion Traps*, Phys. Rev. Lett. **97**, 103007 (2006).

[42] Q. A. Turchette, D. Kielpinski, B. E. King, D. Leibfried, D. M. Meekhof, C. J. Myatt, M. A. Rowe, C. A. Sackett, C. S. Wood, W. M. Itano, C. Monroe, and D. J. Wineland, *Heating of trapped ions from the quantum ground state*, Phys. Rev. A **61**, 063418 (2000).

[43] D. Stick, W. K. Hensinger, S. Olmschenk, M. J. Madsen, K. Schwab, and C. Monroe, *Ion trap in a semiconductor chip*, Nature Phys. **2**, 36 (2006).

[44] P. B. Antohi, D. Schuster, G. M. Akselrod, J. Labaziewicz, Y. Ge, W. S. Lin, Z. Bakr, and I. L. Chuang, *Cryogenic ion trapping systems with surface-electrode traps*, Rev. Sci. Instrum. **80**, 013103 (2009).

[45] J. Labaziewicz, Y. Ge, P. Antohi, D. Leibrandt, K. R. Brown, and I. L. Chuang, *Suppression of Heating Rates in Cyrogenic Sufrace-Electrode Ion Traps*, Phys. Rev. Lett. **100**, 013001 (2008).

[46] R. G. DeVoe and C. Kurtsiefer, *Experimental st6udy of anomalous heating and trap instabilities in a microscopic ^{137}Ba ion trap*, Phys. Rev. A **65**, 063407 (2002).

[47] M. Brownnutt, V. Letchumanan, G. Wilpers, T. R. C., P. Gill, and A. G. Sinclair, *Controlled photoionization loading of $^{88}Sr^+$ for precision ion-trap experiments*, Appl. Phys. B **87**, 411 (2007).

[48] S. Gulde, D. Rotter, P. Barton, F. Schmidt-Kaler, R. Blatt, and W. Hogervorst, *Simple and efficient photo-ionization loading of ions for precision ion-trapping experiments*, Appl. Phys. B **73**, 861 (2001).

[49] D. Rotter, *Photoionisation von Kalzium*, Master's thesis, Leopold-Franzens-Universität Innsbruck, 2003.

[50] D. Lucas, A. Ramos, J. Home, M. McDonnell, S. Nakayama, J.-P. Stacey, S. Webster, D. Stacey, and A. Steane, *Isotope-selective photoionization for calcium ion trapping*, Phys. Rev. A **69**, 012711 (2004).

[51] *Der Brockhaus Naturwisschenschaft und Technik 1 A - GD*, F.A. Brockhaus AG and Spektrum Akademischer Verlag, 2003.

[52] R. Blatt, H. Häffner, C. F. Roos, C. Becher, and F. Schmidt-Kaler, *Ion Trap Quantum Computing with Ca^+ Ions*, Quantum Inf. Process. **3**, 61 (2004).

[53] D. Meschede, *Gerthsen Physik*, Springer Verlag, 2006.

[54] F. Schmidt-Kaler, S. Gulde, M. Riebe, T. Deuschle, A. Kreuter, G. Lancaster, C. Becher, J. Eschner, H. Häffner, and R. Blatt, *The coherence of qubits based on single Ca^+ ions*, J. Phys. B: At. Mol. Opt. Phys. **36**, 623 (2003).

[55] M. O. Scully and M. S. Zubairy, *Quantum Optics*, Cambridge University Press, 1997.

[56] J. N. Dodd, *Atoms and Light Interactions*, Plenum Press, 1991.

[57] C. J. Foot, *Atomic Physics*, Oxford University Press, 2008.

[58] B. W. Shore, *The theory of coherent atomic excitation*, volume 2, John Wiley & Sons, 1990.

[59] B. W. Shore, *The theory of coherent atomic excitation*, volume 1, John Wiley & Sons, 1990.

[60] C. Cohen-Tannoudji, B. Diu, and F. Laloë, *Quantenmechanik 2*, Walter de Gruyter, 1999.

[61] A. Einstein, *On the Quantum Theory of Light*, Physik. Z. **18**, 121 (1917).

[62] R. D. Cowan, *The theory of atomic structure and spectra*, University of California Press, 1981.

[63] R. Loudon, *The Quantum Theory of Light*, Oxford Science Publications, 2007.

[64] T. Maiman, *Stimulated optical radiation in ruby*, Nature **187**, 493 (1960).

[65] D. Meschede, *Optics, Light and Lasers*, Wiley-VCH, 2007.

[66] B. E. A. Saleh and M. C. Teich, *Fundamentals of Photonics*, John Wiley & Sons, 2007.

[67] A. E. Siegman, *Lasers*, University Science Books, 1986.

[68] Y. R. Shen, *The Principles of Nonlinear Optics*, John Wiley & Sons, 1984.

[69] A. Yariv and P. Yeh, *Optical Waves in Crystals*, John Wiley & Sons, 1984.

[70] M. M. Fejer, G. A. Magel, D. H. Jundt, and R. L. Byet, *Quasi-Phase-Matched Second Harmonic Generation: Tuning and Tolerances*, IEEE J. Quantum Electron. **28**, 2631 (1992).

[71] W. P. Risk, T. R. Gosnell, and A. V. Nurmikko, *Compact Blue-Green Lasers*, Cambridge University Press, 2003.

[72] A. Yariv, *Optical Electronics*, Holt, Rinehart and Winston, 1991.

[73] D. S. Hum and M. M. Fejer, *Quasi-phasematching*, C. R. Physique **8**, 180 (2007).

[74] G. D. Boyd and D. A. Kleinman, *Parametric interaction of focused gaussian light beams*, J. Appl. Phys. **39**, 3597 (1968).

[75] E. Hecht, *Optics*, Addison Wesley, 2002.

[76] H. Abitan and T. Skettrup, *Laser resonators with several mirrors and lenses with the bow-tie laser resonator with compensation for astigmatism and thermal lens effects as an example*, J. Opt. A: Pure Appl. Op. **7**, 7 (2005).

[77] H. Kogelnik and T. Li, *Laser Beams and Resonators*, Appl. Opt. **5**, 1550 (1966).

[78] D. Nigg, *Aufbau eines Frequenz-vervierfachten Diodenlasers für die Photoionisation von Magnesium*, Master's thesis, Universität Innsbruck, 2009.

[79] O. S. Brozek, *Effiziente Frequenzverdopplung mit Diodenlasern*, Master's thesis, Universität Hannover, 1995.

[80] W. J. Kozlovsky, C. D. Nabors, and R. L. Byer, *Efficient Second Harmonic Generation of a Diode-Laser-Pumped CW Nd:YAG Laser Using Monolithic $MgO : LiNbO_3$ External Resonant Cavities*, IEEE J. Quantum Electron. **24**, 913 (1988).

[81] T. W. Hänsch and B. Couillaud, *Laser frequency stabilization by polarization spectroscopy of a reflecting reference cavity*, Opt. Commun. **35**, 441 (1980).

[82] Thorlabs, *TCLDM9 5.6mm/9mm Laser Diode Mount; Operating Manual*, 2003.

[83] Toptica Photonics AG, Lochhamer Schlag 19 D-82166 Graefelfing/Munich, *Sys DC 110 Diode Laser Supply Electronics*, m-007 version 03 edition, 2008.

[84] M. Brownnutt, *$^{88}Sr^{+}$ ion trapping techniques and technologies for quantum information*, PhD thesis, Imperial College London, 2007.

[85] J. P. Schiffer, *Phase Transitions in Anisotropically Confined Ionic Crystals*, Phys. Rev. Lett. **70**, 818 (1993).

[86] J. M. Amini, J. Britton, D. Leibfried, and D. J. Wineland, *Atom Chips*, Wiley-VCH, 2008.

[87] W. Demtröder, *Laser Spectroscopy*, Springer Verlag, 1996.

Danksagung

An dieser Stelle möchte ich jenen Menschen danken, ohne deren Hilfe und Unterstützung die Durchführung dieser Arbeit undenkbar gewesen wäre.
Allen voran danke ich Herrn Prof. Rainer Blatt, der mich als Diplomandin in seine Gruppe aufnahm und mir damit die Möglichkeit bot, im Rahmen eines interessanten Projektes den Aufbau eines neuen Experiments mitzuverfolgen und mitzugestalten.
Mit Rat und Tat zur Seite stand mir vor allem Mike Brownnutt, sowohl im Labor als auch während des Schreibens meiner Arbeit. Für alle Ratschläge und Diskussionen, die für mich einen unschätzbaren Wert haben und mir so manches Mal dabei halfen weiterzumachen, bedanke ich mich herzlich. Auch Michael Niedermayr und Muir Kumph haben als Mitstreiter am Cryotrap-Experiment wesentlich zum Gelingen meines Vorhabens beigetragen, was gekrönt wurde durch eine erste, gemeinsam durchgeführte Messung.
Nicht zu vergessen ist des Weiteren Mike Chwalla, der mir nicht nur beim Lösen einiger Latex Probleme geholfen hat, sondern großzügigerweiße auch noch die Layout-Datei für die Bibliographie und die Online Version dieser Arbeit zur Verfügung gestellt hat.
Angeführt sei außerdem noch Max Harlander von dem ich dankenswerterweise in die Weißwurst-Kochgruppe (WWG) aufgenommen wurde. Wer glaubt, es gibt fünf Tage die Woche Weißwurst, den belehren wir gern eines Besseren, zum Beispiel mit vegetarischen Spaghetti (falls noch etwas übrig ist, nachdem ich zugeschlagen habe).
Von Anfang an begeistert haben mich die gesamte 'Arbeitsgruppe Blatt' sowie die Sekretärinnen des Instituts und die Mitarbeiter der Werkstätten mit der Bereitwilligkeit jedes Einzelnen, mir auf meine Fragen eine Antwort zu geben und mir bei der Lösung der auftretenden Probleme zu helfen. Ich bin dankbar in einem Klima gearbeitet zu haben, das vom Miteinander und dem Willen sich gegenseitig zu unterstützen geprägt gewesen ist.
Außerstande alle Personen, denen ich zu Dank verpflichtet bin, hier namentlich zu erwähnen möchte ich ein kollektives 'Dankeschön' an alle richten, die meine Diplomarbeit zu dem gemacht haben, was letztlich zählt: Eine ungemein lehrreiche Erfahrung, nicht nur im physikalischen, sondern auch im menschlichen Sinn.

Ein Mensch, der mich durch meine gesamte Studienzeit begleitet hat, sollte zwischen diesen Dankesworten nicht fehlen. Ein großes Dankeschön gilt meinem Praktikumspartner und guten Kollegen Simon, mit dem nicht nur die Messungen für diverse Praktika und die anschließende Auswertung gut zu bewähltigen waren sondern auch so manche Party zu einem unvergesslichen Ereignis wurde. Abseits der Universität möchte ich noch meinen Freunden danken - besonders Anke, die ich mich unglaublich glücklich schätze zu kennen.
Natürlich gilt mein besonderer Dank meiner Familie, allen voran meinen Eltern Monika und Hermann. In allen Lagen waren und sind sie mir Stütze, ihr scheinbar grenzenloses Vertrauen und ihre Stolz sind mir Ansporn und ich wäre heute nicht die, die ich bin, ohne ihre Fürsorge.
Danke!